ULB UNIVERSITÉ LIBRE DE BRUXELLES

iihe BRUXELLES BRUSSEL

Faculté des Sciences
Département de Physique

Study of a Triple GEM detector for the upgrade in the forward region of the CMS Muon System at the LHC

Federico Lucchetti

Promoteur : Dr. Gilles De Lentdecker

Année académique 2013-2014

Mémoire présenté en vue de l'obtention du diplôme de Master en Sciences Physiques

Résumé

Dans les années à venir, le LHC passera dans une phase de haute luminosité. Ainsi CMS sera exposé à un flux élevé de particules dans la région avant du spectromètre à muons. Ce travaille est destiné à l'étude des détecteurs Triple GEM pour la mise à niveau de la partie avant $1.6 < |\eta| < 2.4$ du spectromètre à muons de CMS, afin de pouvoir augmenter la redondance dans cette région. Le grand atout de cette nouvelle technologie est le maintien d'une efficacité de détection élevé sous des taux de radiations intenses.

Ce travail est consacré à la simulation de la réponse d'un détecteur Triple GEM , couvrant la modélisation de plusieurs processus se déroulant à l'intérieur du détecteur entre autre l'ionisation primaire, le processus d'avalanche électronique et la formation du signal sur les électrodes de lectures. Une partie de ces résultats seront confrontées avec des données réelles, prises sur un prototype Triple GEM.

Abstract

In the coming years, the LHC will enter its phase of high luminosity. As a result the CMS detector complex will be subjected to a high flux rate of particles in the forward region of the muon spectrometer. The purpose of this work is to study Triple GEM detectors for the upgrade in the $1.6 < |\eta| < 2.4$ part of the muon spectrometer in CMS in order to increase the redundancy in this region. The major advantage of this new technology is its high detection efficiency under high rates of radiation fluxes.

This work is aimed at modeling the response of a Triple GEM detector, ranging from the simulation of a primary ionization, the electron avalanche process to the formation of the signal on the readout electronics. Certain results of this computations will be confronted with real measurements taken with a Triple GEM prototype.

Key-words: high energy physics, LHC, CMS, GEM, Upgrade, muon detector

Acknowledgments

Tout d'abord je tiens à remercier chaleureusement le Dr. Gilles De Lentdecker pour m'avoir offert la possibilité de faire mon mémoire sur un sujet qui m'intéresse et qui m'a fait progresser dans ma compréhension de la physique des particules expérimentale. Je lui suis reconnaissant pour m'avoir guidé tout au long de mon travail, son attention et surtout sa patience qu'il a investi lors de la lecture de mon mémoire. Deplus je tiens à lui remercier pour l'oppurtunité qu'il m'a offerte de visiter le centre de recherche DESY qui m'a motivé à étudier le domaine fascinant de la physique des particules.

Ensuite je tiens à remercier Geoffrey Mullier pour m'avoir introduit au différentes méthodes de simulations qui étaient indispensables pour avoir pu travailler sur mon mémoire. Je le remercie aussi pour les bon moments passés et surtout d'avoir partagé son excellent goût en musique.

I would like to thank the members of the GEM group at the IIHE led by Dr. Gilles De Lentdecker: Erik, Florian, Thierry, Patrizia, Yifan, Ryo, Thomas, Alexandre and Micheal for their warm welcome, their useful advice and their hard work for making the Triple GEM prototype work. A special thanks to Thierry for his small contributions that have nevertheless been very useful.

Notons aussi les physiciens mémorants au IIHE pour les bon moments passés leurs petites contributions qui ont été très utiles pour la rédaction de ce mémoire.

Moreover I would like to thank Cindy as well as my roommates den Kéisëcker and Louis XIV for their great support that helped me find my zen during the lost stressful times of my studies.

In fine voglio ringraziare tutta la famiglia, Mamma, Papa, Nona e Mara per il loro incredibile supporto durante questo lungo viaggio dal primo giorno fino alla fine dei mieli studi, per avermi incoraggiato nelle mie scelte e dato voglia di imparare. Questa tesi è dedicata a loro.

Contents

'If I clap my hands, what is the sound of one hand. If two particles collide, what is the light of one particle.'

Introduction

The *Large Hadron Collider* (LHC) at the *European Organisation for Nuclear Research* (CERN) has been temporarily shut down early 2013. Before this break it collided protons at energies up to 8 TeV in the center of mass reference frame at a instantaneous luminosity $10^{33} cm^{-2} s^{-1}$. During this *first Long Shutdown* (LS1) in 2013-2015 , several adjustments are being made in order for the LHC to reach its nominal energy $\sqrt{s} = 14TeV$ and a nominal luminosity of $10^{34} cm^{-2} s^{-1}$. The *second Long Shutdown* (LS2) is being planned for 2018-2020 to improve collimation and reach a luminosity beyond the foreseen $10^{34} cm^{-2} s^{-1}$.

Since the LHC produces collisions at a rate of 40 MHz, no technology is nowadays available to store and analyze every single event. An efficient trigger system has to be implemented to make a selection of a maximum of interesting events. By doing so it can bring the rate of accepted events down to 100 Hz. This is the the case inside the *Compact Muon Solenoid* (CMS) one of the four LHC experiments where the the trigger system is composed by two trigger levels. The first is the *Level-1 Trigger* (L1 Trigger) which collects information from the calorimeters and muon chambers and analyses it by the use of complex algorithms. This first stage rejects a significant number of uninteresting events and reduces the rate to $100kHz$. The second is the *High Level Trigger*, composed of a farm of computers running event reconstruction softwares.

It is then primordial to have an efficient working trigger system coupled to a data acquisition system. In this work we are going to focus on the forward region of the CMS muon spectrometer. It is composed of three types of gaseous detectors: the *Resistive Plate Chambers* (RPC), the *Dtrift Tubes* (DT) and the *Cathode Strip Chambers* (CSC). The first technology has a low spatial resolution of 1 mm but an excellent time resolution around 1 ns. The CSCs and DTs complete the RPC with a spatial resolution of 100 μm and a time resolution around 10 ns. They are all fast detectors suitable for a muon trigger system.

Muon chambers are very important part of the CMS experiment. They play an important role in the detection of high energy muons, often constituting the *Golden Channel*. In fact processes like the decay of the scalar boson or apparition of new physics are linked to the presence of muons in the final state. After the LS2 when the LHC will run at higher luminosity, the trigger system will be confused due to the increase

of background coincidences in the detectors. This will result in a degradation of muon identification.

Keeping this in mind, we will see that the RPC efficiency decreases significantly at those high rates of particles after the LS2. A new technology of gaseous detectors is currently in development, the *Gas Electron Multiplier* (GEM). Those detectors have comparable time and space resolution to the RPCs but are able to maintain an efficiency of 98 % even at high energy fluxes. Therefore the aim of the CMS GEM collaboration is to fill the forward region of muon spectrometer with Triple GEM detectors.

This work is dedicated to the study of this new detector technology and in particular to the understanding of the signal formation on the anode strips. In a Triple GEM detector the electron signal is complex and it is important to have a good understanding of its formation process to investigate the performance of the new detector in term of time resolution but also spatial resolution. Both very much depend on the charge distribution over the different anodes.

Previously, Triple GEM detector studies were looking at the signal formation using a unique and infinite readout plane. In this work we propose a method to simulate the signal on a multi anode plane as it is in the CMS GEM detectors.

First we use a full 3-dimensional Monte Carlo simulation however very time consuming, to study different gas properties and of the amplification process in the GEM foil. We extract from this 3-D simulation parameters that we the use in a parametrization of a Triple GEM detector. This parametrization is used to simulate quickly the the response of our detector, starting from the primary ionization to the avalanche process in the GEM foil. Then we use the full 3-D simulation to correctly compute the signal formation on the anodes of the Triple GEM detector. This method allow us to quickly generate Triple GEM signals by taking directly into account the complex electric field configuration on the anode plane and contribute to a better understanding of the functioning of this detector technology.

The first chapter provides the reader with a general overview of particle physics in particular the *Standard Model* (SM) and its physical motivation. Chapter 2 gives an overall description of the LHC and CMS while Chapter 3 concentrates on the muon spectrometer. The gas electron multiplier (GEM) will be described in Chapter 4 followed by a brief explanation of the simulation methods used to model the detector.

Preliminary results of this simulation are presented in Chapter 5 followed by the study of a Single-GEM in Chapter 6. Finally using the results of Chapter 5, we will be able to efficiently model a Triple GEM detector exposed in Chapter 7 followed by a confrontation with experimental data.

Chapter 1

The Standard Model

The *Standard Model* (SM) is a quantum field theory describing matter particles and their interaction through force carriers called gauge bosons. Only three of the four fundamental interactions of nature have been incorporated into this theory being the electromagnetic, weak and strong interactions. Gravity has not been able to fit into the SM. The latter has been constructed theoretically throughout the 20-th century and is today the best experimentally verified model of particle physics. It has strongly been shaped and confirmed by the confirmation of many theoretically predicted particles, from the electron in 1897 to the discovery of the scalar boson in 2013.

1.1 Particles of the Standard Model

1.1.1 Matter particles

[1] Matter particles are mainly spin $\frac{1}{2}$ particles known as fermions. 12 of those fermions are described by the SM which attributes to each fermion a corresponding anti-fermion. We have six quarks and six leptons and their basic characteristics are summarized in Figure 1.1.

1.1.2 Interactions

However those particles also known as elementary particles are not sufficient to build up matter as we know it. Since a particle can't manifest its presence by its own, it needs to interact with other matter particles in order to be detected. Additional particles called gauge bosons have to be introduced to create interactions between those matter particles. They result from the fact that the SM is a gauge theory based on the symmetry group $SU(3)_C \otimes SU(2)_L \otimes U(1)_Y$. The generators of those 3 groups represent the force carriers namely eight massless gluons for $SU(3)_C$ carrying the strong nuclear force, three massive bosons for $SU(2)_L$ and one massless boson the photon for $U(1)_Y$, responsible for the electroweak interaction.

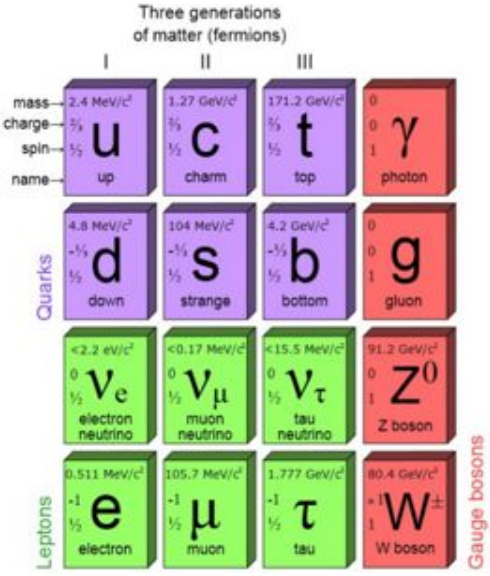

Figure 1.1: Elementary particles of the Standard Model [2]

1.1.3 Spontaneous Symmetry breaking

So far there is no mechanism describing the mass generation of all these particles. Why are some heavier and other are lighter or even massless? In order to give mass to these particles, they have to interact with a scalar field. This is called the spontaneous symmetry breaking (SSB) where the gauge group $SU(2)_L \otimes U(1)_Y$ (4 generators) is broken down to $U(1)_{EM}$ (1 generator) where 3 broken generators arise, known as the Goldstone bosons. This symmetry breaking produces 3 Goldstone bosons which give rise to 3 massive electroweak bosons know as the W^+,W^-, Z and leaves the photon massless. The same mechanism explains the mass generation of the leptons and quarks through a Yukawa interaction between the scalar boson field and a fermion anti-fermion pair.

This mechanism predicted the existence of a new massive particle, quantizing this famous scalar field [1] and completing the last piece of the SM. [3] Its existence has been announced in July 2012 and confirmed in March 2013 at the LHC, having a mass around 125 GeV/c^2 , a spin 0 and a positive parity. It has been proven to decay in the same way as predicted by the SM. However additional measurements have to be made to exactly test its interaction predicted by the SM or whether multiple bosons of its kind exist. One extension of the SM predicts five scalar bosons where each of them has a leptonic decay. Therefore the detection of leptons especially muons in those decay channels will be of importance in the coming years of particle physics, enabling to extend the SM to a more complete theory.

1. Yes, it is the only elementary scalar field in nature. π^0 are described by spin 0 field but are not elementary particles

1.2 Limits and extensions

Despite all those efforts to finally complete the SM, some problems persist. Lets state one of these problems for instance the *Hierarchy Problem* and a SM extension attempting to solve this problem: the *Supersymmetry*.

1.2.1 Hierarchy problem

[4] One vexing problem of the SM is the observed hierarchy between the electroweak scale linked to the mass of the scalar boson $M_{EW} \sim 100\ GeV/c^2$ and the gravity scale linked to the Planck mass $M_P \sim 10^{19}\ GeV/c^2$. In order for the scalar mass to get its experimentally observed scale it has to be fine tuned with respect to M_P by several quantum corrections. However it seems that there are loop corrections to the two-point function with all the fermions of the SM running in the loop that restore the M_{EW} scale to its original scale M_P due to quadratic divergencies. Let H be the scalar field , $\psi\bar{\psi}$ two fermions to which H couples through a Yukawa interaction $L_{SM} \supset \lambda H \Psi \bar{\Psi}$. The leading logarithmic divergence reads:

$$\lambda^2 \int^{\Lambda_{UV}} d^4p \frac{1}{p(p-k)} \sim \lambda^2 \Lambda_{UV}^2 \sim M_p^2 \tag{1.1}$$

where Λ_{UV} is the ultraviolet cutoff of the integral linked to the Planck mass M_P, p the momentum running in the loop and k the incoming momentum.

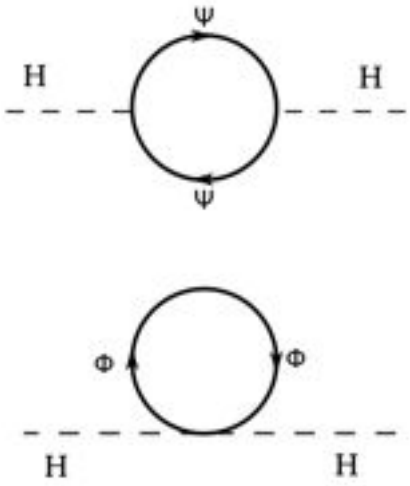

Figure 1.2: top: fermionic 1-loop correction, bottom : bosonic 1-loop correction

1.2.2 Supersymmetric quantum field theory

Supersymmetric quantum field theory (SUSY) is a theory extending the SM which relates integer spin particles to half-integer spin particles. To each particle in the SM, SUSY associates a *superpartner*. When this symmetry is not broken, those superpartners have the same mass and quantum numbers as the particle to which their are linked hence doubling the number of particles in the SM. SUSY is of great interest, since it has an elegant solution for the hierarchy problem. To each fermion, SUSY associates a bosonic counterpart. We can then write an additional bosonic lagrangian term $L_{SM}^{SUSY} \supset \mu H^2 \Phi^2$. The divergence reads:

$$\mu \int^{\Lambda_{UV}} d^4p \frac{1}{p^2} \sim \mu \Lambda_{UV}^2 \tag{1.2}$$

By redefinition of the coupling constants $\mu \sim \lambda^2$ we see that the two contributions cancel each other out in a way that SUSY is able to maintain the hierarchy by protecting it from quantum corrections. Superpartners have not been observed yet so SUSY must be a broken symmetry if it is a true symmetry of nature. Moreover those particles should have masses larger than the ordinary SM particles, estimated around the TeV scale. The *Minimal Supersymmetric Standard Model* predicts five scalar fields. One of these particles decays into SM high energy electrons and muons. Hence the necessity to have an efficient muon detection inside CMS.

Chapter 2

The LHC and CMS

In this Chapter we are going to give an overall description of the Large Hadron Collider (LHC). First of all a short historical note will be given followed by a description of the accelerator complex and some information about the future plans of the LHC. The second part gives a description of CMS by reviewing in detail each detector technology.

2.1 Large Hadron Collider

[5] The *Large Hadron Collider* (LHC) is today the largest particle accelerator and collider in the world. It has been built by the *European Organization for Nuclear Research* (CERN) and is located near the Franco-Swiss border. It consists of a 27 km ring where previously was located its predecessor *Large Electron Positron* collider (LEP). The main particles that are accelerated, using several other accelerators as injectors are protons and heavy ions. The latters are brought into collision at four different locations hosted by four experiments: ALICE, ATLAS, CMS and the LHCb.

2.1.1 A brief history

The construction of the LHC has started in 1998 after its approval in 1994 by the CERN council. Its concept was already been discussed back in the 80's as a successor of the LEP who was already running. Since the 27 km tunnel of the LEP was already in place, it was the most economical place to host the LHC. The LEP was dismantled in 2000 while more and more sections of the new accelerator were assembled in the tunnel. This continued until 2008 when the LHC was finally complete and ready to collide its firts proton beams. In September 2008 it suffered from an incident where 50 superconducting magnets were damaged and had to be shut down for one year.

After this shut down, the LHC to run at the center of mass energy of 7 TeV before shutting down in February 2013. Until the end of 2014 the LHC will undergo a series of upgrades to reach the nominal energy also called the *Long Shutdown 1* (LS1).

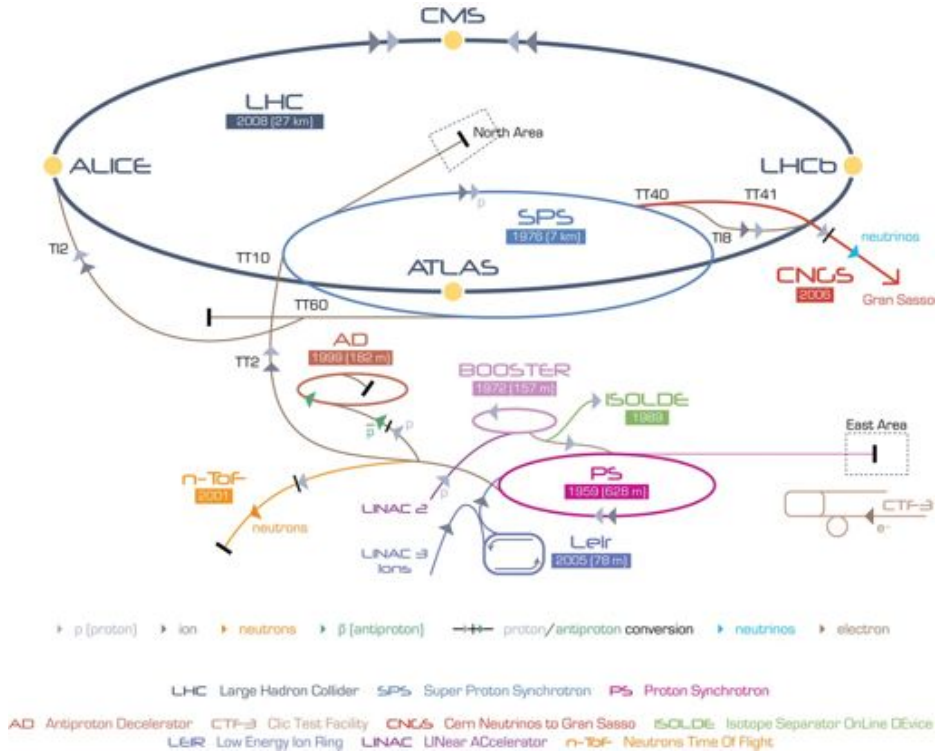

Figure 2.1: LHC injector chain where the smaller accelerators are depicted [6]

2.1.2 Accelerator complex

Before entering the 27 km ring of the LHC, the protons have to be first produced and accelerated. The first step of this process starts in the *Linac2* where gaseous hydrogen atoms are ionized. The resulting protons are then sped up and grouped into bunches and get transferred into a series of synchrotons *Proton Synchrotron Booster* (Booster), *Proton Synchrotron* (PS), and *Super Proton Synchrotron* (SPS). Lastly they enter the LHC tunnel and get seperated into two different tubes travelling in opposite direction.

It is important to mention that the beams are grouped into discrete packages rather than continuous beams. Every bunch of particles entering the tunnel is separated by a time interval of 50 ns. One of the important features of the LHC is its ability to deliver a high density of bunches which is defined by the instantaneous luminosity $\mathcal{L}$. It is straightforward to define the number of expected events per second for a given interaction:

$$f_{process} = \sigma_{process}\mathcal{L}(t) \tag{2.1}$$

where $\sigma_{process}$ is the interaction cross section of the given process, linked to its probability of apparition and expressed in units of surface. Usually the integrated luminosity for circular collider is given by:

$$\mathcal{L} = \frac{N_b^2 n_b f \gamma}{4\pi \epsilon_n \beta^*} F \tag{2.2}$$

where N_b is the number of particles per bunch, n_b number of bunches per beams , f is the revolution frequency, γ_r is the relativistic gamma factor, ϵ_n is the normalized transverse beam emittance, β^* is the beta function at the collision point. F is a geometric correction factor due to the crossing angle of 300 micro radian. It is set up to avoid unwanted parasitic encounters in the same vacuum chamber before they enter separate beam pipes. The large number of bunches per second contributes to this effect. As a consequence we get the number of events expected for a given interaction process:

$$N_{process} = \sigma_{process} \int \mathcal{L}(t) dt \tag{2.3}$$

In the case of an electron collider as LEP, the particles in question are elementary and of the same type. The center of mass reference frame coincides with that of the collision point and its total energy is the exact sum of both beam's energy. However as for example in the LHC, the colliding protons are not elementary so that their respective energy is distributed differently among its partons. Therefore the center of mass reference frame is slightly translated from the collision point. As a consequence the final state particles are predominantly emitted in the forward region of the detector. A major benefit of this is that a large scale of energies can be probed with the same machine.

2.1.3 Future upgrades

[7] The LHC upgrades are summarized in the table below. The LHC operating schedule is divided by three Long Shutdowns. During the LS1 the center of mass energy will reach the nominal energy of 14 TeV and the beam luminosity will be doubled i.e. the time interval between two bunches will be shortened by a factor of 2. The Long Shutdown-2 (LS2) is planned after 2017 where the luminosity will again be increased. In 2021 the LHC will benefit from a another upgrade during the Long Shutdown-3 (LS3) during which the luminosity is planned to be increased by a factor of 10, resulting from an upgrade in th injection chain. This is also called the *High Luminosity LHC* (HL-LHC) era.

Period	Energy	Luminosity
2010-2012	7-8 TeV	0.5 10^{34} $cm^{-2}s^{-1}$
LS1	-	-
2015-2017	13-14 TeV	10^{34} $cm^{-2}s^{-1}$
LS2	-	-
2019-2021	14 TeV	2 10^{34} $cm^{-2}s^{-1}$
LS3	-	-
2021 -	14 TeV	2 10^{35} $cm^{-2}s^{-1}$

2.1.4 Motivations and goals

The four major experiments installed at the LHC pursue different and some common goals. The LHCb is particularly interested in the physics of the b-quark namely its role in the CP symmetry breaking explaining the slight difference between matter and antimatter. *ALICE* [8] is mainly a heavy-ion detector designed to study the physics of a recently discovered new phase of matter called quark-gluon plasma. *ATLAS* [9] and *CMS*[10] have very common objectives. They investigate a wide range of physics, initially aimed at discovering the SM scalar boson but also searching for new physics beyond the SM like SUSY and dark matter particles.

In the following section we will discuss the goals of CMS in more detail.

2.2 Compact Muon Solenoid

[10] The *Compact Muon Solenoid* (CMS) is one of the four major experiments recording the LHC beam collisions. Its structure is segmented into different types of detectors each specifically built for the detection of a certain kind of particle. As it is depicted in Figure 2.2, CMS is composed of five parts starting from the center to the outer layers: the *silicon tracker* (TK), the *electromagnetic calorimeter* (ECAL), the *hadronic calorimeter* (HCAL) the superconductive solenoid and finally the *muon chambers*. In addition to the barrel part of CMS where the detectors are placed in concentric layer around the beam pipe, comes the endcap part to efficiently detect final state particles traveling near the beam line.

2.2.1 Coordinate System

In order to reconstruct the trajectory of particles produced by the head-on proton-proton collisions inside CMS, we need an appropriate coordinate system. The XY plane is used to parametrize the transverse plane orthogonal to the beam line. The Z coordinate follows the direction of the beam.

This Cartesian coordinate system is however not very appropriate for CMS since the latter has a cylindrical geometry where products of the collision are emitted from a point source in a spherical symmetric fashion. Switching to cylindrical coordinates R the radius ,ϕ the azimuth angle and θ the polar angle where $R\phi$ parametrizes the transverse plane, z the longitudinal direction.

Moreover there seems to be a very practical quantity called the *rapidity* which has an interesting property. It is possible to show that the rapidity y is invariant under Lorentz boosts transformation along the z axis.[12]

$$y = \frac{1}{2} ln \left(\frac{E + p_z}{E - p_z} \right) \tag{2.4}$$

For relativistic particles this quantity becomes the *pseudo-rapidity* η.

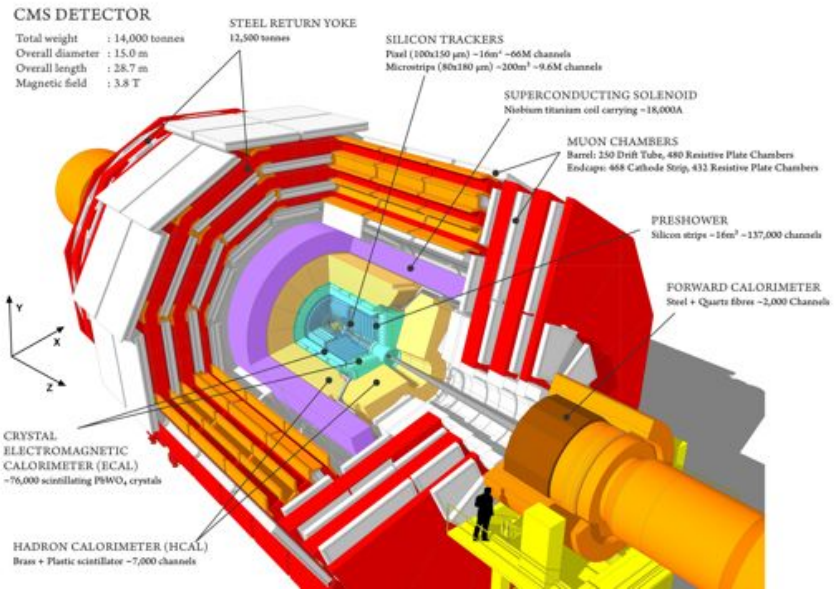

Figure 2.2: the silicon tracker (blue), the electromagnetic calorimeter (green-blue), the hadronic calorimeter (orange), the magnet (purple), and the muon chambers (white) [11]

$$y = -ln\left[tan\left(\frac{\theta}{2}\right)\right] \tag{2.5}$$

It is preferred to use η over the polar angle since the emission of particles is constant as a function of pseudo-rapidity. We conclude that particle fluxes are more important near the endcaps than in the barrel region. This will strongly influence the detectors geometry.

2.2.2 Silicon Tracker

Being the detector closest to the interaction point (IP) where particle fluxes are high, the *Silicon Tracker* is the detector with the most accurate space resolution. Its main task is to track all the particles coming from the IP, reconstruct there trajectory in order to make precise measurements of particle momenta. The tracker is composed of *Silicon Strip Detector* containing the *Silicon Pixel Detector*. The disposition of the different technologies used inside the tracker are represented in Figure 2.4 where the silicon strip detector is depicted in red and the silicon pixel in blue. TIP, TOB, TID and TEC refer to the underlying substructures of the silicon strip detector.

Silicon Pixel Detector

The Silicon Pixel is the detector has a radius ranging from 4 *cm* to 10 *cm*. It englobes the IP where the number of particles per second received at 8 *cm* from the

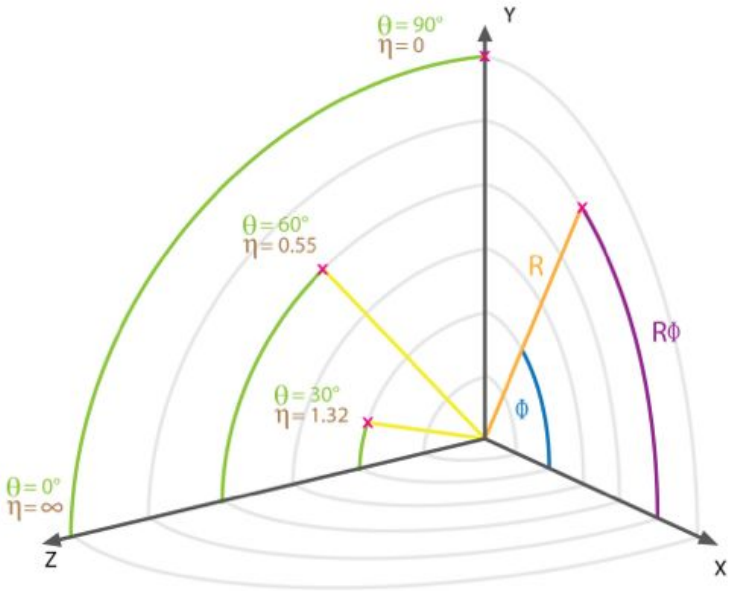

Figure 2.3: CMS coordinate system [13]

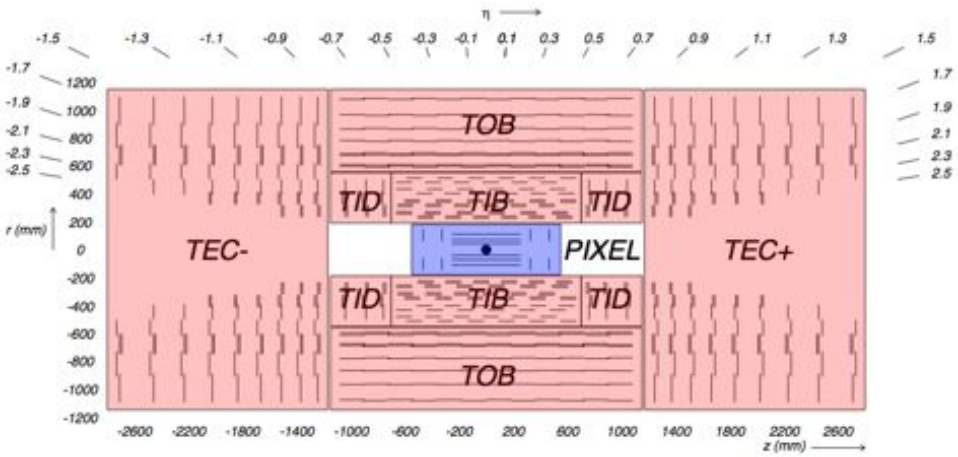

Figure 2.4: Tracker inside CMS where the pixel detector is represented in blue and the silicon strip in red. [10]

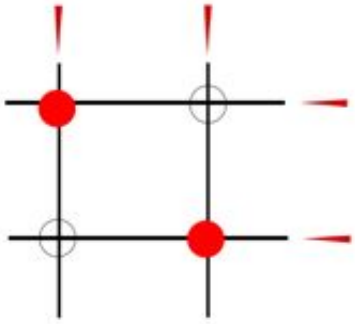

Figure 2.5: two real hits (red) producing four signals and generating two ghosts (blank)

collision point is around 10 million per cm^2. In order to reconstruct this high density of emitted particles an excellent detection efficiency is needed. 65 million small rectangles of 100 μm x 150 μm called pixels, form the silicon pixel detector. Each pixel has its own readout electronics so that the number of output cables increases drastically with the number of pixels (granularity) and hence the number of dead detection spaces. Usually such detectors have an excellent space resolution of 15 to 20 μm .

Silicon Strip Detectors

The silicon pixel detector is englobed by the silicon strip detector. The latter cannot have the same granularity as the first for both technical and financial reasons. As the name already suggests, the detector uses strips separated by 800 to 122 μm instead of pixels. In this way only one coordinate is measured. Some of the strips are crossed by second layer of strips with a small stereo angle enabling them to measure the second coordinate and improving global precision. This disposition enables the detector to reach a spatial resolution up to 23 μm and 53 μm in the direction perpendicular to the strips. However a certain ambiguity arises when two or more particles hit the detector at the same time rezsulting in the generation of *ghost hits* shown on Figure 2.5.

Performance

As stated before, one interesting measurement is the determination of the emitted charged particle's momentum. Since the region inside the tracker is subject to a uniform magnetic field B, the trajectory of the particle is bent due to the Lorentz force. The following relation between the bending radius of the track and the transverse momentum results.

$$p_T[GeVc^{-1}] = 0.3B[T]R[m] \tag{2.6}$$

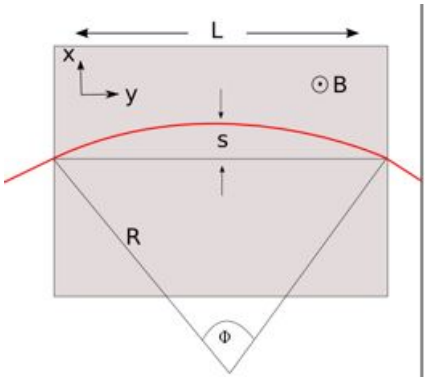

Figure 2.6: charged particle(red track) entering magnetic field region (gray)

We can rewrite the previous relation in terms of the sagitta s : (see Figure 2.6)

$$\left(\frac{L}{2}\right)^2 + (R-s)^2 = R^2 \tag{2.7}$$

since $s \ll L$ and $s \ll R$ we have that $R \simeq \frac{L^2}{8s}$ and the transverse momentum becomes

$$p_t \simeq \frac{0.3L^2B}{8s} \tag{2.8}$$

So by measuring the bending radius or the sagitta we can derive the transverse momentum of the particle. It is easy to see that low energy particles will be easier to reconstruct since their curvature in the detector is less straight. High energy particles will have straighter trajectories. Another unavoidable source of error when it comes to measuring the particle's momentum is due to multiple scattering related to the quantity of matter encountered. Figure 2.8 shows the resolution on the transverse momentum as a function of the pseudo-rapidity. We see that the error on the measurement of p_T increases with η since in the forward region more matter is encountered and hence causing more scattering. The detection efficiency seems to mimic this effect at high pseudo-rapidity where it stays close to 100 % and drops significantly in the endcap region. The increasing strip size can also contribute to this effect.

2.2.3 Calorimeters

In particle physics, calorimeters are used to absorb the entire energy of a particle where a fraction of it gets converted into a signal proportional to that energy deposit. To do this, calorimeters are usually constituted of inactive materials used to provoke depending on the particle's interaction an electromagnetic or a hadronic cascade. Different parameters are used to describe this cascade and are important to know since they will influence the detector's dimension and geometry.

For the *Electromagnetic Calorimeter* (ECAL) we are interested in the radiation length λ_R which reflects the average length that a electron or photon has to travel inside the

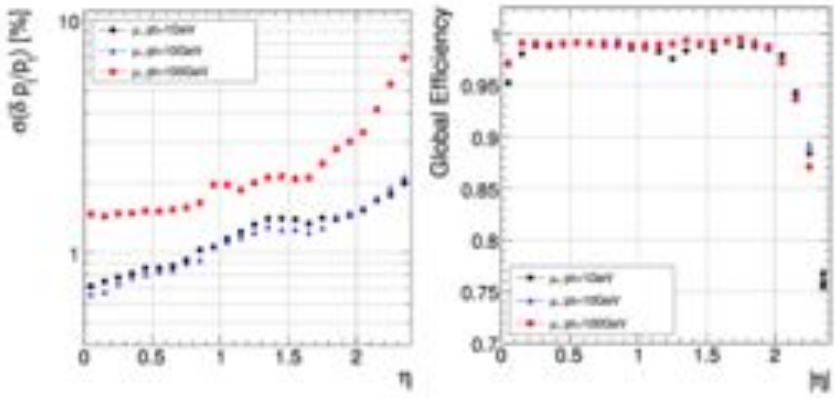

Figure 2.7: relative measurement error on the transverse momentum p_T (left) and detection efficiency (right) of the tracker as a function of pseudo-rapidity for muons with p_T = 1, 10, 100 $GeV\ c^{-1}$ [10]

detector before it emits a photon or respectively create a pair electron/positron. λ_R will decide the depth of the ECAL since we want the detector to contain ideally the entire cascade. The Molière Radius R_M is used to determine the width of the cascade and describes the radius of cylinder in which 90% of the shower is contained.

Whereas for the *Hadronic Calorimeter* (HCAL) we focus on the hadronic part of the detection which splits up in elastic and inelastic interactions. We than use the absorption length λ_a which is the mean distance of a hadron to interact inelastically with the inactive medium in the detector. For the elastic collisions we use the the interaction length λ_I which gives the average distance in which a hadron has went through a elastic scattering. λ_I can be compared to the Molière radius, it contains 95% of the hadronic shower. These two quantities depend on the atomic number Z of the absorber.

The interaction length λ_I is much larger than the radiation length λ_a, the HCAL has a greater depth than the ECAL and is placed behind it else the photons and the electrons would never reach the ECAL.

As a contrast to the tracker, the calorimeter's energy resolution improves with the particle's energy. This resolution is summarized by

$$\left(\frac{\sigma_E}{E}\right)^2 = \left(\frac{a}{\sqrt{E}}\right)^2 + b^2 + \left(\frac{c}{E}\right)^2 \tag{2.9}$$

where a is a stochastic term depending on the production of secondary particles in the shower, b is a constant term related to the uniformity of the crystal and the calibration of the detector, and c comes from the electronic noise inside the detector.

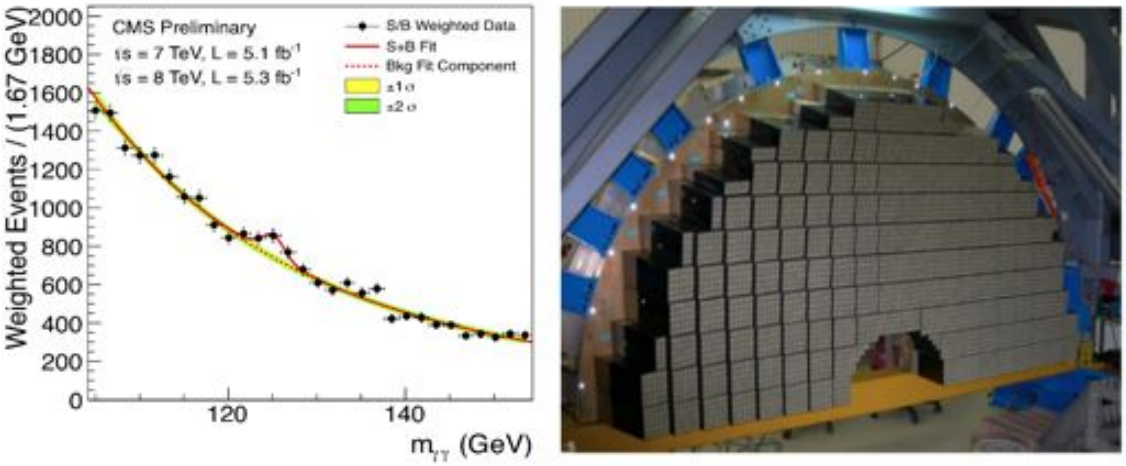

Figure 2.8: Left: Diphoton mass distribution excess observed in CMS around a mass of 125 GeV (black points with error bars). The dotted curve shows the background fit, the solid red line shows the fit rsult for the observed signal with the added background [14]. Right: Endcap ECAL showing the crates in which the crystals are placed.[10]

Electromagnetic Calorimeter

As stated above, the ECAL energy resolution depends on its ability to absorb the entire electromagnetic shower. The leading contributions at high energies to this process are Bremsstrahlung for the electrons and pair creation for the photons. Bremsstrahlung probability is proportional to $\frac{1}{m^2}$ which explains why the shower is only initiated by electrons. Heavier particles like muons ($m_\mu \sim 200 m_e$) and hadrons don't leave any trace in the ECAL. This chain reaction continues as long as the the resulting particle's energy exceeds the energy needed to repeat the process. Photomultiplier tubes are placed behind the crystals to capture the deposited energy.

The active material in the ECAL in CMS are $PbWO_4$ crystals of small section 2.2 x 2.2 cm^2. These type of crystals have the smallest radiation length and Molière radius which results in a small and compact calorimeter. The emission time is very quick, 5 to 15 ns which allows the ECAL to absorb up to 85% of scintillation light in a time interval of 25 ns between 2 bunch crossings.

The ECAL played a major role in the detection of the missing scalar boson of the SM in the decay $h \to \gamma + \gamma$ by reconstructing the invariant mass of the process and detecting an excess of photons in the final state. Figure 2.8 (left) shows the $\gamma\gamma$ mass distribution where an excess of events above background at a mass of 125 GeV is observed inside the ECAL is observed. [14]

Figure 2.9: Insertion of HCAL in CMS [15]

Hadronic Calorimeters

The role of the HCAL is similar to the ECAL except that it is partitioned in different detection layers. Its a succession of 16 layers of absorbers made out of steel plates , Zn and Cu alloy plates whose thickness ranges between 40 to 70 mm. Between each absorber a plastic scintillator of 3.7 mm to 9 mm is placed so that a particle has to travel through 79 cm of matter equivalent to 5.8 radiation length λ_I in the barrel region $\eta = 0$

Pions π^0 are the most encountered particles in the HCAL since they are the most lightest hadrons. Beside their strong interaction in the medium they have also an electromagnetic component as they decay into two photons. The response of the calorimeter is different for the two components and some parameters have to be modified in order to equilibrate their respective response to the detector. The electromagnetic part is better detected hence the hadronic detection efficiency has to be increased by adding Uranium into the absorber for better neutron and low energy photons detection. The electromagnetic detection efficiency can be decreased by combining absorbers with different atomic numbers Z.

2.2.4 The CMS superconducting Solenoid

As we saw in the tracker section, the superconducting solenoid is the heart part of the measurement of particle momenta and charge identification. It creates a uniform magnetic field inside the solenoid of 3.8 T and a more complex vector field outside of 2 T. The metal is cooled down to 4.5 K, temperature at at which it becomes superconductive. The whole solenoid measures 12.5 m in length, inner diameter is 6 m the outer 14 m . It was easy to fit both calorimeters inside the magnet so that particles had to encounter less matter and improve energy resolution. There is however no disadvantage to have placed the muon chambers behind the magnet which act as a filter for particles escaping

the calorimeters and letting only muons reach the muon spectrometer.

Figure 2.10: Insertion of the solenoid into the muon chambers (red) [10]

2.2.5 The muon chambers

To ensure that only muons reach the muon system, the latter has been placed in outer part of CMS. It is composed of several types of gaseous detector. A more detailed description of this will follow in the next chapter.

2.2.6 Trigger System

Estimating the number of channels at 15 millions and a bunch crossing rate of 40 MHz, nearly 600 TB of data is generated per second for 1 *byte* per channel. It is then important to be able to select interesting events out of the massive quantity of data being recorded. Moreover this has to be done in the most rapid way to avoid missing the next wave of coming 25 ns later.

This is done by the trigger system which for CMS is split into two; the *Level 1 Trigger* (HL1) and the *High Level Trigger* (HLT), depicted in Figure 2.11

The first level the data gets saved in a temporary memory located next to the readout electronics for a period of 3.2 μs. This corresponds to 128 bunch crossings at a rate of 40 MHz and is the time necessary for the trigger to decide whether the information is rejected or transfered to the HLT.

This is however a very short interval, only the calorimeters and the muons system contribute to this decision without exploiting their full granularity. The huge number of readout channels inside the tracker makes it too slow to be able to decide at this level.

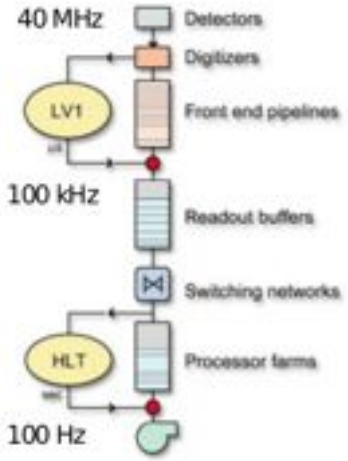

Figure 2.11: Schematic representation of the trigger system and the data acquisition system of CMS [16]

The HLT gets an input at a rate of 100 kHz and completes the analysis of the full data received, including the tracker. It has a deadline of 1 ms before the next bunch crossing and proceeds with the full reconstruction of the events.

Chapter 3

The CMS muon spectrometer

In this Chapter we will review how CMS detects particles by the use of gaseous detectors. First of all we will introduce some historical background of gaseous detectors and how they gained increasingly popularity in particle physics. Then it should be of interest to describe the behind this kind of detectors, how particles interact with them, the amplification process and the formation of signals on the readout electronics. The efficiency and the resolution properties of the detectors will be explained and their importance in CMS. Finally we will give an overall description of the different technologies used inside the CMS muon spectrometer.

3.1 Introduction

CMS relies heavily on its muon detection efficiency especially on its muon chambers. These are exclusively composed of gaseous detectors , exposed in this Chapter.

The idea of gaseous detectors in particle physics started around 1908 with Rutherford and H.Geiger [17] when it came to detect radiation coming from radioactive elements and counting their decay rate. This brought to the invention of the Geiger-Müller counter in 1928 [18] which had a great success for slow decaying rates but failed to be used in high energy physics where scintillation detectors were preferred due to their quicker response.

It wasn't until the 1960 when the *Multi Wire Proportional Chambers* (MWPC) made their first apparition. Invented by G.Charpak [19], MWPC have a space resolution between 0.1 mm and 1 mm, and were considered as new candidates for high energy particle detection. They are still today still an inspiration for the developments of new technologies based on the same detection mechanisms. The benefits of gaseous detector are multiple and will become clear during the present chapter. They offer a competitive alternative to the high cost technology based on solid state detectors.

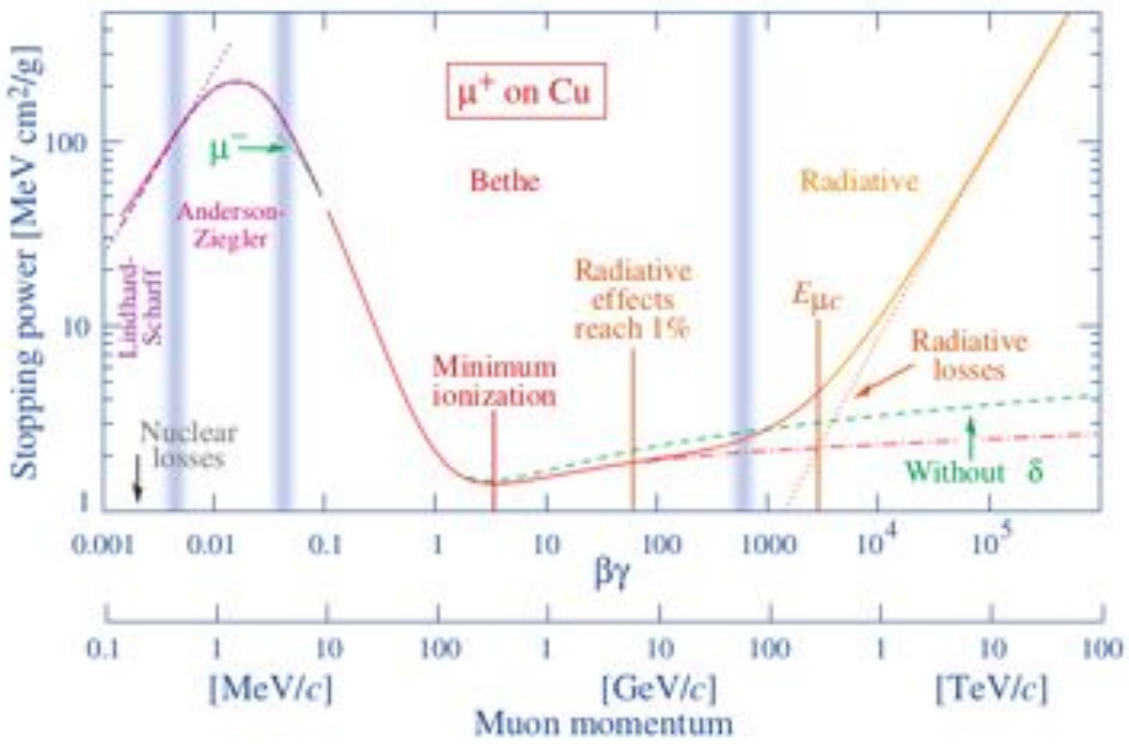

Figure 3.1: mean energy lost for positive muons in copper as a function of $\beta\gamma = p/Mc$. The solid line indicates the total mean energy lost and the dashed curves their respective contribution.[20]

3.2 Particle Detection in Gaseous Detectors

3.2.1 Mean Energy Loss

First of all, let us review some basic description on how particles interact inside a gas volume. For this consider a charged particle heavier than an electron, in our case a muon μ. The muon entering the gas region goes through a multitude of complex interactions . Figure 3.1 shows mean energy lost for different processes as a function of the muon momentum.

It is possible to state how the muon is going to lose on average its energy over the distance traveled in the respective medium . This is described by the Bethe relation which is valid for values of $\beta\gamma = [0.1, 1000]$. [1] [20].

$$-\left\langle \frac{dE}{dx} \right\rangle = Kz^2 \frac{Z}{A} \frac{1}{\beta^2} \left[\frac{1}{2} ln \frac{2m_e c^2 \gamma^2 T_{max}}{I^2} - \beta^2 - \frac{\delta(\beta\gamma)}{2} \right] \tag{3.1}$$

1. $\beta = \frac{v}{c}$ and $\gamma = \frac{1}{\sqrt{1-\beta^2}}$ where v is the speed of the particle.

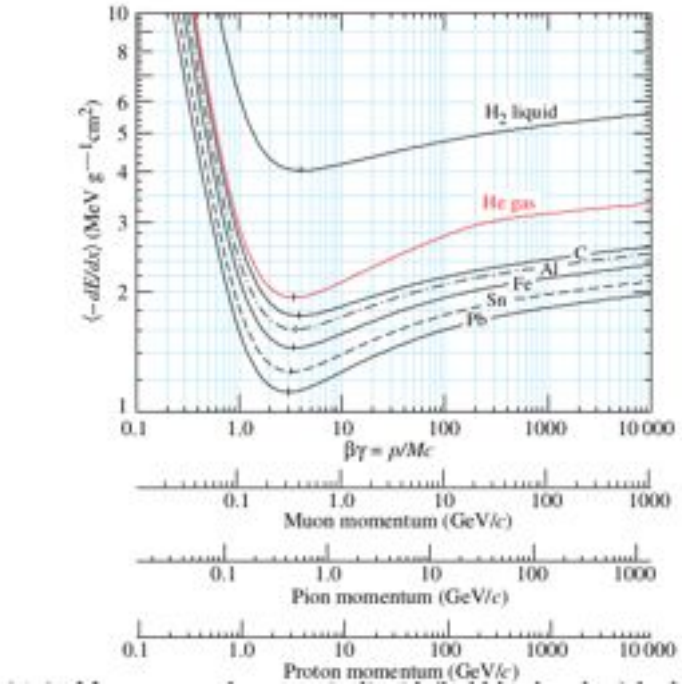

Figure 3.2: Mean energy loss rate in different material, gaseous Helium shwon in red. [20]

where :
T_{max} is the maximum transferable energy to the electron per collision

m_e the electron mass

$\beta = \frac{v}{c}$, v the incoming particle's speed and c the speed of light

$\gamma = \frac{1}{\sqrt{1-\beta^2}}$

I the mean excitation energy

A and Z the atomic mass resp. the atomic number of the gas atoms

$K = 4\pi N_A r_e^2 m_e c^2$, N_A the Avogadro number and r_e the classical electron radius

Figure 3.2 depicts the behavior of relation 3.1 as function of momentum for three different incident particles interacting in several distinct materials.

We notice that for $\beta\gamma < 1$ the energy loss is very high but decreases for increasing values of $\beta\gamma$ until it reaches a local minimum. A particle at this particular point ($3 <$

$\beta\gamma < 4$) is called a *Minimum Ionizing Particle* or MIP. For higher values of $\beta\gamma$ we see an increase in energy loss , entering an relativistic regime $\beta \approx 1$ $\gamma \gg 1$ where the $ln(\gamma)$ dominates.[21] It finally results in a plateau called the Fermi plateau where ultra-relativistic effects occur, polarizing the atoms of the medium. A screening effect takes place, reducing the interaction of the incoming particle with the medium.

3.2.2 Ionization

Muons entering the medium leave a trail of ionization which causes localized energy deposition inside the detector where the most probable value for $\frac{dE}{dx}$ is given by relation 3.1.

For an ionization to occur, the incoming muon has to leave at least a certain amount of energy necessary to eject an atomic electron. This will produce a pair of ion-electron.

$$X + \gamma \rightarrow X^+ + e^- \tag{3.2}$$

The energy dE lost by the muon should be greater than the ionization potential I. If the resulting electron has an energy greater than I, it can in its own ionize the medium, called the secondary ionization. The total amount of electrons created as a result of an ionization are called *primary electrons*. The average number of pairs created can be calculated by [22]

$$\langle N \rangle = \frac{L}{W} \left\langle \frac{dE}{dx} \right\rangle \tag{3.3}$$

where W is the required energy for a pair creation, L the length of the trail of the incident particle in the medium. Some valuues of W are shown on the table above. [23] For a medium composed of K mixed independent gases we can generalize this equation by summing over all contributions.

$$\langle N \rangle = \sum_i^K \frac{LP_i}{W_i} \left\langle \frac{dE}{dx} \right\rangle \tag{3.4}$$

It is also instructive to define the number of created pairs per unit length

$$n_T \equiv \frac{\langle N \rangle}{L} \tag{3.5}$$

Gas	$W(eV)$	n_T (cm^-1)
Ar	26	97
CH_4	30	54
CO_2	34	100
CF_4	54	120
He	41.3	8
Ne	37	40
Xe	22	312

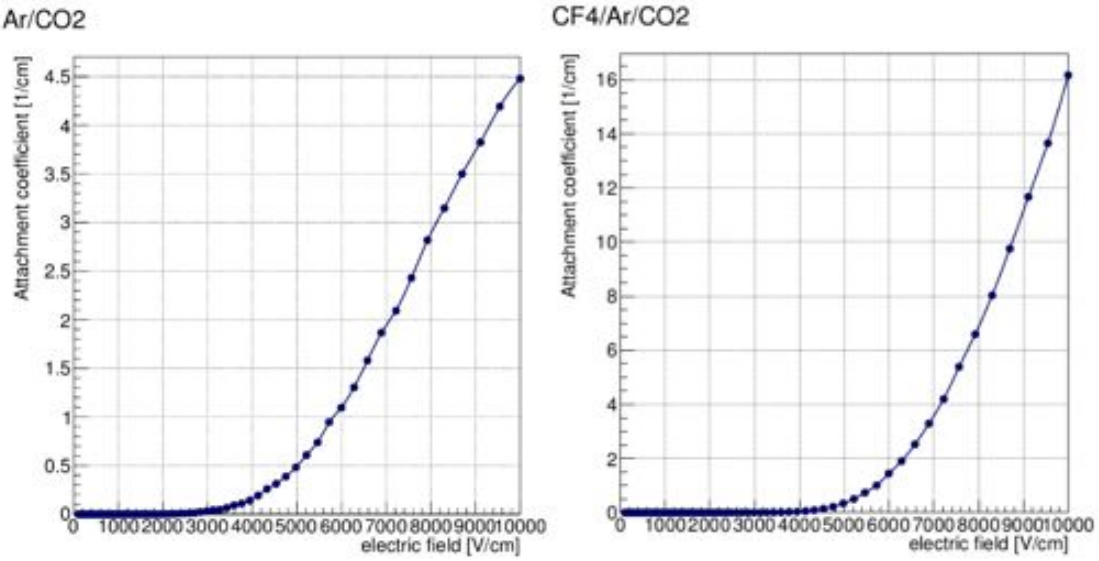

Figure 3.3: Attachment coefficient as a function of the electric field applied inside the respective gas mixture; Left: $ArCO2$ 70:30 . Right: $ArCO_2CF_4 45:15:40$ [25]

3.2.3 Penning Effect

[24] [22] There is another contribution to the production of electrons inside the medium, called the *Penning Effect*. In certain cases where an excited atom can't return to its ground state quick enough due to a conservation of spin parity, it ionizes another neutral atom

$$X^* + Y \rightarrow X + Y^+ + e^- \tag{3.6}$$

In either case, the excited atom can return to its ground state by emitting a photon, inducing an ionization

$$X^* \rightarrow X + \gamma \tag{3.7}$$

$$\gamma + Y \rightarrow B^+ + e^- \tag{3.8}$$

For the Penning Effect to have a significant contribution to the creation of electron-ion pairs, the collision time of A^* and B has to be smaller than the photon emission time of A^*.

3.2.4 Other processes

[26] [27] [28] Other and more complex processes involve an electron from an outer atomic oribtal replacing an ejected electron due to a prior ionization. This results in an emission of a photon, the Auger effect. This photon can escape the sensible gas volume or create in its turn another double ionization.

$$X + \gamma \rightarrow X^{+*} + e^- \rightarrow X^{++} + 2e^- \tag{3.9}$$

Another example is the attachment of an electron on a neutral atom.

$$X + e^- \rightarrow X^- \tag{3.10}$$

where a free moving electron inside the gas volume is lost and binded by the neutral atom. Usually the resulting negative ion is not stable like in the case of CF_4 that will be of interest in the following section.

$$CF_4 + e^- \rightarrow \left(CF_4^-\right)^* \rightarrow CF_3^+ + F + 2e^- \tag{3.11}$$

where X^* denotes that X is unstable. The two resulting electrons contribute to the amplification of the signal. An attachment coefficient related to the probability of this kind of reaction can be computed and is show on Figure 3.3 for two different gas mixtures.

3.2.5 Avalanche

Formation of the avalanche

[20] The total number of produced primary electrons is not significant to be detected by any readout electronics. [2]

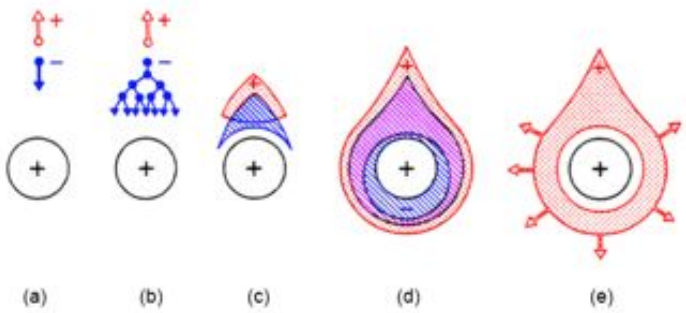

Figure 3.4: a) Primary electrons and ions drift apart , b) electrons being faster than the ions have already triggered an avalanche drifting towards the anode, c) the electron cloud starts to englobe the anode d) and e) the electrons get absorbed by the anode and the repulsion between the anode and ions is no longer screened, the ions start to drift away. During this time the detection electrode is said to be dead since no other signals can be formed. As long as the ions haven't been evacuated, the detector cannot operate [29]

Therefore the number of electrons has to be multiplied inside the gas chamber by the use of very intense electric fields (several tenths of kV/cm). In this region of high field intensity, the electron gain enough energy to ionize further the gas by creating

2. Several hundred electrons are usually produced by an ionization in a gas volume of few mm thickness. The electronic noise intrinsic to the readout electronics will mask completely this signal

an avalanche process. Once this process has started, the number of electron-ion pairs increases exponentially. Figure 3.4 shows the development of an avalanche around an anode wire, typically encountered in gaseous detectors.

Moreover the charge multiplication has a certain limit where it can no longer continue. This can be seen on Figure. The electrons are moving faster than the ions, and accumulate around the anode and leave the ions near the cathode. An additional electric field $\vec{E_d}$ rises due to the charge separation of the ions and the electrons. When those two electric fields compensate $E_d = E_a$, the process stops and the charges start to recombine. This usually happens for a gain factor of 10^8

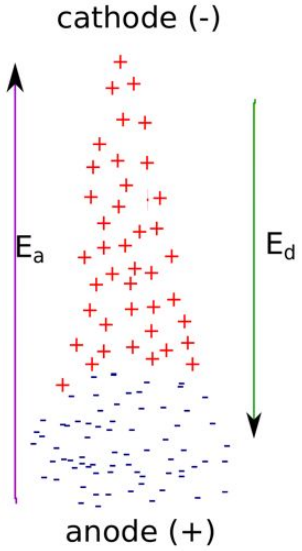

Figure 3.5: formation of an avalanche, E_a is the electric field applied between the electrodes, E_d is the electric field produces by the charge "droplet".

Gain

The gain of the amplification stage is defined by $\frac{N}{N(0)}$ where N is the number of electrons in the final state and $N(0)$ is the number of primary electrons. The number of electrons produced is proportional to l , the length of the region of the amplification. We have that

$$dN = N\alpha(x)dx \tag{3.12}$$

where dx is the infinitesimal path. α is the *Townsend coefficient* and is defined as $\frac{1}{\lambda}$. λ is the mean free path of the electron traveling inside the medium. α depends of the charge distribution of the medium and of the cross section of the different reactions. It can only been calculated experimentally or by numerical computation. By integrating the latter equation we get that:

$$G(x) = \frac{N(x)}{N(0)} = e^{\int_0^l \alpha(x)dx} \tag{3.13}$$

There seems to be a certain regularity when comparing different values of α. Polyatomic gases have more degrees of freedom (rotation, vibration etc) and tend to absorb energy, prevent ionization easier than mono-atomic gases, hence have smaller Townsend coefficient. However for mono-atomic gases, when they recombine with electrons, emit UV photons able to damage some components of the detector and even create another avalanche when hitting a metallic part. This is why a polyatomic gas is added. It plays the role of a quencher able to absorb the radiation. Nevertheless it has also a disadvantage of degrading the material of the detector over time.

3.2.6 Drift and Diffusion of charges in a gas

Once the avalanche started, the electrons and ions have to drift to their respective electrode. They are submitted to a multitude of elastic scattering inside the gas which will provoke a spreading in the charge cloud. This is will be important in the next Chapter when discussing the spatial resolution of detectors.

Drift without external Field

In a gas at thermal equilibrium and without external field, the speed distribution of the ions and electrons is described the Maxwell speed distribution law. [30]

$$P(v)dv = n\sqrt{\frac{2}{\pi}}\left(\frac{m}{k_B T}\right)^{\frac{3}{2}} v^2 e^{-\frac{mv^2}{2k_B T}} dv \tag{3.14}$$

where n is the number of molecules in the gas, k_B the Boltzman constant, m the molecular mass. It is easy to see why ions move quicker than electrons by averaging the above distribution and finding the mean speed

$$v_{mean} = \sqrt{\frac{3k_B T}{m}} \tag{3.15}$$

which is proportional to the inverse of the square root of the mass. This will help us to understand how the diffusion evolves in time.

The most general and simple model for this situation is described by the Brownian motion equation: [31]

$$\frac{\partial \phi}{\partial t} = D\nabla^2 \phi \tag{3.16}$$

where ϕ is the density of particles D the diffusion coefficient of particles spreading in a gas. The solution in one dimension of this parabolic differential equation is given by a Gaussian function

$$\phi(x,t) = \frac{n}{4\pi Dt} e^{-\frac{x^2}{4Dt}} \tag{3.17}$$

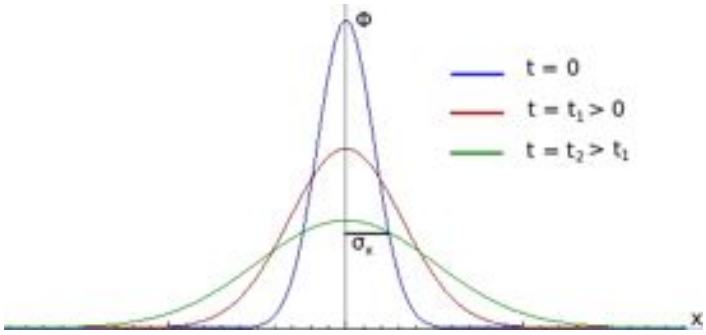

Figure 3.6: diffusion of the density of free charges over time in one dimension

where the standard deviation is

$$\sigma_x^2(t) = 2Dt \tag{3.18}$$

and can be generalized in three dimensions [3]

$$\sigma^2(t) = 6Dt \tag{3.19}$$

Supposing that the probability between an short interval of time dt of having the first collision is

$$p(t)dt = \frac{1}{\tau} e^{\frac{-t}{\tau}} dt \tag{3.20}$$

where τ is a normalization factor. Using this we can compute the diffusion after the first collision in a given direction of space by computing the standard deviation.

$$\delta_x^2 = \frac{1}{3} \int_0^\infty x(t)^2 p(t) dt \tag{3.21}$$

where the factor 1/3 counts for the three possible degrees of freedom. The mean speed can be replaced in this case by using the mean free path λ by $v_{mean} = \frac{\lambda}{\tau}$. Then after a time t the traveled path is $x(t) = tv_{mean}$. Equation 3.17 gives

$$\delta_x^2 = \frac{1}{3} \int_0^\infty \left(\frac{t\lambda}{\tau} \right)^2 p(t) dt = \frac{2}{3} \lambda_0^2 \tag{3.22}$$

So that after a time $t \gg \tau$, t/τ collisions have occurred and the total diffusion at time t is given by

$$\sigma(t)_x^2 = \frac{2}{3} \frac{\lambda^2}{\tau} t \tag{3.23}$$

Using 3.15 and 3.16

3. An alternative expression exists for this whci expresses D as $D = \frac{\sigma_x}{\sqrt{z}}$ where z is the drift distance

$$D = \frac{\lambda^2}{3\tau} = \frac{1}{3} v_{mean} \lambda = \frac{1}{3} \sqrt{\frac{3 k_B T}{m}} \lambda \tag{3.24}$$

Drift In an Electromagnetic Field

[32] [33] [30] The equation of motion of a particle in an electromagnetic field is described by the Lorentz force. If we add an friction term K $\mathbf{v}$, the second law of Newton becomes

$$m \frac{d\mathbf{v}}{dt} = e\left(\mathbf{E} + \mathbf{v} \times \mathbf{B}\right) - K\mathbf{v} \tag{3.25}$$

where m is the mass of the particle, $\mathbf{v}$ its speed and e its electric charge, $\mathbf{E}$ and $\mathbf{B}$ the electromagnetic field. K $\mathbf{v}$ describes the collision of the particle with the gas molecules and has the dimension of a force hence we can state that $K \equiv \frac{m}{\tau}$. where τ is the mean time between two collisions. By taking a $t \to \infty$ the left-hand-side of the equation becomes negligible at equilibrium and we are left with a system of linear equations by restating $\frac{e}{m}\mathbf{E} \to \mathbf{E}$ and $\frac{e}{m}\mathbf{B} = \omega$.

$$m\mathbf{E} = \mathbf{\Omega E} \tag{3.26}$$

where $\mathbf{\Omega}$ is

$$\begin{pmatrix} \frac{1}{\tau} & -\omega_z & \omega y \\ \omega_z & \frac{1}{\tau} & -omega_x \\ -\omega_y & \omega_x & \frac{1}{\tau} \end{pmatrix} \tag{3.27}$$

by inverting this matrix we get the drift velocity.

$$\mathbf{v_D} = \frac{\mu E}{1 + \omega^2 \tau^2} \left(\mathbf{u_E} + \omega\tau(\mathbf{u_E} \times \mathbf{u_B}) + \omega^2\tau^2(\mathbf{u_E} \cdot \mathbf{u_B})\mathbf{u_B}\right) \tag{3.28}$$

where $\mu \equiv \frac{e\tau}{m}$ is the mobility of the particle in the medium and $\mathbf{u_E}$,$\mathbf{u_B}$ are the unitary vectors giving the direction of the respective fields.

- $B = 0$ we immediately get

$$\mathbf{v_D} = \mu\mathbf{E} \tag{3.29}$$

Using previously obtained expressions for the standard deviation of the diffusion σ_x and the diffusion coefficient D

$$\sigma_x = \sqrt{2Dt} = \sqrt{2\frac{kT}{e}\frac{z}{E}} \tag{3.30}$$

where we used that $t = \frac{z}{v_{mean}} = \frac{z}{\mu E}$ and z is the drift length of the electrons or ions. Hence the diffusion width is proportional to the drift length.

- $\mathbf{B} \parallel \mathbf{E}$

We will now show that the drift velocity can be expressed as a function of the electric field and the pressure inside the gas which will be of importance later in this work.In this case 3.29 still holds. The drift direction is not changed. Additionally using μ

$$\mathbf{v_D} = \frac{e\tau}{m_e}\mathbf{E} = \frac{e\lambda}{m_e v_{mean}}\mathbf{E} \tag{3.31}$$

Going further we know that for elastic collision $\lambda = \frac{1}{n_v \sigma}$ where n_v is the number of atoms or collision centers per volume in the medium and σ the cross section related to this collision which for hard sphere collision $\sigma \sim \pi R^2$. R is the radius of the collision centers.

$$\lambda \sim \frac{1}{n_V \pi R^2} \tag{3.32}$$

This can be rewritten by relating n_V to the Avogadro number N_A and the ideal gas law $PV = nRT$, P pressure, V volume, n number of atoms in the gas, R the ideal gas constant.

$$\frac{1}{n_V \pi R^2} = \frac{V}{nN_A}\frac{1}{\pi R^2} = \frac{RT}{\pi R^2 N_A P} \tag{3.33}$$

We conclude that since v_D is proportional to the electric field E and $\frac{1}{P}$

$$v_D = v_D(E/P) \tag{3.34}$$

• $\mathbf{B} \nparallel \mathbf{E}$ the drift velocity is deviated in respect to the component orthogonal to the the $(\mathbf{u_B}, \mathbf{u_E})$ plane and the other to the direction of the magnetic field. Intuitively we can see that this will reduce the transverse diffusion of the charge cloud due to the helicoidal trajectory of the particles. The results of this statement will be exposed later in this work. Note that a non negligible magnetic field is present inside the muon chambers.

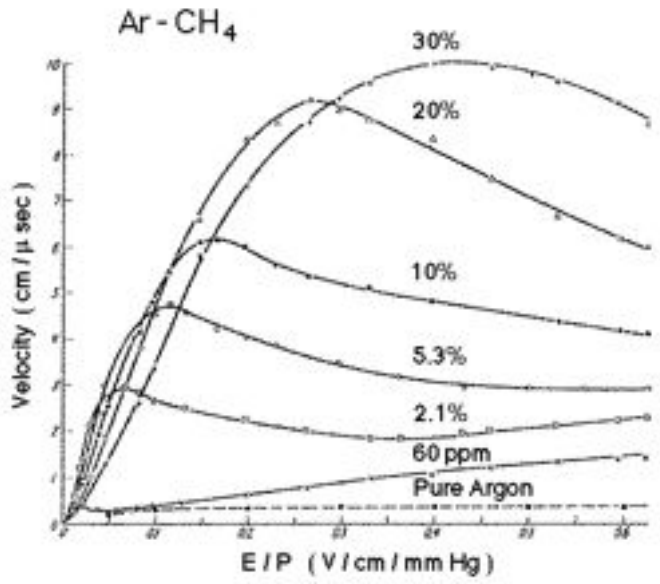

Figure 3.7: drift velocities as a function of E/P for different $Ar - CH_4$ gas proportions [29]

3.3 Signal Formation

3.3.1 Signal Induction

[34] The signal does not result from the charge collection on the electrodes but rather from the drifting of the electrons and ions. To show this we have to derive the surface charge density created by a moving charge q towards an infinite large grounded metal plate. We have to solve the Poisson equation with boundary condition $\phi = 0$ on the conductor surface $z = 0$

$$\Delta\phi = -\frac{\rho}{\epsilon_0} \tag{3.35}$$

where ρ is the volume charge distribution, ϕ is the electric potential related to the electric field by $\mathbf{E} = -\nabla\phi$. By using Gauss Law

$$\int_S \mathbf{E} \cdot d\mathbf{A} = \frac{1}{\epsilon_0} \int_V \rho dV \tag{3.36}$$

since charges are only distributed over a surface plane A, rather over the entire volume we get that $EA = \frac{\sigma A}{\epsilon_0}$

$$\sigma(x, y) = \epsilon_0 E \tag{3.37}$$

The electric field is found by placing an opposite charge on the other side of the plane at a exact same distance in order to create the right boundary condition $\phi(z = 0) = 0$.

This is the method of images which allows us to write down the electric field of a point charge at distance z_0 from the plane.

$$E_z(x,y) = -\frac{qz_0}{2\pi\epsilon_0(x^2+y^2+z_0^2)^{\frac{3}{2}}} \tag{3.38}$$

As a result we get the total charge induced on the plane

$$Q = \int_{\mathbb{R}^2} \sigma(x,y)dxdy = \int_{\mathbb{R}^2} \epsilon_0 E_z(x,y) = -q \tag{3.39}$$

The total charge induced is independent of the distance of the point charge from the plate, however the surface charge distribution depends on z_0.

We see that the total charge remains constant through time , in other words there is no induced current on a infinite large plane. To have a current we need to segment this plane in finite and grounded strips. The total charge distribution doesn't change globally when summing all the contribution of the individual strips. However locally on an electrode of size l

$$Q(z_0) = \int_{\mathbb{R}} \int_{[-l/2,l/2]} \sigma(x,y)dxdy = -\frac{2q}{\pi} \arctan\left(\frac{w}{2z_0}\right) \tag{3.40}$$

by changing variables $z(t) = z_0 - vt$ and using the chain rule

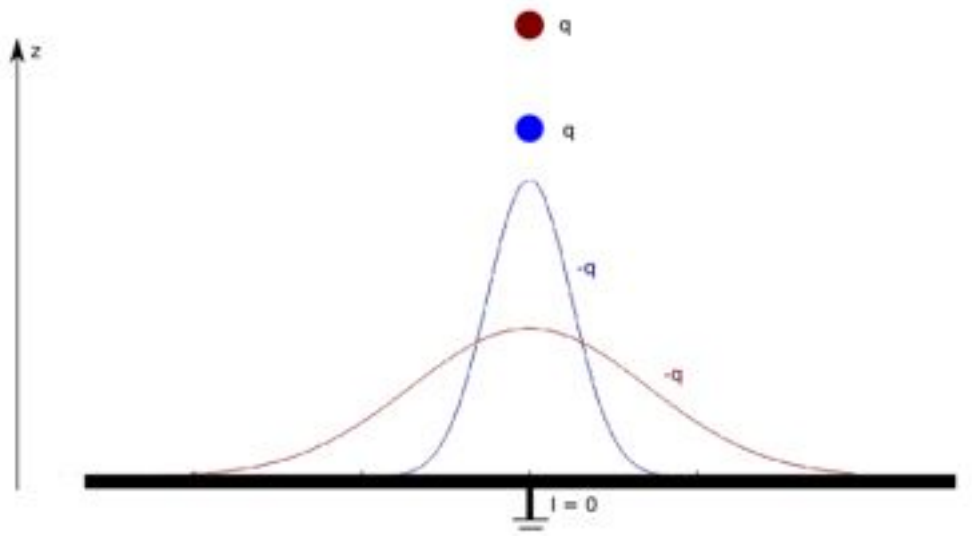

Figure 3.8: surface charge distribution on an infinite conductor produced by a point charge q. The surface of the curves represents the total amount of charge induced on the conductor plane. The spreading of the distribution and the increase of its height is due to the approaching of the charge

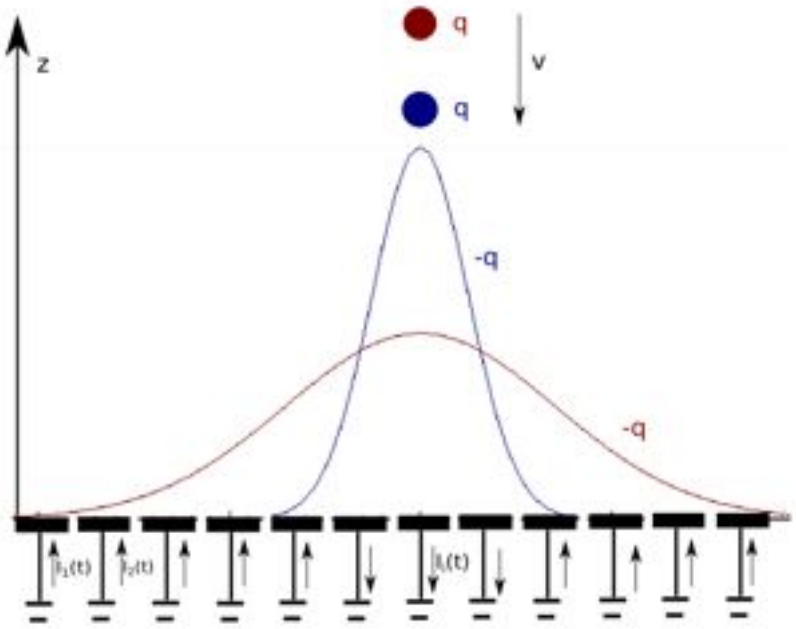

Figure 3.9: surface charge distribution produced by a moving charge on a segmented grounded metal. Current direction is inverted when $\sigma_{z_1} < \sigma_{z_2}$ and $z_1 > z_2$

$$I_i(t) = -\frac{d}{dt}Q_i(z(t)) = -\frac{\partial Q_i(z(t))}{\partial z_0}\frac{dz(t)}{dt} = \frac{4ql}{\pi\left(4z^2(t) + l^2\right)}v \tag{3.41}$$

We conclude that the movement of the point charge induces a flowing current between the strips and the ground.

[35] There is a more practical way to derive the induced current on a conductor. In order to do this we need to apply the Shockley-Ramo theorem. Considering a series of n electrodes like in the previous example and wanting to compute the induced current on the ith one, we need to remove nth charge q from the setup and set all electrodes to zero except V_i. A certain weighting field $\mathbf{E}_i$ will arise from this which can be solved analytically for simple boundary conditions but requires numerical simulations for more complex geometries. If $\mathbf{x}(t)$ is the position of the charge, $\mathbf{x}(t)$ its velocity, the induced current $I_i(t)$ on the ith electrode is.

$$I_i(t) = -\frac{q}{V_i}\mathbf{E}_i[\mathbf{x}(t)]\mathbf{v}(t) \tag{3.42}$$

The underlying idea to this equation is that in order to induce an electric current , the moving charge cannot move perpendicular to the weighting field, the field lines where $\mathbf{E}_i$ is constant, called the equipotentials. Moreover this enables us to retrieve easily the induced current only by computing the weighting field and the drift velocity.

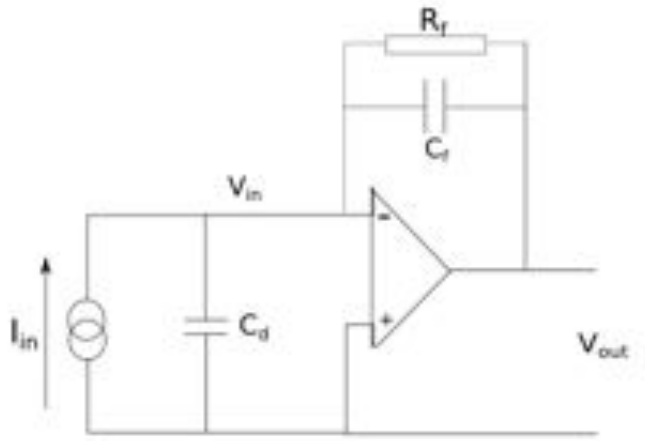

Figure 3.10: Charge-sensitive preamplifier [32]

The electrodes are then 'scaled' down to simple nodes where their respective induced current are placed as ideal currents. All the electronic components are added to the circuit usually capacitances. The measured current is then obtained by computing all the capacitances between the nodes $C_{i,i+1}$ and taking into account all the weighting fields. Since the avalanche is formed by multiple charges, the induced current is calculated by summing up all the individual current.

3.3.2 Readout electronics

[36] An ionizing particle for instance a muon passing through the gas volume will ionize the medium, it encounters and produce up to several hundreds electrons per *cm* traveled [4].In gaseous detectors this signal is amplified internally by the different processes described previously. In principle the resulting signal doesn't need to be amplified later. Nevertheless a series of amplification and transformations are applied by the readout electronics before being digitized and arriving a the first trigger level.

Since the detectors we just discussed are mainly charge producing devices, we choose a charge-sensitive preamplification. The main benefit of this choice is that the computation of the output voltage does not depend on the detector capacitance (Fig 3.8). It functions as an integrator and its output voltage can be derived easily.

$$v_{out}(t) = -\frac{1}{C_f}\int i_{in}(t)dt = -\frac{Q}{C_f} \tag{3.43}$$

4. See Chapter 5 for more details

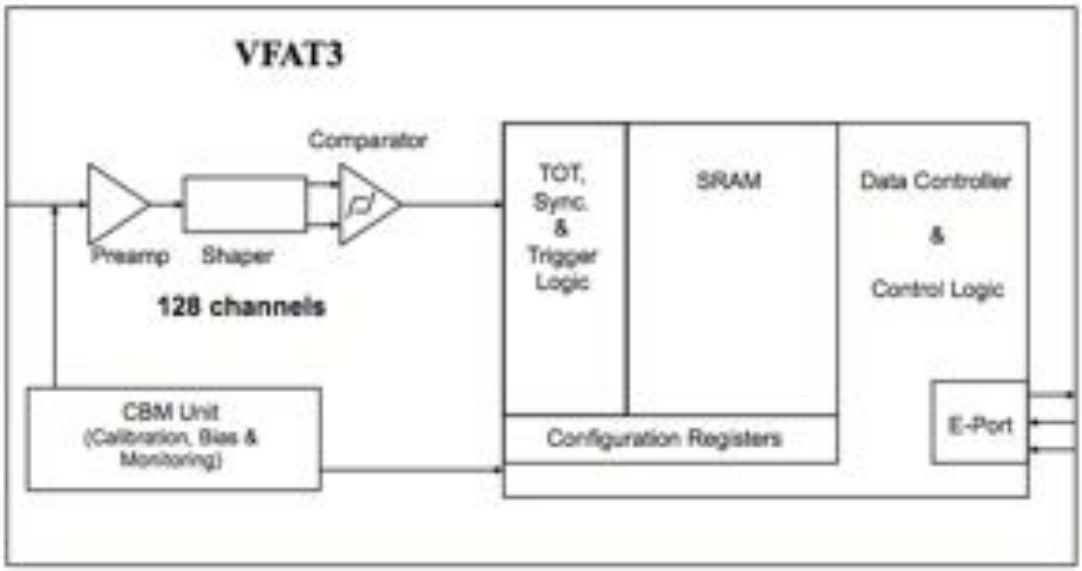

Figure 3.11: View of the on-board electronics needed for the readout of the strips' signal. The architecture has 128 analogical channel readouts which are connected individually to one strip. [36]

where I_{in} is the input current and C_d the detector's capacitance which determine the input voltage V_{in} entering the preamplifier. The feedback capacitance C_f collects the charge produced by the detector and discharges itself through the feedback resistance R_f with a typical time constant $\tau = R_f C_f \sim \mu s$. The outgoing signal is a exponentially decreasing charge as a function of time. However the time constant in other words the signal duration is too long for the LHC bunch crossing rates where the interval between two collision events is 25 ns .

This is why a shaper is added to the electronics to decrease the signal duration. In this way the signal output will enable us to distinguish between two signals separated by a small interval and avoid a pileup. However this signal shaping is followed by a presence of undershoot which can be corrected by a more complex method called the *Pole Zero cancellation* and will not be discussed further.

The comparator follows the shaper which digitizes the signal and can then be stored in memory (SRAM). It is sent through optical links (E-Port) to the off-detector electronics located in a cavern near next to the CMS detectors.

The above described electronic architecture is often very complex and would be impossible to simulate. Supposing that the amplitudes we are dealing with allow us us to regard the electronics' behavior in a linear regime it will be straightforward to model the system by a response function. This function can be obtained by shooting a very short signal δ through the electronics and mapping its output. This is called the *Signal Convolution* which in mathematical terms can be expressed by the $*$ operation defined

by:

$$(f * g)(t) = \int_{\infty}^{\infty} f(t - t')g(t')dt' \tag{3.44}$$

Replacing in the above equation f by a quick signal function for instance a δ-Dirac function and convoluting it with the unknown response function T

$$(\delta * T)(t) = \int_{\infty}^{\infty} \delta(t - t')T(t')dt' = T(t) \tag{3.45}$$

we retrieve the response function at the electronics' output which can be in turn be used to convolute any given input signal. This will help us to model the resulting output signal of the detector after being subjected to a series of amplification and shaping stages.

3.4 Efficiency and Resolution

3.4.1 Spatial Resolution

[32]

The spatial resolution is defined as the error on measurement of the spatial coordinate made by the detector. As we saw earlier, the electron cloud also called the *electron cluster* has a tendency to spread while it is drifting inside the gas volume inside an electric field. The transverse spread of the these charges will impact the shape of the signal read-out on the electronics. This has enormous consequences on the detectors spatial σ_{res} resolution. Supposing that the spread is gaussian we can show by the Central Limit Theorem that if for n the standard deviation of the electron cluster in one transverse direction becomes $\frac{\sigma_x}{n}$.

This explains why it is important to have a high number of electrons and hence reduce the spread. When the cluster charge spreads uniformly only around one single strip, the spatial resolution is given by the size of the pitch strip divided by the variance of a uniform distribution $\sqrt{12}$, the pitch being the distance between two strips plus the width of the strip.

$$\sigma_x = \frac{pitch}{\sqrt{12}} \tag{3.46}$$

Another typical approach for the coordinate determination of the particle's hit is the method of *Center of Gravity*. The latter exploits the fact that the current is not induced on one single but on multiple separate electrodes.

The position of the hit is determined by averaging the the induced charge on multiple electrodes.

$$\mathbf{x}_{reconstr} = \frac{\sum_i \mathbf{x}_i q_i}{\sum_i q_i} \tag{3.47}$$

where q_i are the individual charge weights on electrode i , x_i the geometric center of electrode i. Using this method it is possible to obtain better spatial resolution than 3.46.

The spatial resolution is related to the resolution on the momentum. It is important to ensure a good spatial resolution when detecting hits of the particle whose trajectory we want to reconstruct and momentum. We already determined that the spread is proportional to the drift distance, so that for gaseous detectors the spatial resolution will depend on the space interval between the electrodes.

3.4.2 Time Resolution

The LHC *Bunch Crossing* (BX) rate is 40 MHz. The challenge is to assign the correct particles to the corresponding BX and in order to do so the detectors have to have an excellent time resolution.

3.4.3 Detection efficiency

The detection efficiency is required to be at least 95% for CMS which means that out of 100 particles 95 are detected. The efficiency mainly depends upon the detector's ability to maintain its gain even at high radiation rates. (See rate capability)

3.4.4 Rate capability

The rate capability of a detector is defined as the maximum flux rate of particles under which the detector can operate without a significant loss of gain or detection efficiency. In gaseous detectors, the ions created by the avalanche drift up to 1000 times slower than the electrons. If they aren't evacuated fast enough their charge distribution can lower the interior electric field by a screening effect and consequently diminish the gain.

3.5 CMS Muon System

[10] [37] The CMS Muon System is composed exclusively of gaseous detectors namely, *Cathode Strip Chambers* (CSC), *Drift Tubes* (DT) and *Resistive Plate Chambers* (RPC) that will be described in the following sections.

3.5.1 Cathode Strip Chambers

Cathode Strip Chambers are trapezoidal proportional detectors consisting of 6 gas gaps where anode wires are stretched radially throughout the chamber. Cathodes strips are segmented and placed perpendicularly to the anode wires on the inner boundary of the chamber. CSCs have a detection surface up to $3.4 \times 1.5\ m^2$ and have an excellent rate capability which explains the fact that they are placed in the endcap disks of CMS. A muon passing though the chamber produces an avalanche between the anode and cathode.(see section 3.2.5) The electric field between the wires and the strips triggers the avalanche near the anodes and an image charge on the cathode strips. The spatial resolution from each chamber varies between 100 and 200 μ.

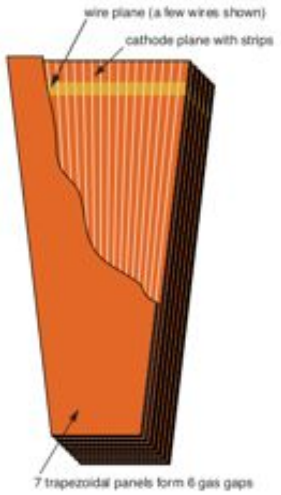

Figure 3.12: Schematic view of the CSC [37]

3.5.2 Drift Tubes

Drift Tubes are rectangular chambers filled with a mixture gas $Ar : CO_2$ (85:15). The anode wire is placed in the center between two cathode strips producing a strong electric field of 1.5 kV cm^{-1}. The functioning of the DTs are similar to the CSCs, the electric field causes the charges to drift inside the gas where the electrons produce avalanches near the anode. Figure 3.10 shows a schematic view of a DT. The electrode strips near anode help to uniformify the field and improve the drifting of the charges.

The drift time of the electrons enables to measure the distance of the muon trace from the anode. However one DT alone, having a spatial resolution of 250 μm,is unable to determine from which side of the anode the muons has passed. This is why DTs are grouped together to form the structure depicted schematically in the figure 3.14 so that the left-right ambiguity disappears. The spatial resolution is in this way improved up to 100 μm.

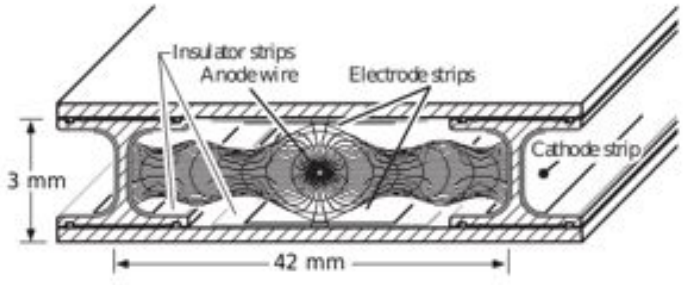

Figure 3.13: Schematic view of a DT [37]

3.5.3 Resistive Plate Chambers

Resistive Plate Chambers (RPC) are composed of a gas region enclosed by two plates of resistive material (bakelite). Behind those plates are placed readout electrodes. RPC function in a mode called the *streamer* mode where an intense electric potential of 7 kV to 12 kV is applied on the surface of the plates coated in graphite. A muon passing through a RPC creates a discharge inside the gas, however the electron-ion pairs never reach the electrodes due to the high resistive plates. The evacuation time of the detector can therefore be very long if too many charges are produced hence it is preferred to maintain a low gain. Most of the signal amplification is done by the readout electronics. The RPCs have a reduced spatial resolution of 1 mm but have an excellent time resolution of 1 ns and a rate capability of up to 10 $kHz\ cm^{-2}$.

3.5.4 CMS Detector Configuration

The disposition of the three different detectors presented above has been chosen to cover a maximum detection area. The different radiation environments also play a main role since they are different in the barrel $|\eta| < 1.2$ (10 Hz/cl^2) and endcap region $1 < |\eta| < 2.4$ (10 - 1000 Hz/cm^2) .See Figure 3.17 In the barrel region the radiation background is relatively small , the muon rates are not significant as well as the magnetic field residuals, DTs are preferred. In the endcaps, CSCs are used where high radiation, muon rates and magnetic field residuals are high .(See Figure 3.16) Moreover, RPCs are added in both regions to ensure good time resolution. Since the instantaneous luminosity at start-up was expected to be lower than the nominal one, for financial reasons, the installation of RPCs in the forward region $1.6 < |\eta| < 2.4$ was staged. Currently this region is still instrumented with CSCs only.

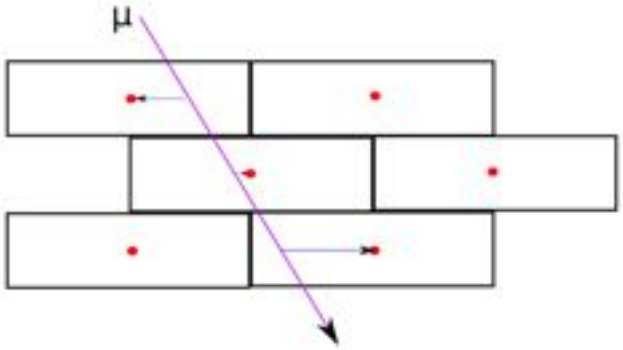

Figure 3.14: right-left ambiguity lifted when placing a translated second layer of DTs with parallel anodes

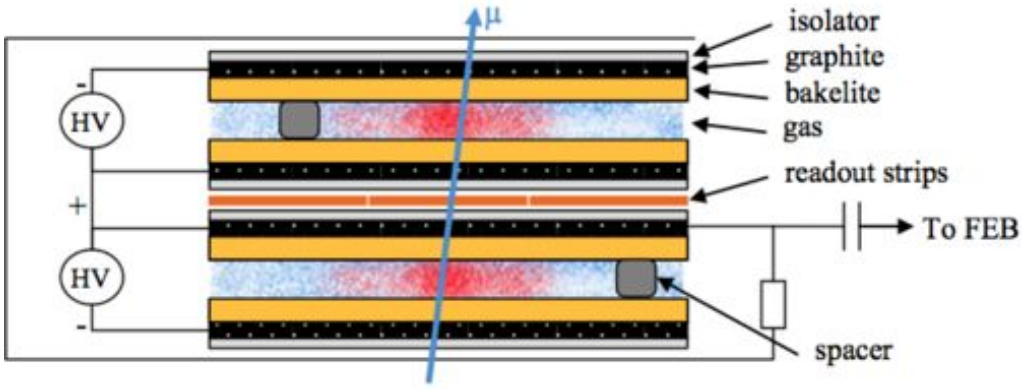

Figure 3.15: Schematic view of an RPC [37]

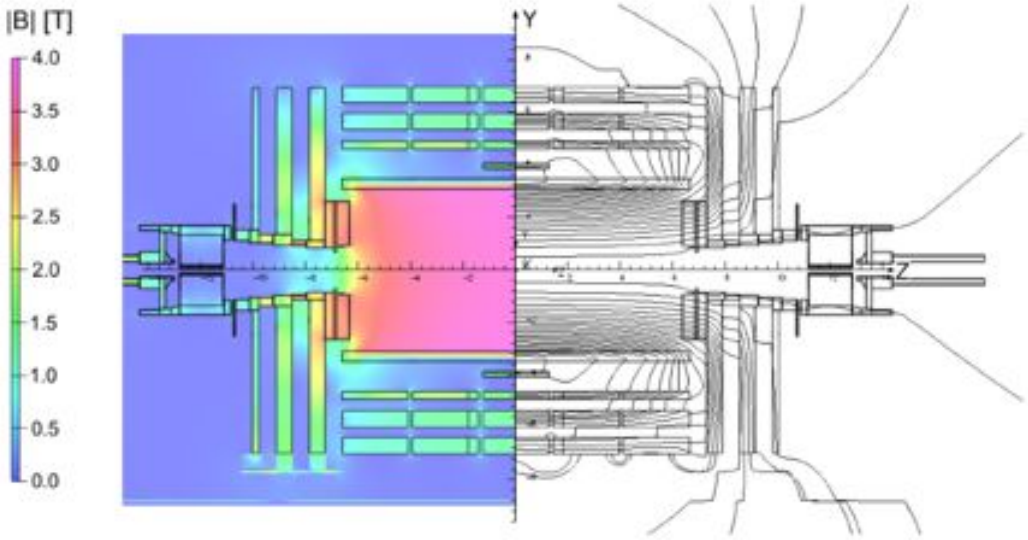

Figure 3.16: Longitudinal section view of the CMS map of the magnetic field (right) and lines (left) . The field strength varies between 0.5 T and 2.7 T in the endcap region of the muon spectrometer. [38]

3.5.5 Upgrade of the CMS muon spectrometer

[7] The forward region $1.6 < |\eta| < 2.4$ being only equipped with CSCs, leaves this part of the detector less robust and efficient for muon triggering and identification. One also wants to have a maximum detection efficiency and rate capability to enhance the physics reach. It is then interesting to place additional layers of detection in the forward area

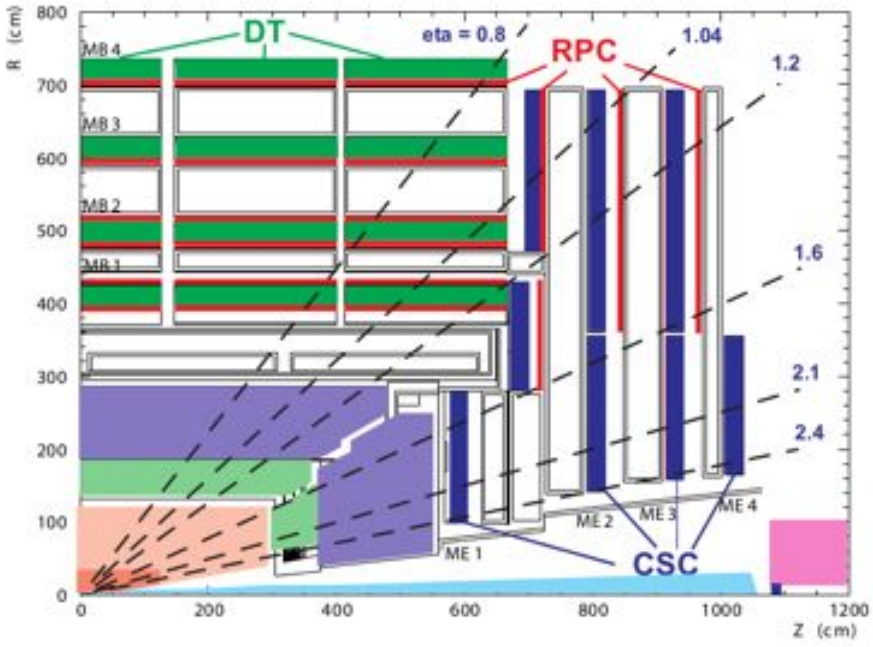

Figure 3.17: Disposition of the different detector inside the CMS muon spectrometer.[37]

to yield additional particle hits resulting in the improvement of the track reconstruction, the muon momentum resolution and better constraints on the background rejection at the trigger level.

The LHC will enter in the following years its High Luminosity Phase shortly after the LS2 (see Section 2.1.3), where one expects rates of several kHz cm^{-2} in the $|\eta| > 1.6$ region. The already installed RPCs in the $|\eta| < 1.6$ region will not be able to operate at this rate. This is why the CMS GEM Collaboration plans to install a new technology of gaseous detector in this region able to sustain such rates and maintain an good space and time resolution. The new detectors are called *Gaseous Electron Multiplier* (GEM) and will be described in detail in the next chapters.

Chapter 4

Gas Electron Multiplier Detector

This chapter will review the the geometry and the functioning of a GEM detector followed by the different modeling methods and softwares used to simulate the whole detector response from the first ionization and the avalanche process to the formation of the signal.

4.1 Detector Design

[39] A GEM detector is constituted by an enclosed volume separated by the *GEM foil*. The gap above the foil is called the *drift gap* while the gap below is the induction gap.

A GEM foil (see Figure 4.1) is composed of a 50 μm thick kapton foil between two copper plates of 5 μm thickness. Microscopic holes are drilled in this foil using a method called *etching* [2]. The hole diameter is typically 35 μm and 70 μm while the distance between the holes also called the *pitch* varies between 50 μm and 200 μm.

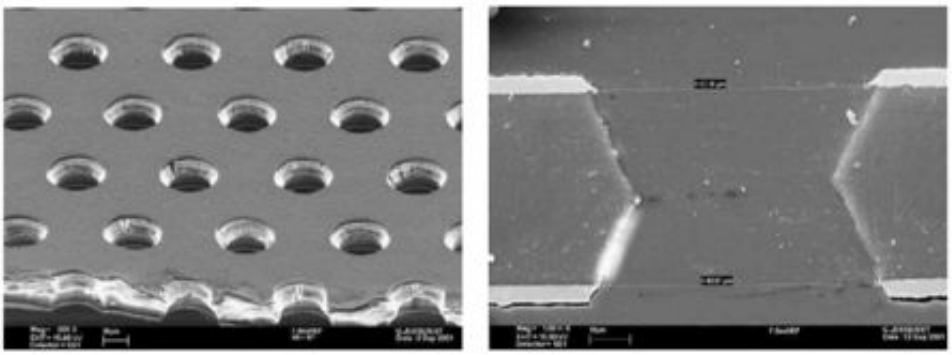

Figure 4.1: Left: Electron microscope view of a GEM holes, Right: Biconic section of a hole [40].

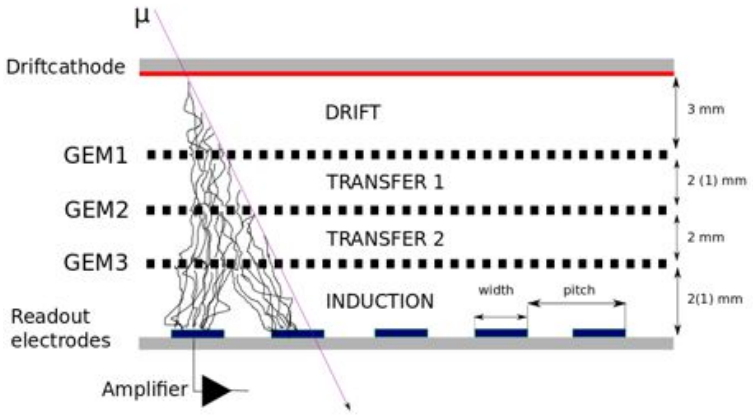

Figure 4.2: Electron avalanche forming inside a triple GEM detector.

4.2 Functioning

Let us focus first on the functioning of a single GEM foil detector which can be later on easily generalized to a detector with multiple GEM foils. A muon entering the GEM detector ionizes the gas producing the primary electrons in the drift region where an electric field of a few kV/cm is applied enabling the negative charges to drift towards the GEM foil while the ions are flowing in the opposite direction.

The electrons yet to few to produce a signal on the readout electronics placed at the end of the induction gap will have to be multiplied. This is where the GEM foil comes into play. Between the top and bottom layer of the copper plate a voltage of a few hundred Volts is applied producing a high electric field region, especially inside the hole where it can reach tenths of kV/cm^2.

Electrons passing through the holes get multiplied by a certain gain factor depending mainly on the electric field and the geometry inside the detector. In order to further increase this gain factor, more GEM foils can be added where the electrons go through a series of additional multiplication stages . A *Double GEM* (DGEM) and a *Triple GEM* have two and three foils respectively. In a multi GEM detector the intermediate gaps between the drift and induction gaps are called the *transfer gaps*. Electrons leaving the last GEM foil enter the induction gap where the signal is induced on the readout electrodes.

A detector made of multiple GEM foils allows to reach higher gains as seen in Figure 4.4 at lower voltages across the various foils, compared to a detector made of a single foil. Since multiple GEMs operate at lower voltages than a single GEM, the discharge

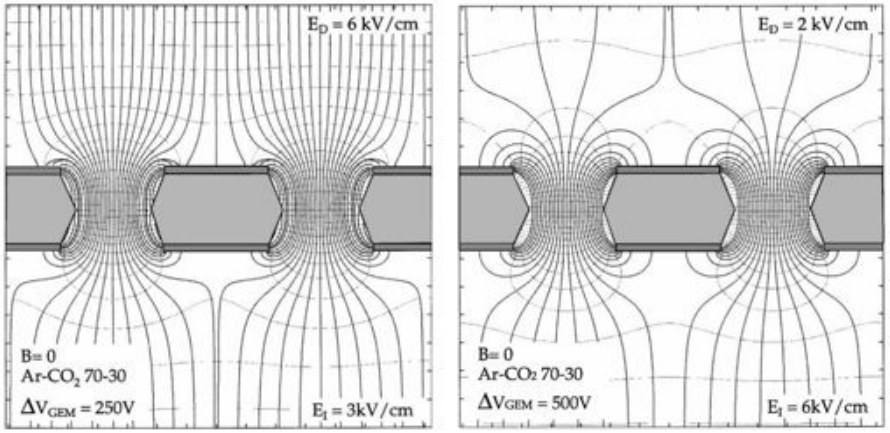

Figure 4.3: Field lines of a GEM. Left: Intense drift field (6 kV/cm) and low induction field (3 kV/cm) with voltage of 250 V across the GEM foil. Right: Low drift field (3 kV/cm) and intense induction field (6 kV/cm) with a voltage of 500 V across the GEM. Inside the holes, the electric field lines get really dense with a relatively low voltage source. [41]

probability is also very much suppressed.

After the last multiplication at the exit of the third GEM layer, the avalanched electrons also called the *electron clusters* enter the induction gap where a signal is induced on the readout strips placed at the lower part of this gap.

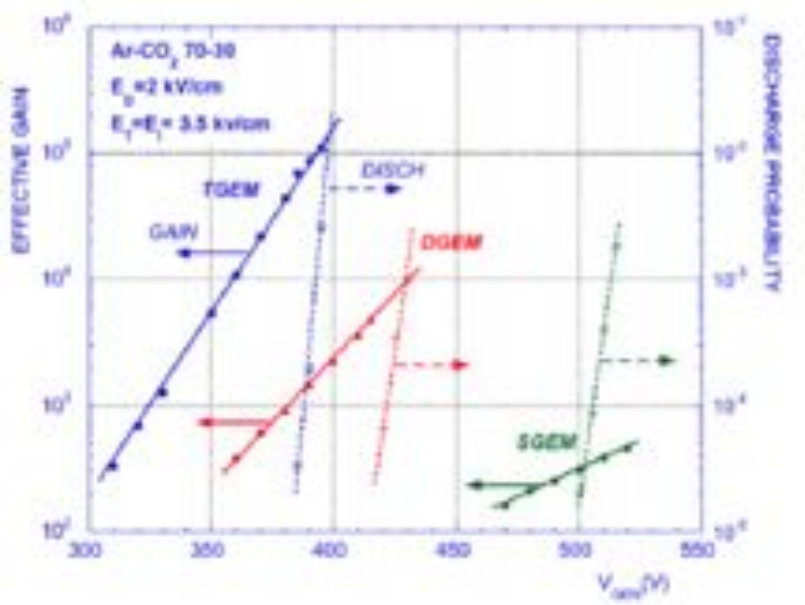

Figure 4.4: gain and discharge probability for different numbers of GEM layer as a function to the applied voltage. [42]

4.3 GEM for the CMS upgrade

[7] [43] As introduced in the previous chapter, the RPC detectors are not able to sustain the high rate particle flux in the forward region of the muon spectrometer for $1.6 < |\eta| < 2.4$. Instead the new GEM technology will be installed in the presently not instrumented parts of the CMS endcap muon system. Several test beam studies have successfully concluded that this type of detector will sustain the high radiation fluxes in the forward region for the era of the high-luminosity LHC, ranging up to several kHz cm^{-2}. Figure 4.5 shows the relative gain of a GEM detectors compared to *Multi Wire Proportional Chambers* (MWPC) which include DT's and CSC's. With increasingly high particle rates, the gain of the MWPC drops rapidly while GEM detectors maintaincon-stantly their relative gain even at higher particle rates up to 10^4 kHz/mm^2.

This new upgrade completes the trigger system of muons by adding a redundancy in the high η regions, unable to be filled by the RPCs. In this way a good transverse momentum resolution for high-p_T endcap muons in the TeV range can be achieved which is important for the muon trigger system. Additionally a second independent trigger path is provided in the forward region.

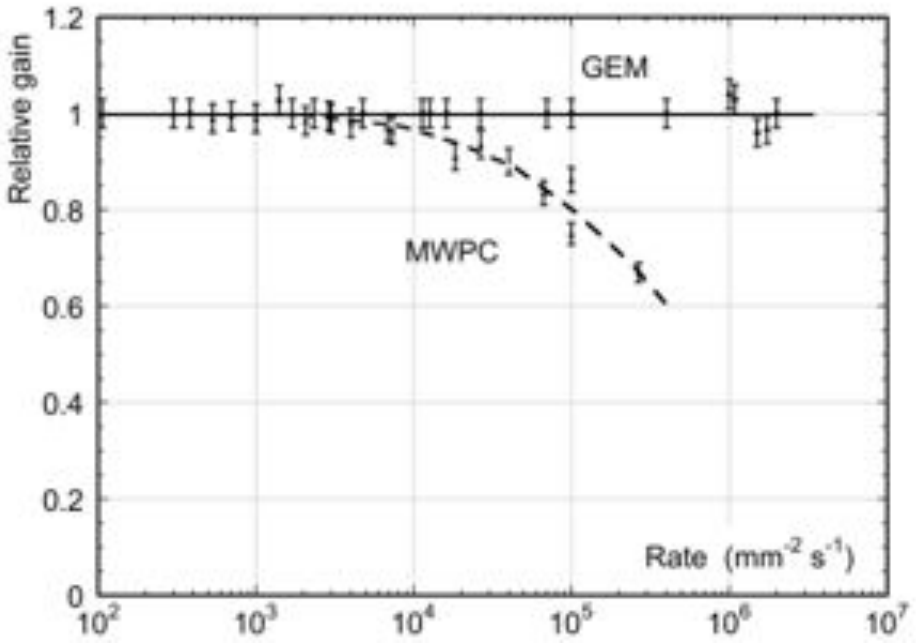

Figure 4.5: Realtive gain of the GEM technology compared to the MWPC as a function of the particle radiation flux. [20]

Figure 4.7 shows a longitudinal view of the CMS barrel and endcap region where the orange zones depict the future location of the GEM stations GE 1/1 and GE 2/1 each constituted by two back-to-back triple GEM detectors. For the GE 1/1 station, each detector covers an angle of 10° and has a trapezoidal shape of dimensions 990 mm (220 - 455)mm having a total detection surface of 3000 cm^2 shown on Figure 4.6. It is worth noting than since the particle flux rate in the Muon Chambers is 10 kHz implies that each Triple GEM detector with its 3000 cm^2 is submitted under a total radiation rate of $3 \cdot 10^8$ Hz. Since each Triple GEM is partitionned into 3x8 segments with each 128 readout channels, the average interval time of two particles hitting the one strip is around 100 ns. [1]

1. This time interval will impose a constraint on the duration of a signal recorded on the readout electronics, detailled in Chapter 7.

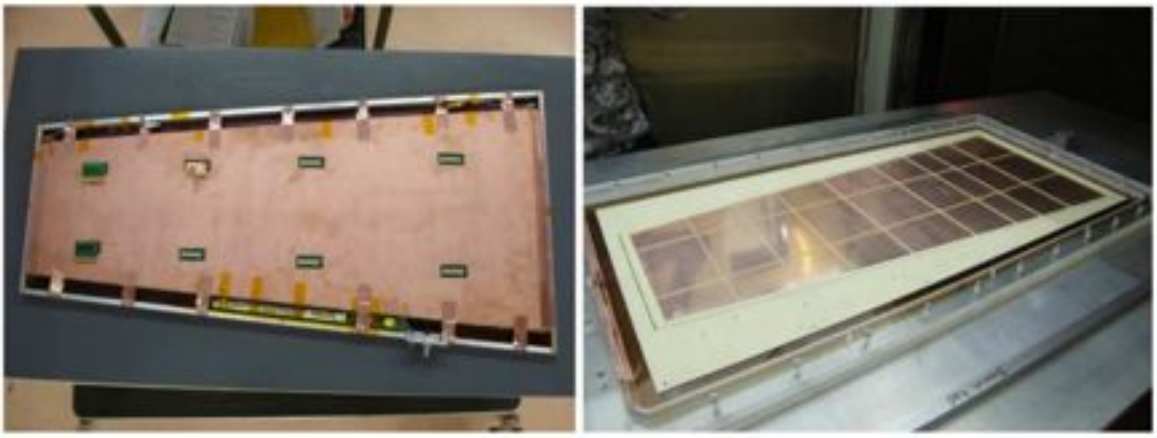

Figure 4.6: large Triple GEM prototype constituted by 3x8 segments [43]

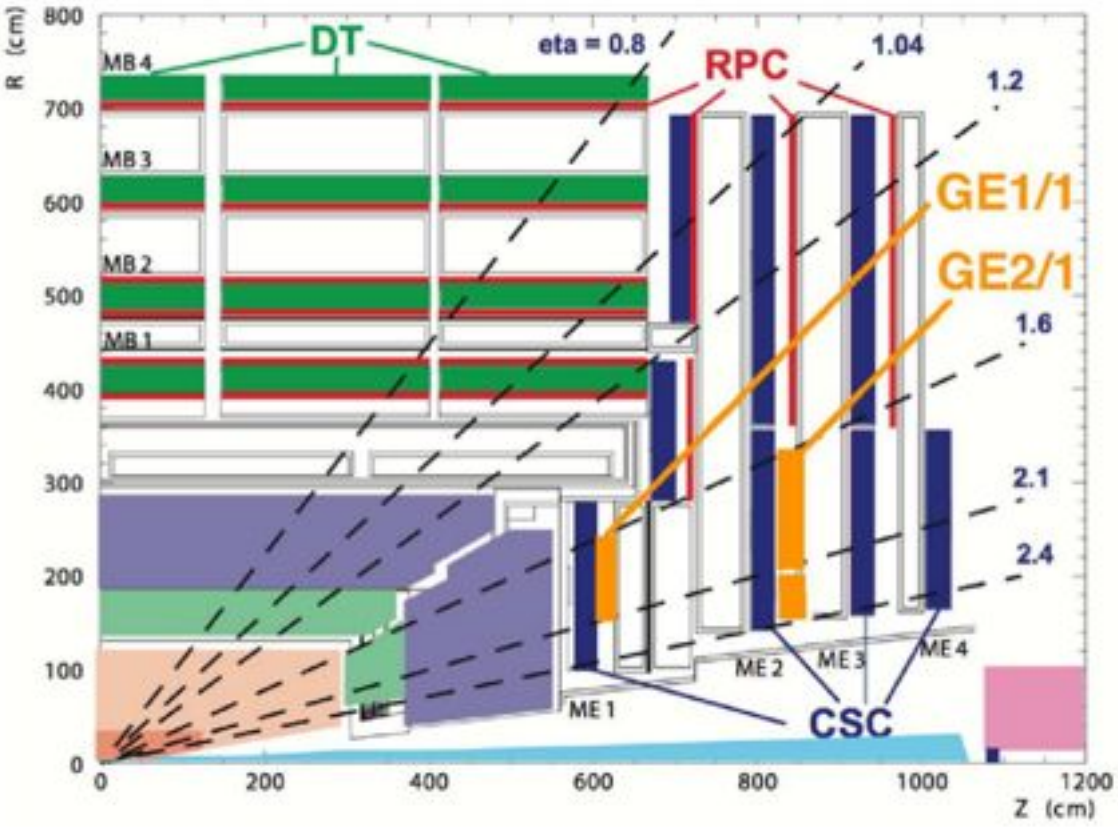

Figure 4.7: Longitudinal view of CMS of the barrel and endcap region. [43]

4.4 Simulation

Since the main scope of this work concentrates on the modeling of a GEM detector it will be important to introduce the reader to the different simulation tools used to obtain the different results presented in the following chapters. This chapter covers the functioning of several simulation softwares used to compute the field maps inside the detector, the generation of primary electrons inside the gas produced by the ionizing particle, the simulation of an electron avalanche and the signal formation on the readout electrodes.

4.4.1 ANSYS

[44] [45] [46] Ansys is a simulation software capable of modeling multiple phenomena ranging from thermal and electrical conduction to fluid dynamics. For our purpose we will use Ansys to create the electric field maps of our detector, in other words computing the electric potential in each point inside the detector taking into account the internal applied electric field and the geometry of the GEM. The software aims at solving the Maxwell equation of electrodynamics by using the method of finite elements. This method is a numerical integration of the partial differential equation able to retrieve a field map of the geometry present inside a GEM where any analytical methods would fail due to the complex boundary conditions. This method is analogous to the idea where the area of a disc is approximated by filling it with increasingly smaller rectangles, the mesh and where each infinitesimal area is given by the shaping function.

Field maps

First of all, the materials inside the GEM have to be defined in Ansys by attributing them a certain dielectric constant. The gas will have a constant near 1 since for instance CF_4 ,CO_2, Ar are transparent and have a refractive index equal to 1. The copper plates on the GEM foil are electric current conductors and have a very high dielectric constant around 10^{10}. Kapton being an insulator material has a dielectric constant of 4.

Secondly, a mesh is defined to cover the whole detector volume where we want to solve the equations. This mesh is partitioned in tetrahedra in order to adapt to the geometry of the inside surface we want to cover. At every node of the mesh the electric potential is computed. Depending on the complexity of the geometry, the size of the tetrahedra will decrease rapidly to cover efficiently irregular shapes especially near the GEM holes.

Since the number of polygons increases with complexity of the geometry hence the risk to generate imprecise shapes, we are bound to simplify the situation in order to avoid false field computation. To do this we have to recognize that the GEM geometry has a translational symmetry so that we can reduce the problem to one selected region also know in lattice theory, as the primitive cell. By limiting the field computation to this cell, we can solve the entire field map by arguments based on symmetry. Figure 4.8 shows the three possible types of cells able to generate the whole GEM structure. However the

Figure 4.8: Cells able to build up a single GEM, the first one being the primitive cell. [25]

second and third are generated by the first which can be considered as the primitive cell of the GEM lattice.To complete the simplification we have to add symmetrical boundary condition on the XY plane along the Z axis in order to generate the GEM holes and to satisfy symmetrical boundary conditions.

The generated mesh gives the solution of the problem at every node by knowing the shape of the given polygons. In our case we use curved tetrahedrals with 10 nodes. To each polygon is associated a given shaping function where by extrapolation the whole problem can be solved. The software returns the values of all the electric potentials enabling us to know the corresponding electric field lines.

4.4.2 GARFIELD

[47] [48] Garfield is multi-functional software using a C++ interface in ROOT called Garfroot developed for simulating the behavior of gaseous and silicon based detectors. Its application ranges from simulation of an electron avalanche to the ionization produced by a muon inside a medium and can model the signal formation on a readout strip. Field maps that were previously computed numerically or analytically are used as inputs to map exactly where the electric flux lines are the most dense hence where the electron avalanche will take place. Starting with several electrons in the drift gap created by the ionizing particle we will in this section explain how Garfield manages to simulate their drifting and multiplication .

The main feature of Garfield is its ability to compute collisions based on the method called *null collision*. To expose this let us state the problem in terms of probability. It is straightforward to assume that the collision probability $P(t)$ in a given time interval δt depends on the speed of the particle $\vec{V}(t)$ and of course of the relative speed of the gas atom or molecule$\vec{u}$. If the reference frame is the same as the laboratory we can state that:

$$P(t)\delta t = \alpha(t)e^{-\int_0^t \alpha(\tau)d\tau}\delta t \tag{4.1}$$

where $\alpha(t)$ is the collision rate defined by:

$$\alpha(t) = \int \sigma(\Delta v)f(\vec{u}d\vec{u} \tag{4.2}$$

where $\|\vec{V}(t) - \vec{u}\|$ and σ is the cross section of the collision depending on the relative speed between the two particles. f represents the speed distribution of the gas particles depending on its pressure and temperature. [49] The null collision method states that if $\alpha(t)$ is bounded we can introduce a certain noise coming from ineffective collisions in such a way that

$$\alpha_{max} = \alpha(t) + \alpha_{ineff} \tag{4.3}$$

α_{max} is an arbitrary constant bounding $\alpha(t)$ so that the combined probability distribution takes a simpler form

$$P_c(t) = \alpha_{max}e^{-\alpha maxt} \tag{4.4}$$

Knowing the results of this expression and at the same time the added noise , by injecting a random distribution we can test if a real collision has occurred or not. Once the test confirms the generated event, a random cross section is picked up from a data base depending on the type of process that is occurring which includes a ionizations, elastic and inelastic scattering, vibrational or translational excitation. Each of this reaction has a certain rate of occurrence depending on the energy of the reaction and produced different end states. For instance a elastic scattering collision will only diffuse the electrons in every direction, ionization will add electrons and lower the ionizing particle's energy. The Penning effect is not included in this library of reactions and is computed separately.

Ions created during the ionization are described by the Langevin equation where their mobilities in their respective medium are looked up in mobility tables. We will furthermore not be very interested in their description since; will show later that their presence doesn't contribute significantly to the signal formation.

4.4.3 Magboltz

[51] Magboltz is used to solve the Boltzmann transport equation used by Garfield to simulate the microscopic trajectory of the electrons traveling inside the gas. In this way it is possible to retrieve gas properties such as drift velocities, Townsend and diffusion coefficients. FOOTNOTE

4.4.4 Heed

[52] Heed is used to simulate primary ionizations, compute the energy loss of the ionizing particle and retrieve the resulting electron distributions taking into account the different possible cross sections for each atoms inside the medium. Next Chapter will

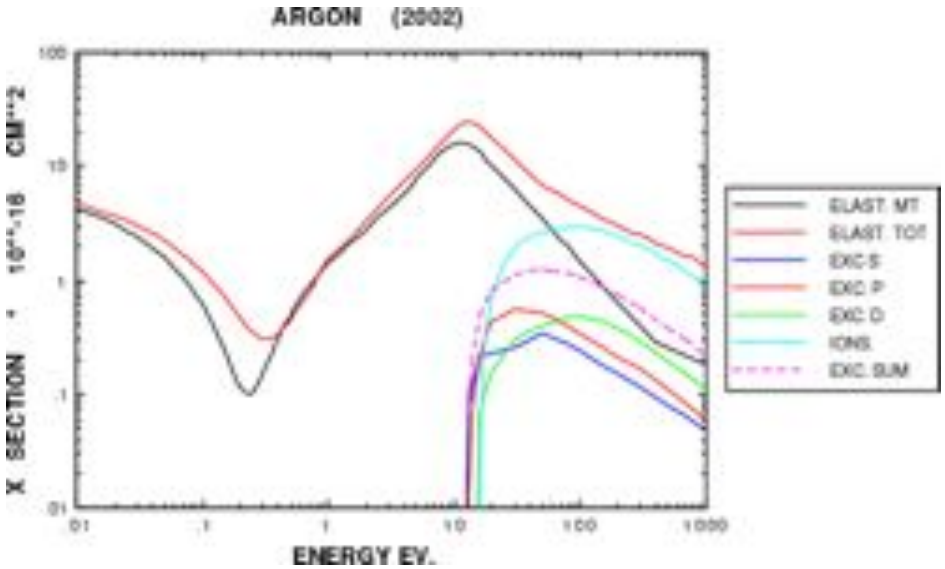

Figure 4.9: Cross section for different processes inside Ar [50]

expose the different primary electron distribution produced by muons and pions inside a gas volume.

4.4.5 Geometry

The GEM detector is planned to be installed in the endcaps of the CMS muon spectrometer. The detector should then face the interaction point between the two proton beams which justifies the choice of the coordinate axis shown in Figure . Figure 4.10 shows the geometry of the GEM foil with the values given in the following table.

D	70 μm
d	50 μm
Rim	80 μm
K	50 μm
P	140μm
d_{copper}	5 μm

The structure of the primitive cell for the single GEM can be generalized for a Triple GEM detector by piling up three single GEM primitive cells. However the central cell has to be inverted to correctly reproduce the tripleGEM primitive cell. Similarly, the same mirror conditions are imposed to model the whole structure containing all three GEM foils.

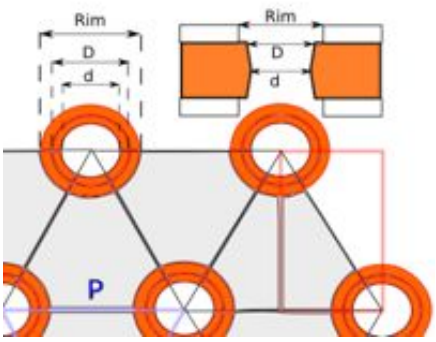

Figure 4.10: schematic view of a GEM foil with the biconic section of a GEM hole. kapton (orange), copper plates (white). D is the diameter of the hole, d the intern diameter, P is the pitch distance between two holes, K the thickness of the kapton and Rim the external diameter or distance between two cupper foils. The red rectangle depicts the primitive cell.

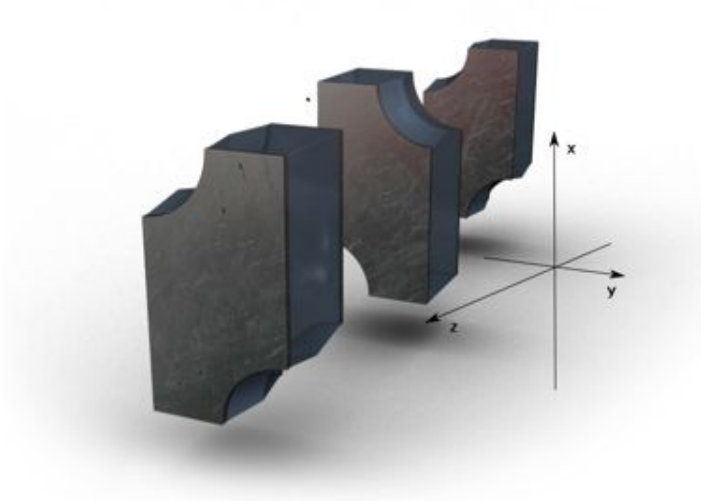

Figure 4.11: representation of the Triple GEM primitive cell [25]

Chapter 5

Simulation Results

This Chapter will describe the interaction of the primary particle inside the gas volume. This includes the energy loss of the ionizing particle we want to detect, and how many electrons are produced after each ionization. Moreover it will be of interest to derive some results of how the resulting electrons will drift inside the gas medium where a electric and a magnetic field is applied. All these results will be of great importance for the study of signals inside a Triple GEM detector. In fact the Garfield framework is able enough to model the signal induction in a Single GEM detector but fails at computing signals in a Triple GEM detector due to the complexity of the problem coupled with a limited computation power. This is why the following study has been made where the outcomes will be used as inputs for a hybrid simulation method explained in Chapter 7.

5.1 Primary Ionization

[37] The first step of modeling a gaseous detector starts with the ionization trace left by the primary particle. Along its trajectory it will collide with the gas atoms ejecting their orbital electrons. The process will continue until the ionizing particle has left the volume. The simulation will treat muons, charged pions and protons. Figure 5.1 shows the particle flux spectra entering the muon chambers from different sources as a function of η. Muons and pions are ideally expected to be created as products of the proton-proton collision as a result of jet production . Their energy spectra varies between 1 GeV to 1000 GeV and will contribute the most to the particle radiation. Since we are interested in the forward region of the detector close to the beam pipe a certain amount of radiation will enter the endcap muon chambers . Those background radiation are formed by charged particles like electrons, muons, pions and protons whose energy spectra are rather wide and have the potential to affect all chambers. In addition some leaking neutrons emitted from the very forward calorimeter (HF) originating from hadronization processes are able to enter the muon chambers. The flux grows exponentially near the beam pipe where it is mainly dominated by electrons/positons and muons. All these particles leave a specific type of interaction inside the gaseous detector, characterize . Let us first set some definitions to how characterize the different interaction occurring

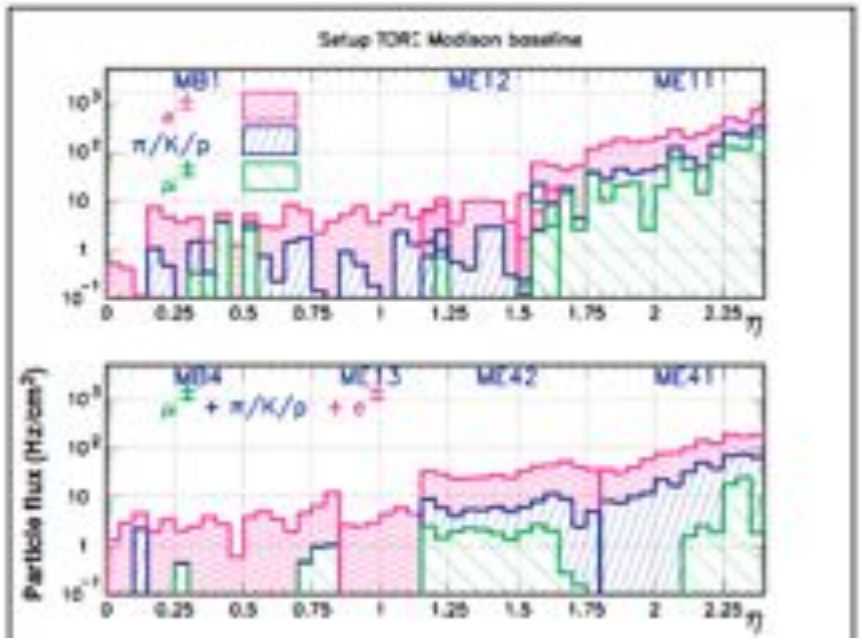

Figure 5.1: Charged particle fluxes in the muon chambers a cumulative sum of different sources. Top: fluxes in the first chamber as a function of η. Bottom: fluxes in the last chamber as a function of η [37]

inside the gas volume.

1. The number of primary clusters are the number of collisions between the primary particle and the gas molecule where a primary electron is produced.
2. The number of secondary clusters is the number of collisions between the primary electron and a gas molecule where another electron is produced often defined as the secondary electron.
3. The cluster size ot the total cluster is defined as the total amount of electrons including the primary and secondary electrons.

5.1.1 Primary clusters

To model the number of clusters produced inside a gas volume we will use Heed as a simulation software. Two different gaseous mixtures will be used $ArCO_2CF_4$ and $ArCO_2$ with respective proportions 45:15:40 and 70:30. The energy of the respective ionizing particles varies between 1 GeV - 1 TeV for muons, 1 GeV - 200 GeV for charged pions and 5 GeV - 200 GeV for protons. Neutrons will not be discussed here since they are not included in the Heed database and only interact with the detector by hadronization processes on the outer layers of the GEM outside the gas volume. The detector is modeled by a rectangular box 10 x 10 x 0.7 cm^3 in the (x, y, z) coordinate

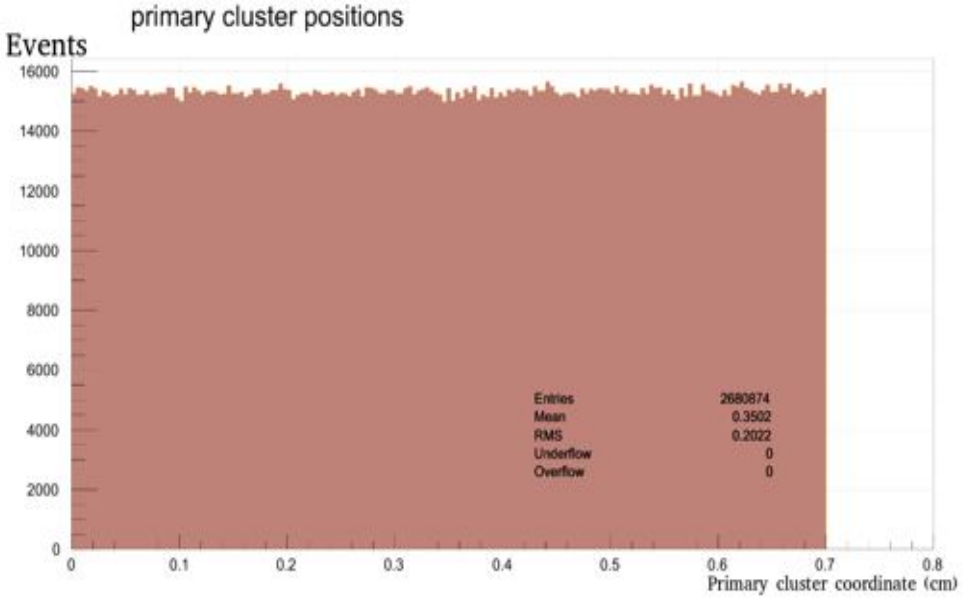

Figure 5.2: Position distribution of primary clusters along the track

.

system. [1] The incoming particle has an initial momentum vector (0,0,1) and will mainly ionize the gas along the 7 mm path. 100000 tracks have been computed.

Figure 5.2 shows the position of primary clusters produced by a 1 GeV muon inside $ArCO_2$ 70:30 . The ionization process is uniformly distributed and doesn't decrease during the flight. Figure 5.3 shows the energy lost of the muon inside $ArCO_2$ gas 70:30 which will be transfered to the ejected primary electrons. The behavior follows a Landau distribution.

It is possible to compute the number of primary clusters produced along the ionization track. This will be of importance when simulating the avalanche process of the secondary electrons. Figure 5.4 shows the number of clusters generated by five different particles at a given energy for the two gas mixtures. The distributions have a gaussian shape where we can suppose that the most probable value of primary clusters produced coincides with the mean value of the distribution. [2]

Let us extract for each particle, for different energies and for two different gas mixtures how the mean value of primary clusters behaves as a function of the primary particle's energy. This can be seen on Figure 5.5 where following observations can be drawn.

1. The number of primary clusters increases with the energy of the primary particle.
2. The number of primary clusters decreases with the primary particle's mass.

1. The total length of the drift distance inside a Triple GEM detector along the z axis is 7 mm including the 3 mm induction, 1 mm drift and two transfer gaps of 1 mm and 2 mm

2. The distribution has to be normalized with respect to the total amount of events simulated to be considered a probability distribution.

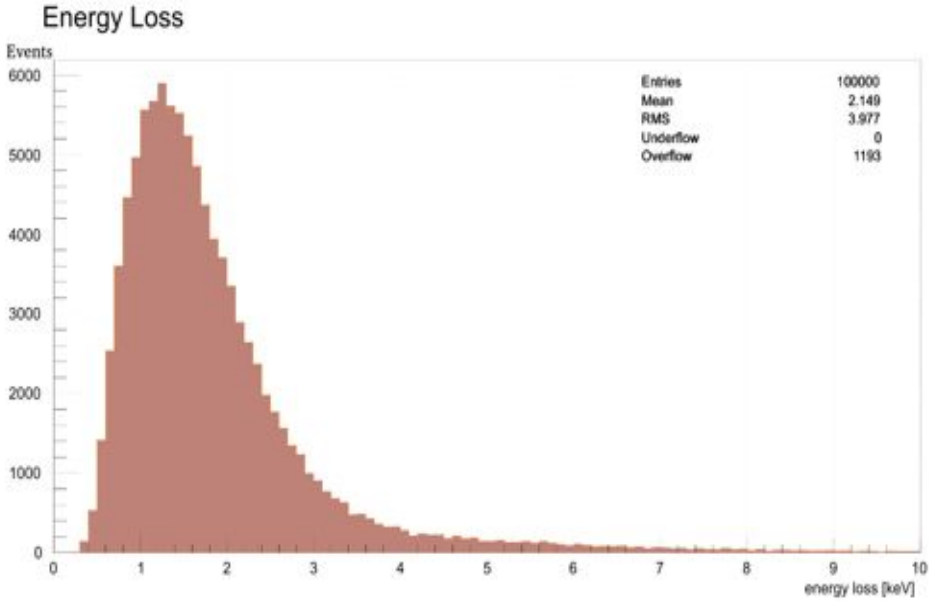

Figure 5.3: Energy loss of the ionizing particle deposited inside the gas.

3. The number of primary clusters produced by protons initially decreases but increases for energy values above 4 GeV
4. The number of primary clusters is more probable in $ArCO_2CF_4$ than in $ArCO_2$.

The fist observation can be compared to Figure 3.1 where the stopping power of a given medium increases with the primary particle's energy hence more energy is lost inside the material. The only way to transfer this energy to the atoms in the given medium is either elastically where no electron is ejected or inelastically where an ionization occurs.

The second observation can also be restated by saying that the interaction probability of heavy particles (protons) is smaller than for light particles (muons and pions) as long as they have the same absolute charge. This can only be verified in experiment , an exact explanation would consider to model the cross section for this interaction.

The third statement can be understood when noticing that a proton at 4 GeV has reached its minimum ionization point visible on Figure 3.2. $ArCO_2$ or $ArCO_2CF_4$ are gases similar to He gas where the MIP of the proton lies around a momentum of 3 GeV. [3]

3. $E^2 = p^2 + m^2$ hence for $p = 3\ GeV$ and $m = 938\ GeV$, $E \sim 3\ GeV$

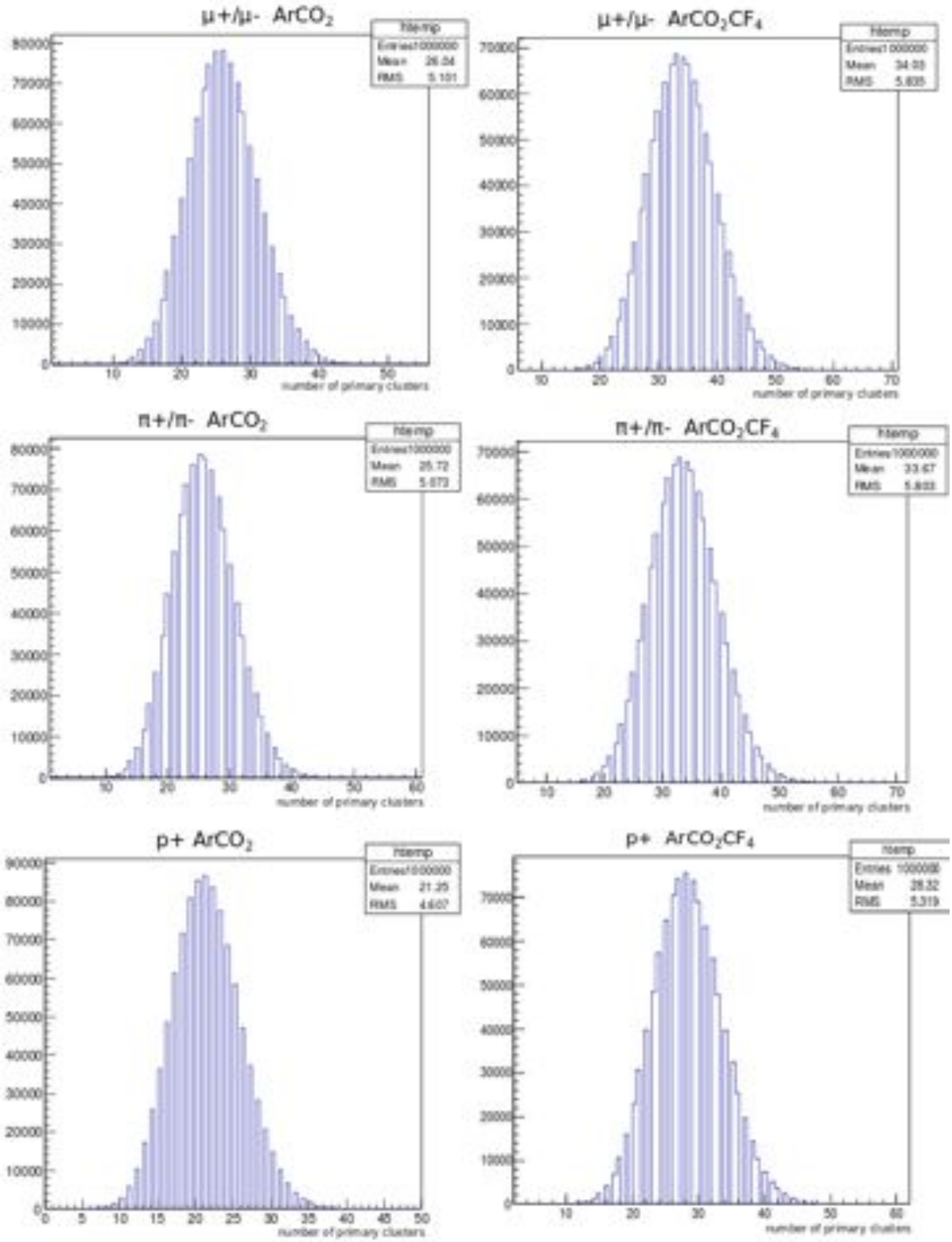

Figure 5.4: number of clusters produced by five different particles in 2 different gas mixtures

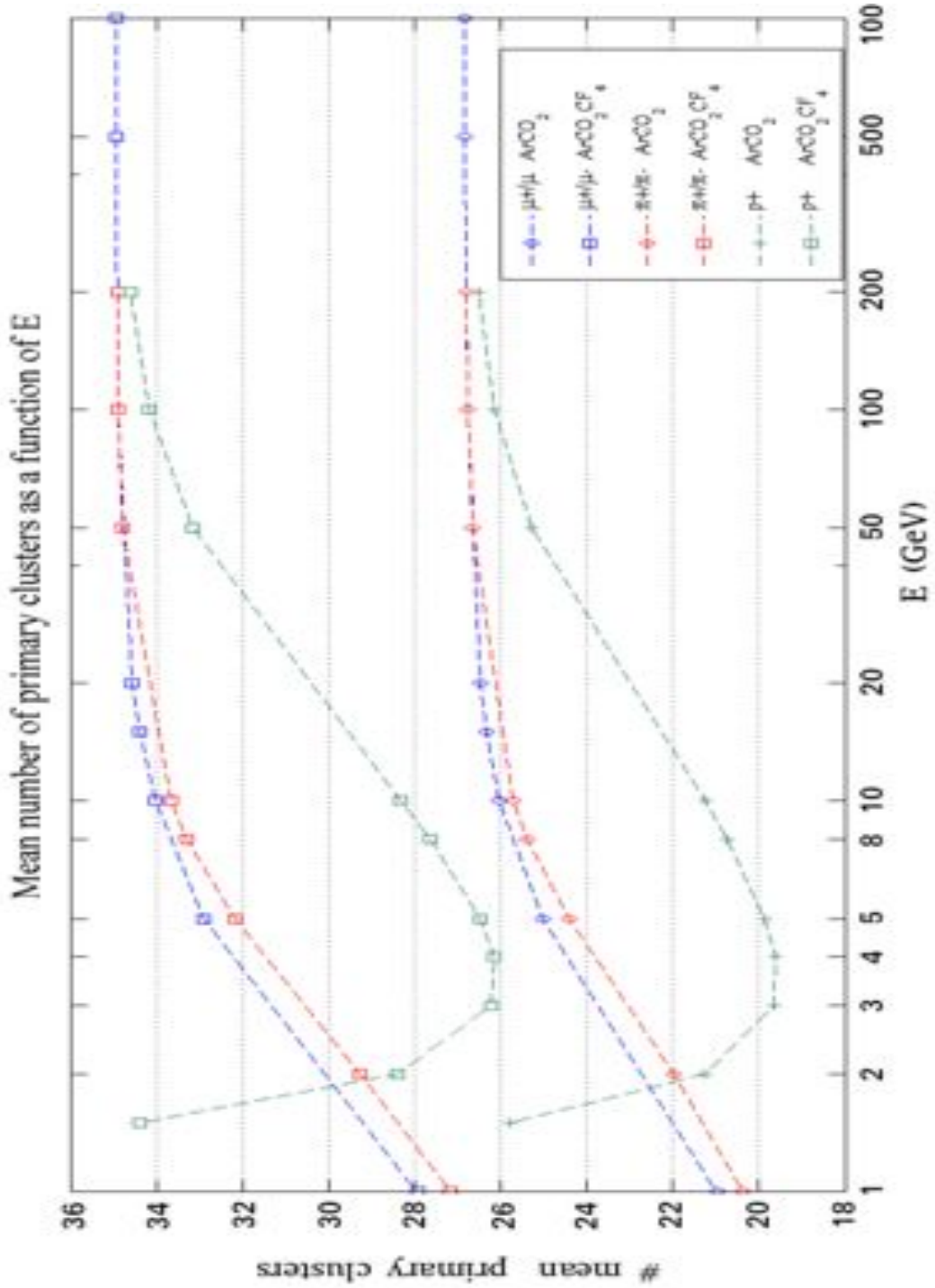

Figure 5.5: Mean number of primary cluster produced by three different primary particles for two different gas mixtures along a track of 1 *cm*. The results are shown as a function of the primary particle's energy. The dashed lines have been added. Vertical error bars are not shown and vary between 4-6 number of particle clusters. See Appendix A.

5.1.2 Mean energy loss

The mean energy loss is modeled using Heed where primary particles' trajectories inside the gas volume are generated over a distance of 1 cm. For each particle at a given energy losing its energy in a pure gas, a Landau distribution is drawn (See Figure 5.3) where the mean energy loss is extracted and plotted on a graph as a function of the primary particle's momentum. The results are shown on Figure 5.6 for three particles for three different pure gases. Additionally the obtained simulated results are compared with the mean energy loss curve shown on Figure 3.2 for muons, pions and protons inside gaseous Helium which has been obtained with the Bethe relation 3.1 in Section 3.2.1.

Note that the mean energy loss $\left\langle \frac{dE}{dx} \right\rangle$ shown on Figure 3.2 is expressed as the mean energy loss E in MeV per ρ per l where ρ is the density of the gas in $\frac{g}{cm^3}$ and l the distance in cm over which the primary particle loses its energy. Consequently we have to multiply the values for $\left\langle \frac{dE}{dx} \right\rangle$ by the helium density $\rho_{He} = 1.8 \cdot 10^{-4} g\ cm^{-3}$ in order to be compared to the simulated results. Following points can be drawn.

1. Energy losses are more important in gas mixtures containing $CF4$ than in other mixtures containing CO_2 and Ar.
2. Energy loss increases with the primary particle's mass and energy.
3. The simulated data (colored points) mimics the data coming from Figure 3.2 (green squares). Moreover the minimum ionization point is visible for the three particles and coincides with the MIP for the Figure 3.2 data.

We will not discuss the reasons for the first two points and will only be takes as observation since their explanation would not give us a better understanding of a GEM detecor. The third point is important since it confirm the validity of our simulation despite some deviations. Argon being a rare gas has a very close energy loss profile as Helium whcih is also a rare gas.

5.1.3 Cluster size

For determining the total secondary cluster size we have to take into account the secondary ionization where collisions between the primary electrons, having enough energy to ionize furthermore the gas are involved. Figure 5.8 shows the number of total secondary electrons produced per primary cluster. Alternatively we have chosen pure gases instead of mixtures. For gas mixtures $ArCO_2$ 70:30 and $ArCO_2CF_4$ 45:15:40 equation 5.1 applies where $\langle N \rangle$ each pure gas is averaged according to the mixture proportions so that the cluster size for each mixture can be computed.

The obtained distributions show that the probability of producing an increasing number of secondary electrons decreases exponentially. The most probable number of electrons produced is around 2 for the three gas mixtures.

It is instructive to know how mean value for this distribution behave as a function of energy for muons, pions and protons. We get the following table:

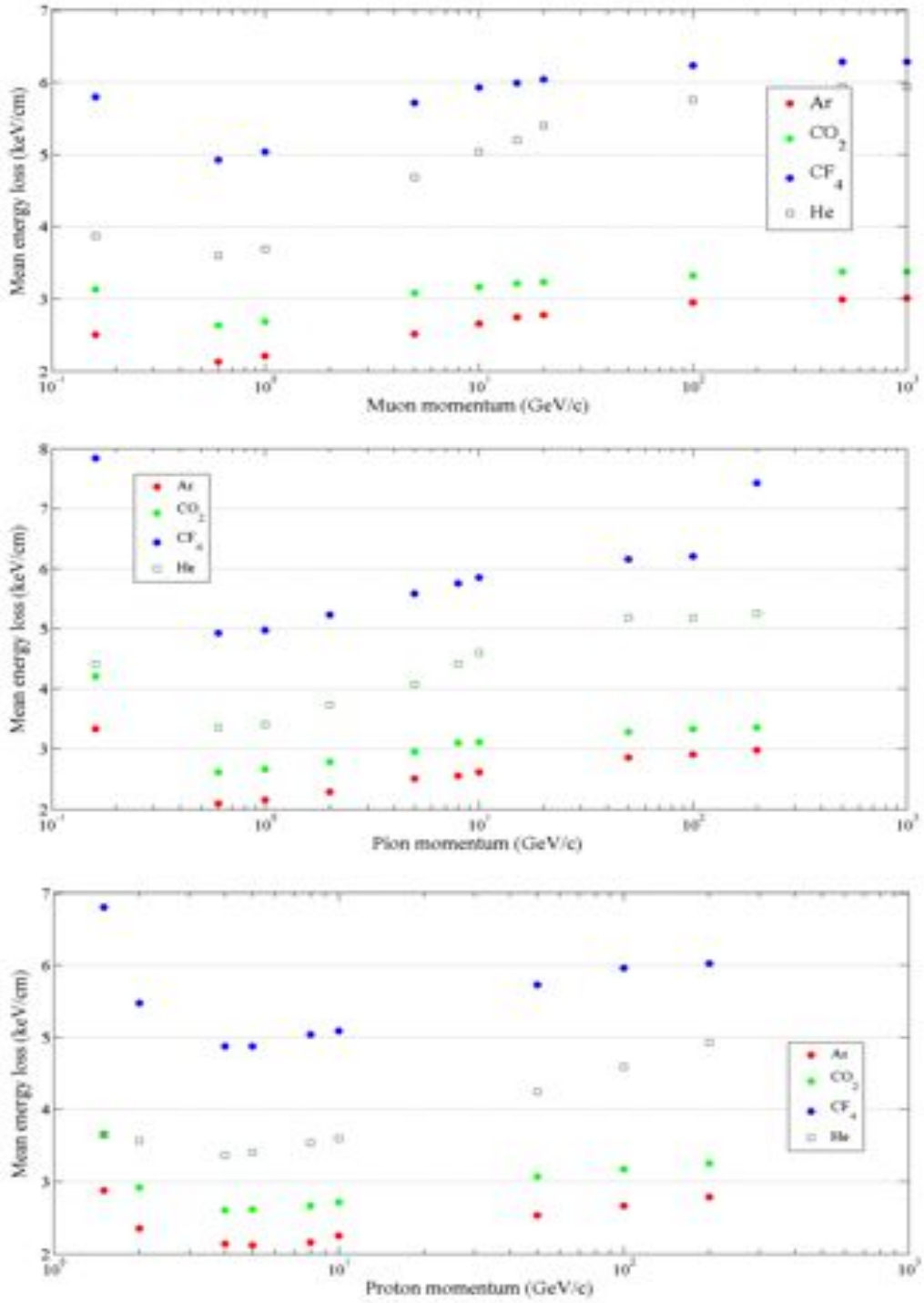

Figure 5.6: Mean energy loss simulated inside 1 cm gas volume shown for muon, pions and protons for three different gases, Ar (red) , CO_2 (green) and CF_4 (blue). The mean energy loss is also shown inside He (green squares) drawn from Figure 3.2

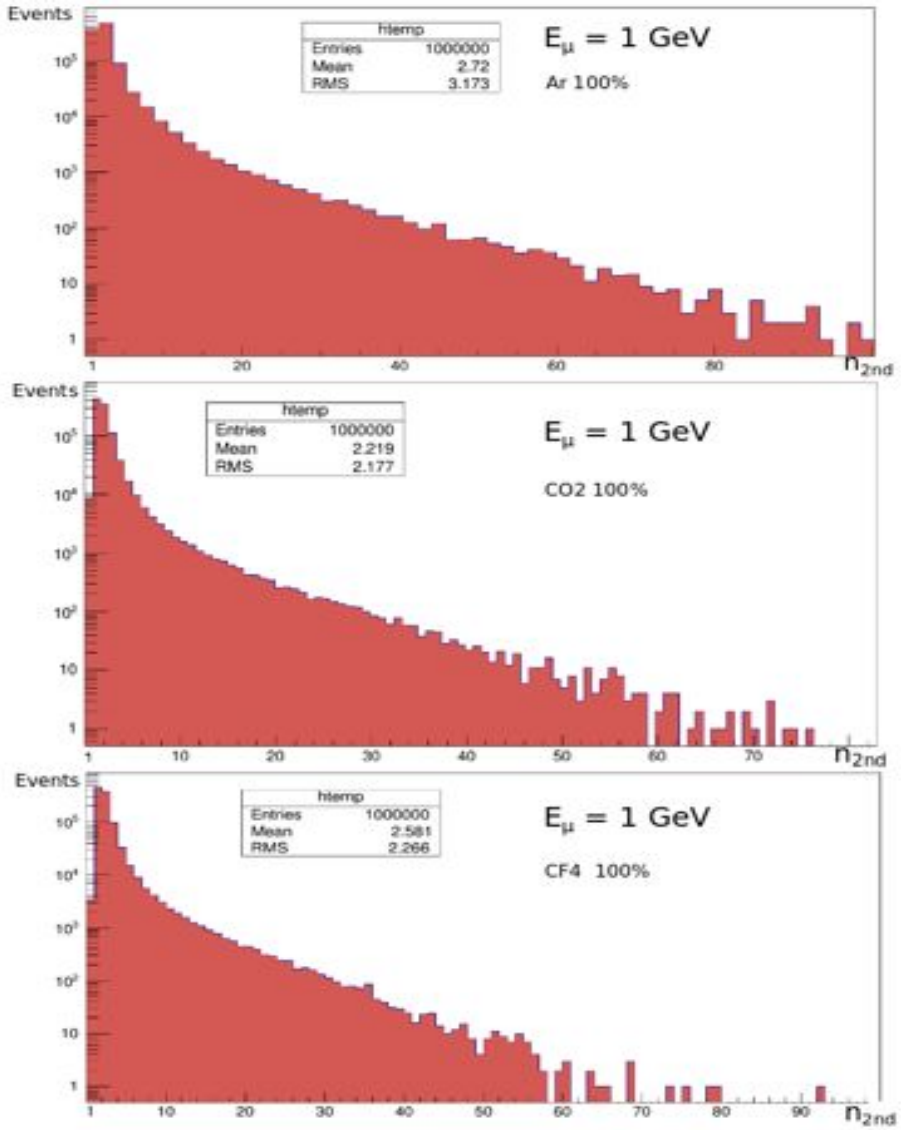

Figure 5.7: Total secondary electron distributions for muons at 1 GeV produced by one ionization collision in 3 different gases

First of all we recognize the same behavior as for the mean number of primary clusters, where lighter particles e.g. muons and pions ionize more easily than heavier particles like protons. Furthermore the minimum ionization particle bump is also observed this time for protons near 2 GeV. Finally notice that the presence of Argon along with the CF_4 inside a gas mixture produces the most electrons following the ionization process.

μ+/μ−

E (GeV)	Ar	CO_2	CF_4
1	2.7	2.2	2.6
5	2.8	2.3	2.7
10	2.8	2.3	2.7
15	2.9	2.3	2.7
20	2.9	2.3	2.7
100	2.9	2.3	2.7
500	3.1	2.4	2.7
1000	3.2	2.4	2.7

π+/π−

E (GeV)	Ar	CO_2	CF_4
1	2.7	2.1	2.6
2	2.8	2.2	2.6
5	2.9	2.3	2.7
8	2.9	2.3	2.7
10	2.9	2.3	2.7
50	3.1	2.4	2.8
100	3.1	2.4	2.8
200	3.2	2.4	2.8

p+

E (GeV)	Ar	CO_2	CF_4
1.5	3.1	2.5	2.9
2	2.8	2.3	2.8
3	2.7	2.2	2.6
4	2.7	2.2	2.7
5	2.7	2.3	2.7
8	2.8	2.3	2.7
10	2.8	2.3	2.9
50	3.1	2.5	2.9
100	3.1	2.5	2.9

Figure 5.8: Average number of total secondary electrons produced per primary collision as a function the energy in 3 different pure gases

5.2 Gas tables

A necessary step for successfully simulating an electron avalanches is the computation of electron drift velocities along with the diffusion coefficient inside a medium where a electric field is applied. The medium consists of two different gas mixtures ; $ArCO_2$ 70:30 or ArO_2CF_4 45:15:40. The Garfield interface called Magboltz will be used to compute these parameters by solving the Boltzmann transfer equations. The results are show in Figure 5.9. and are simulated with a collision parameter of 50 giving errors less than 1 %.

5.2.1 Drift velocity

The top plot on Figure 5.9 shows the drift velocity as a function E/p where E is the electric field applied along the z axis inside the medium and p the pressure of the gas. p has been fixed to the atmospheric pressure of 780 $Torr$.

1. The drift velocity inside the $ArCO_2CF_4$ mixture always exceeds the velocity inside the $ArCO_2$ mixture. This can be understood intuitively by comparing the density for each gas. Indeed we already showed in 3.33 that the drift velocity v_D is proportional to the mean free path λ which in turn is proportional to the density $\frac{1}{n_V}$. A simple calculation shows that the first gas mixture has less collision centers than the second which explains the ability of electrons to travel faster inside a less dense gas volume. This will also have an impact on the duration of the signal on the readout electronics.
2. It is useful to compare the drift velocity for both $B = 0$ and $B = 2.5T$ since there is a non negligible magnetic field in the endcap region of the muon chambers that varies between 0.1 T and 2.5 T. An angle of 8° between the electric and magnetic field has been chosen as it will be the case for the GE1/1 location. [38] In this

case the v_D is obtained by taking into account the transverse direction of the speed vector which are added to longitudinal components. However there seems to be no significant deviation from the $B = 0T$ case.

5.2.2 Longitudinal diffusion coefficient

The evolution of the longitudinal diffusion coefficient d_l is shown on Figure 5.9 (middle) dl measures the spread of the electrons in the direction z. Here again the presence of the magnetic field does not bring any deviation compared to the curve dl ($B = 0$).

5.2.3 Transverse diffusion coefficient

The transverse diffusion coefficient describes how the electron cluster spreads in the transverse plane (y,z) seen on Figure 5.9 (bottom)

1. The transverse diffusion is higher in the $ArCO_2$ mixture. This gas is denser hence the electrons tend to spread more easily due the increased collision centers encountered along their trajectories.
2. However in this case, the magnetic field has an influence on the transversal spreading. In fact it reduced the diffusion in the transverse plane as it has been discussed in Section 3.2. The electron cloud width is reduced by up to 10 % by a focusing effect.

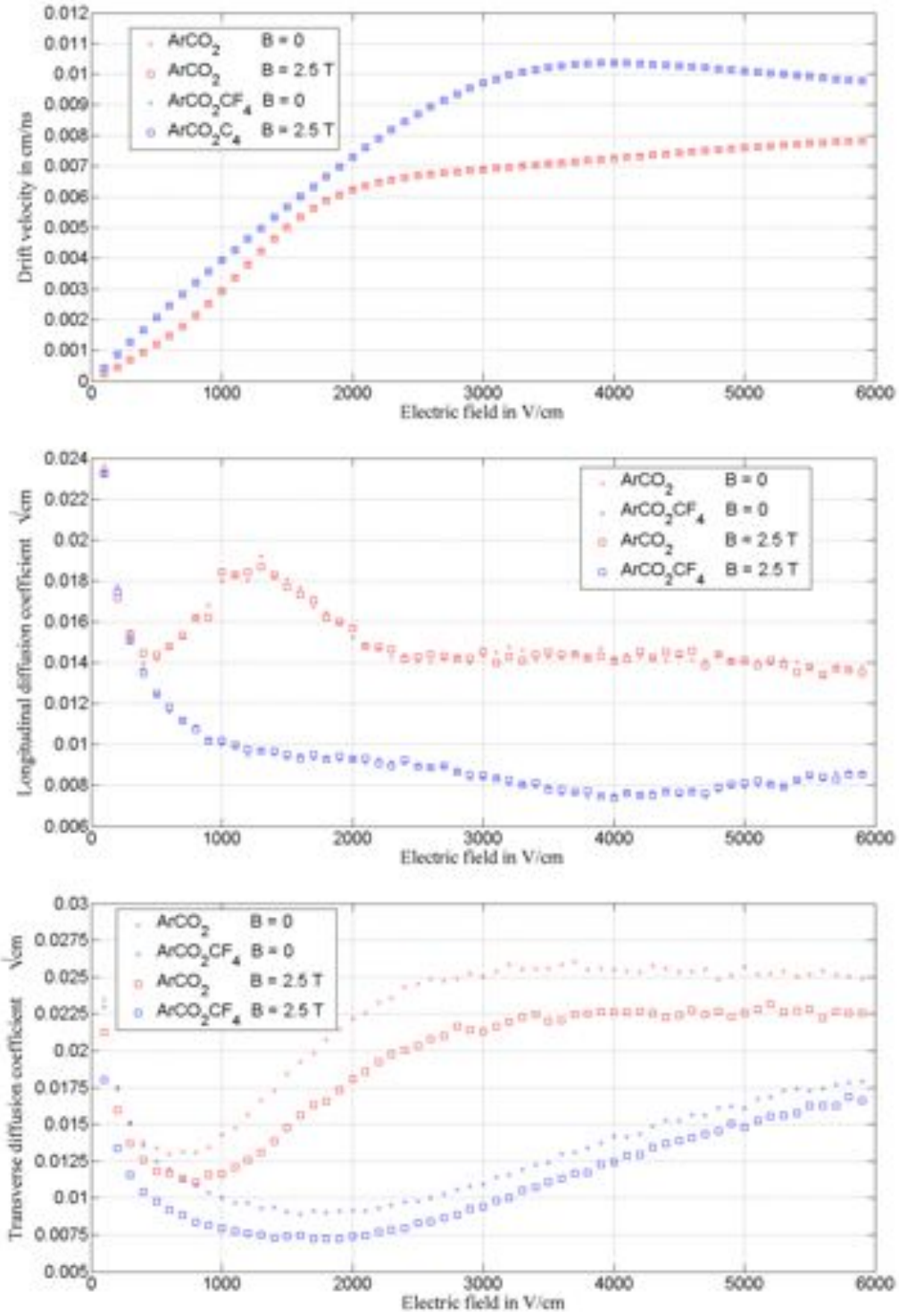

Figure 5.9: Drift velocity (top) , longitudinal diffusion coefficient (middle) and transverse diffusion coefficient (bottom) as a function of the electric field for two different gases. Squares show the data where a magnetic field of 2.5 T is applied with 8° with respect to the electric field.

5.3 Conclusions

The obtained results should give us some preliminary ideas how the primary particles interact with the gas. Moreover we have shown how the total cluster of electrons will drift and spread inside the gas when an electric and a magnetic field is applied. Those results will be used later for the parametrized simulation of thei CMS Triple GEM detector. Moreover the obtained parameters helped us study the difference between two gas mixtures $ArCO_2$ and $ArCO_2CF_4$ which will have a direct impact on the performance of the detector.

Some conclusions can be drawn at this point. An important result is the confirmation of the simulated mean energy loss profile with the data obtained by the Bethe equation. Moreover the number of primary cluster produced by the primary particle along with the cluster size which are coupled to the mean energy loss through equation 3.4 mimic as expected the behavior of the Bethe equation. This preliminary results give us an understanding of how many electrons can be generated by different primary particles.

Secondly we have show that the drift velocity is greater in $ArCO_2CF_4$ than in $ArCO_2$. This enables us to give an fist estimation of how the drift time of the electrons produced inside the gas volume varies depending on the gas mixture chosen. Indeed this will impact the performance of the Triple GEM detector which will be discussed in the following Chapters.

Thirdly the computation of the diffusion coefficient also gives us a first criterion of which gas mixture to choose. Note the difference in the transverse diffusion coefficient. where the electron cloud will spread more in $ArCO_2$ than in $ArCO_2CF_4$. This will strongly influence the spread of the electron cloud during its drifting inside the detector.

Lastly we discussed the presence of the magnetic field which had only an effect on the transverse diffusion coefficient by decreasing it as already expected in Section 3.2.6.

Chapter 6

Single GEM Study

Since now we have extracted all the necessary parameters for characterizing the interaction between the primary particle and the gas atoms along with the drift and diffusion properties of the primary/secondary electrons inside the gas volume. The aim of this Chapter is to model the avalanche where important parameters are extracted to describe the electron multiplication inside the gas and their transfer through the GEM holes. Moreover the outcomes of this study will be of importance for the hybrid simulation when discussing signals in a Triple GEM detector. Since the latter can be viewed as a generalization of a single GEM where each foil can be regarded as independent from the others, we are going to start with the study of a single GEM foil.

In order to do this we are going to simulate an avalanche starting with 1000 primary electrons (see Figure 6.1). To get various results, the voltage accros the GEM along with the electric field in the drift and induction gap are chosen differently for each avalanche. The process will be analyzed in two different gas mixtures $ArCO_2$ 70:30 and $ArCO_2CF_4$ 45:15:40.

The last part of this Chapter concerns the signal formation on the readout electronics.

6.1 Single Electron Response

First of all we are going to study the response of the detector when injecting a fixed number of primary electrons at 1 mm from the center of the GEM foil where they are going to be accelerated by the electric field in the drift region towards the GEM hole. This is where the multiplication starts. This process can be characterized by two different quantities; the gain and the transparency.

6.1.1 Total gain

The total gain of the detector is defined as the multiplication factor which describes the intensity of the electron avalanche. It is defined as the ratio between the the initial secondary electrons and the resulting multiplied electrons.

$$G_{tot} = \frac{n_{tot}}{n} \tag{6.1}$$

where n_{tot} is the number of electrons produced after the avalanche and n the number of primary electrons. However the total gain is not a very realistic measurable quantity since it doesn't take into account the attachment of electrons on material inside the GEM for instance the kapton foil.

6.1.2 Transparency and effective gain

In order to properly describe the avalanche process we have to count how many final electrons are able to contribute to the electronic signal in other words discard those who get attached by the kapton foil or the copper plates. An interesting quantity used in optics is the transparency which is defined in terms of the geometry of the gem foil, the pitch and the hole diameter. This definition is however independent of the voltages applied across the GEM, consequently we will use a more experimental approach. In this way the transparency can be defined as

$$T = \frac{n_{eff}}{n} \tag{6.2}$$

where n_{eff} is the number of electrons able to induce a signal on the electrodes per secondary electron. We consider electrons having passed 470 μm after the lower GEM foil as potential charge carriers producing a detectable signal or reaching the next GEM foil when considering a Triple GEM. This will lead us to define the *effective gain* which is the total gain corrected by the transparency.

$$G_{eff} = T \cdot G_{tot} \tag{6.3}$$

This is a quantity that will be measured later experimentally in this work.

Figure 6.2 shows the effective gain as a function of the GEM voltage for fixed drift and induction electric fields. The three different field values are frequently encountered for the three GEM foils in a Triple GEM. Low electric field in the drift gap (3 kV/cm) and intense field values in the induction gap 5 (kV/cm) maximize the transparency hence the effective gain of the detector. This is can be understood when visualizing the electric field lines on Figure 4.3. For intense drift fields, the field lines along which the electrons tend to travel are directed towards the upper metal plates where the charges get absorbed. For low drift fields this effect diminishes and more electrons are passing through the GEM hole. The opposite is true for the induction field where for higher values the extraction of the electrons out of the holes is more efficient This has been shown in Garfield transparency simulations [25]. Following observations can be made.

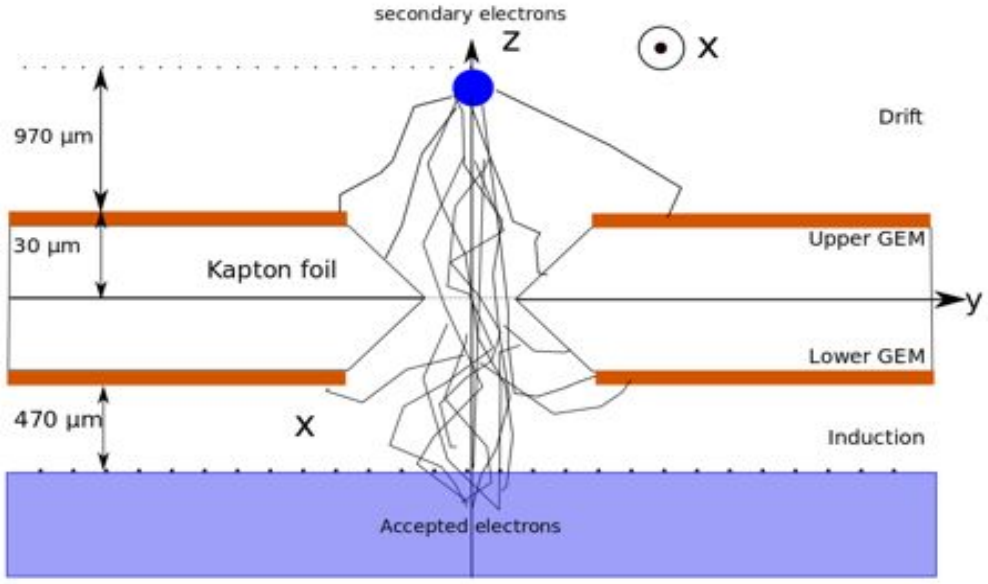

Figure 6.1: Schematic representation of an electron avalanche. Some electrons are absorbed by the copper plates (orange) or the kapton foil, others reach the blue region 470 μm below the lower GEM that will contribute to the signal formation.

1. The effective gain increases exponantially with the voltage across the GEM foil.
2. The avalanche process coupled with the transparency is more effective in $ArCO_2$ 70:30 compared to $ArCO_2CF_4$ 45:15:40.

The first observation can be understood easily knowing that the avalanche is a multiplicative process. The second is due to the higher Argon proportion in $ArCO_2$ which has a larger Townsend coefficient than CF_4. Moreover to each gas an attachement coefficient can be associated which is larger for CF_4 mixtures hence less transparency. This can be visualized on Figure 3.3.

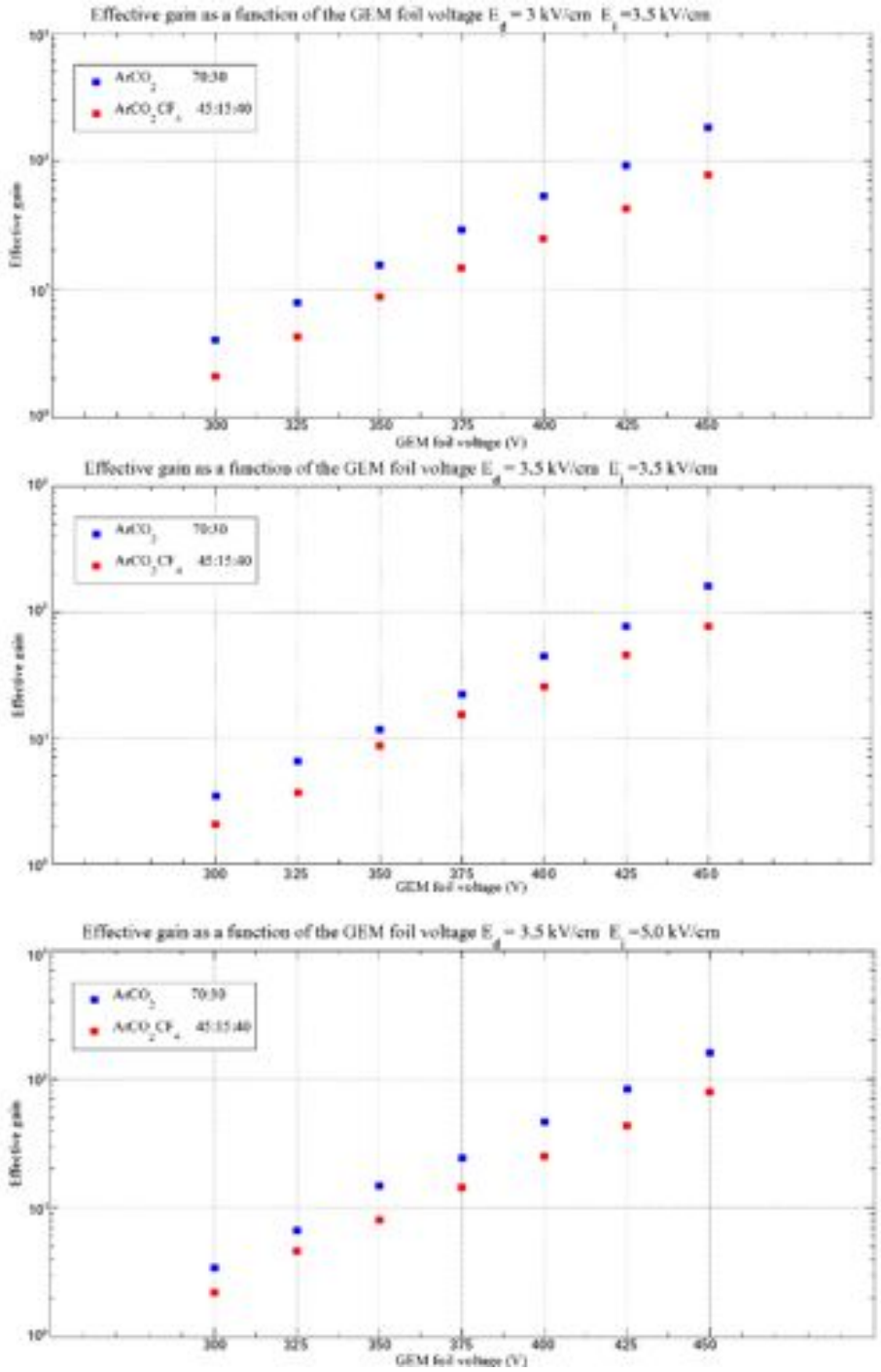

Figure 6.2: Effective gain as a function of the GEM foil voltage for three different drift and induction configurations. E_d is the drift electric field and E_i the induction electric field. Top $E_d = 3\ kV/cm\ E_i = 3.5\ kV/cm$. Middle: $E_d = 3.5\ kV/cm\ E_i = 3.5\ kV/cm$. Bottom : $E_d = 3.5\ kV/cm\ E_i = 5\ kV/cm$

6.2 Signal Formation

Moreover if we want to determine the coordinate of the hit of the particle entering the detector we have to measure the spread of the avalanched electrons entering the induction gap. This is done by analyzing the signal formation on the readout strips placed at the end of the induction gap below the GEM foil. At this point we are not going to simulate signal formation resulting from a muon entering the detector but rather start with 1000 electrons followed by the electron avalanche and transfer through the holes to the modeling of the signal on the readout electrodes. Each electron will represent a simulated event. The readout electrodes are segmented metal strips placed on an insulator material usually kapton. The strip geometry chosen for our purpose consists of strips all parallel to the y axis (1-D readout). The width of one strip plus the space between two strips is also called the pitch size, the electrode z height is set to 5 μm. The electron cloud refers to the total distribution of the avalanched electrons below the GEM foil able to induce a signal. Figure 6.3 shows a micro-photograph of two 2-D readout pattern.

For visualizing the signal induction inside a GEM detector we have to access the electron endpoints (x_f, y_f, z_f, t_f) of the electron cloud distribution. Figure 6.4 shows the retrieved endpoint distribution along on transverse coordinate x. This distribution will be used for simulating the signal induction for a single GEM.

The Ramo-Shockley theorem is used for modeling the current as a function of the electron drifting time inside the induction gap which requires the knowledge of the drift velocity of the electrons and more importantly the weighting fields for the electrode. The latter can be obtained analytically for simple geometries. However in our case a numerical

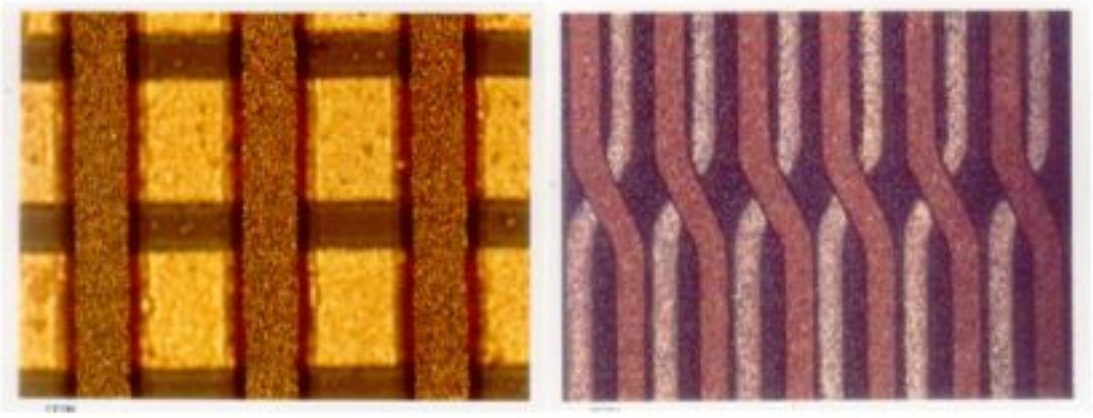

Figure 6.3: Micro-photograph of two readout patterns. Left: Cartesian 2-D readout strip pattern on a kapton ridge. Distance between strips is 200 μm and the strip width 50 μm and 150 μm for the top and bottom layer respectively. Right: small-angle stereo readout pattern separated by 25 μm thick kapton ridges [53]

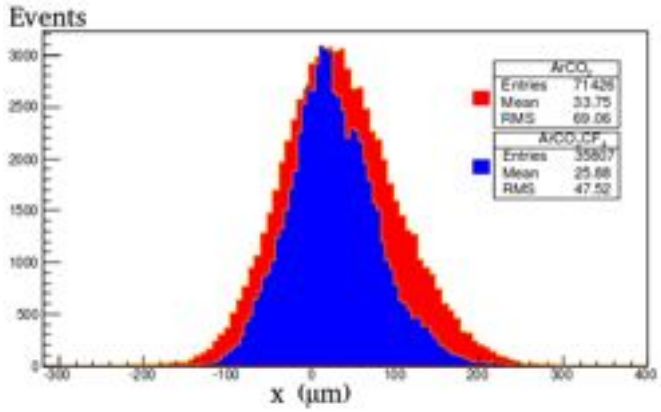

Figure 6.4: Transverse distribution along the x coordinate of all the electrons arriving at 470 μm below the GEM foil for two different gases $ArCO_2$ (blue) and $ArCO_2CF_4$ (red)

approach is needed where the values of the weighting field in each space coordinate can be derived by Ansys.

Garfield is used to simulate the electron avalanche of the initial 1000 electrons and the charge transport through the gas taking into account the weighting field of the strip. We are going to use typical a electric field value of $5kV/cm$ inside $ArCO_2CF_4$ 45:15:40 and $ArCO_2CF_4$ and induction gap distance of 1 mm. The voltage of the GEM foil is fixed to $350V$.

6.2.1 Single electrode

Starting with 1000 initial electrons, we first simulate the electron avalanche and the charge transport through the GEM holes. Keeping only electrons that are able to drift beyond the 470 μm (See Figure 6.4)) below the lower copper plate we retrieve the spatial distribution in the (x, z) plane as well as the arrival time of the individual electrons. Using the appropriate field map for the electrode weighting field we can compute the electron drift towards the z = -1 mm by applying the Ramo-Shockley theorem.

Figure 6.5 shows the signal induced by the electrons (left) and ions (right). It accumulates the total signal of the 1000 initial electrons that have been avalanched and entered the ionductance gap.

1. The amplitude of the ion signal is of 3 orders of magnitude weaker that the electron signal.
2. The duration of the ion signal is longer than the electron signal.

This can be understood when recalling that the drift velocity of the ions is about 1000 times smaller than that of the electrons hence generate a weaker signal. The ions created inside the GEM foil during the avalanche are drifting in the opposite direction following the field lines of the GEM. As a result they get screened by the GEM foil, are

attached by the upper metal plate hence the signal is strongly suppressed. More over due to their extended drift time $t_{Idrift} = \frac{z_{GEM}}{v_{Ion}} = \frac{50\mu m}{10^{-3}v_e} > 100ns$ where z_{GEM} is the typical thickness of a GEM foil and v_e the electron drift velocity $\sim 1mm/\mu m$. Note that this drift time is very short compared to other gas detectors like MPWC where ions have to drift over distances of several mm during which their gain and hence their rate capability is diminished for an increasing radiation flux rate entering the detector. (See Figure 4.5).

6.2.2 Multiple electrodes

Figure 6.4 shows the charge distribution of the electron cluster below the GEM foil. Since the electron cloud tends to spread in the transverse plane (x, y) a typical procedure of determining the position of the particle's hit on the detector is to analyze the signal formation on multiple readout strips. (See 3.4.1) In this way by applying the method of Center of Gravity which exploits the charge sharing on multiple strips it possible to reduce the spatial resolution below the typical pitch of the strips. Three different electrode widths are taken; 600 μm , 880 μm, 1050 μm separated by a distance of 100 μm.

The corresponding fields maps are obtained by generating the appropriate primitive cell which can be seen on Figure 6.6 where each electrode is indexed by a number. For the first and fifth electrode i.e. those on the border are included half, the second, third and forth entirely. Mirror conditions on the (x, y) axes are imposed to generate the full

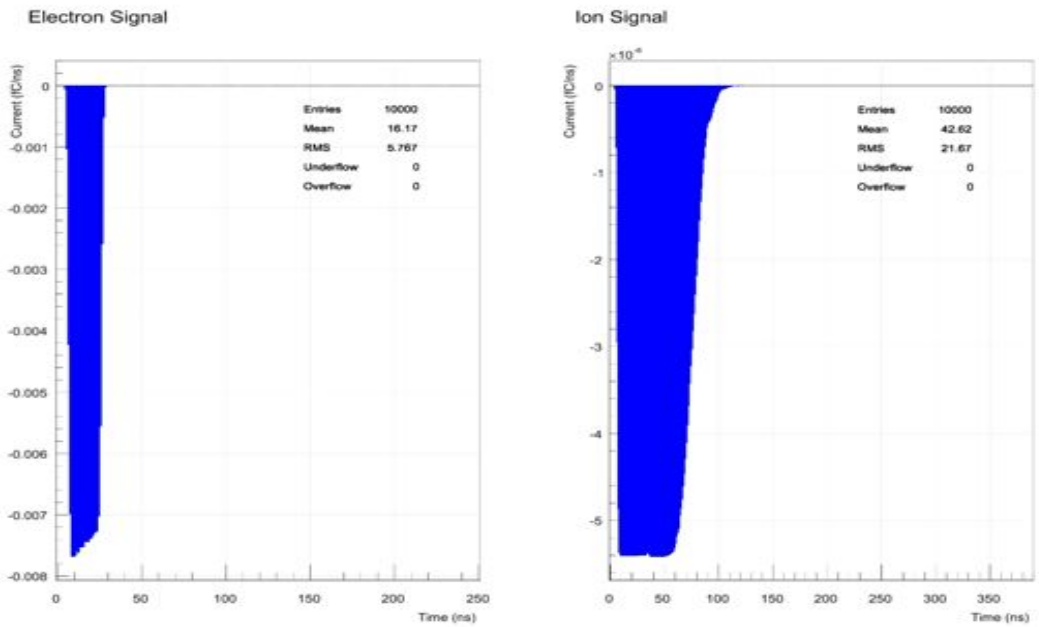

Figure 6.5: Total Electron and Ion signal for $E_{ind} = 5kV/cm$ and induction gap $1mm$ in $ArCO_2CF_4$ 45:15:40

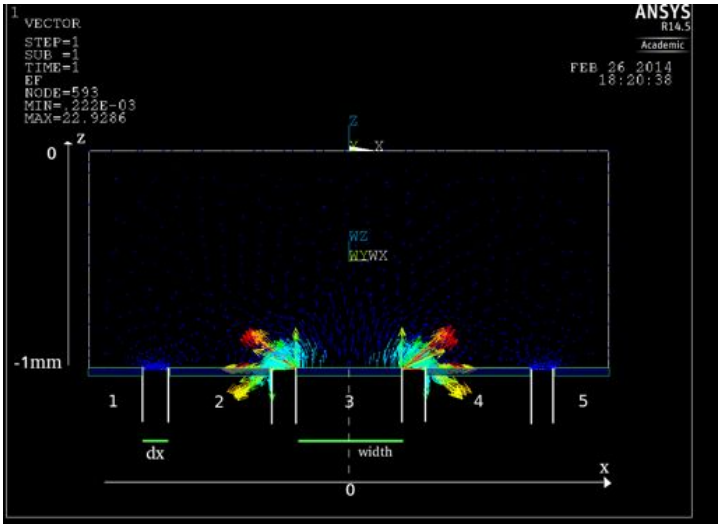

Figure 6.6: Weighting field map for for electrode 3 generated with Ansys. The blue vectors represent the density of the weighting field , the length its intensity . The width is $600\mu m$ where each strip is separated by $dx = 100\mu m$. The blue boxes represent the position of the electrodes

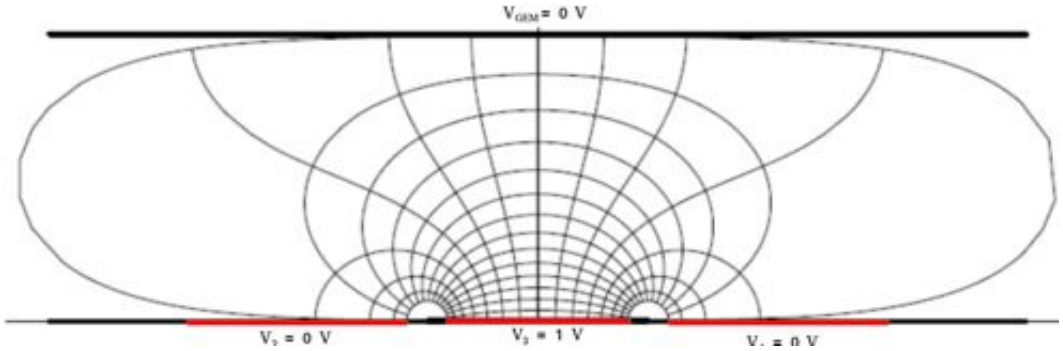

Figure 6.7: Weighting field for the central electrode E3 when putting all the other electrode potentials to zero along with the lower GEM plate (top). Electrodes are shown in red. The field lines can be seen between two conductors with different electric potential. The equipotentials are perpendicular to the field lines (vertical curved lines) . [34]

structure. The corresponding weighting fields for electrode i are obtained by setting all other electrodes along with the lower GEM foil metal plate to the ground $V = 0$. Now we are able to analyze the signal induction on multiple strips. See Figure 6.8.

1. As it can be seen on Figures 6.8 and 6.9 , the signal is induced mainly on the central electrode $E3$. The current is practically zero on the outer electrodes E1 and E5.
2. Electrode 4 and 2 recorded approximately the same amount current.

3. Interestingly we also see a diminishing of the peak intensity of the current with an increasing width values.
4. Finally when comparing the signals for the two gas mixtures we notice that the current is shorter in the $ArCO_2CF_4$ mixture.
5. Then current changes sign for E2 and E4 after 13 ns.
6. Peak intensities are less higher in $ArCO_2CF_4$.

The first observation can be understood by noticing the spread of the electron cluster drifting inside the the induction gap (see Figure 6.4). In fact the cluster spread (69 μm for $ArCO_2$ and 47 μm for $ArCO_2$) only diffuses around the central electrode and doesn't extend enough to reach the neighbor electrodes E1 E2 E4 E5. No electrons enter the region of the E1 E2 E4 and E5 weighting field consequently the current is very much supressed on the latters.

The second point is because electrode 2 and 4 are adjacent to the central electrode.

Thirdly as it can be seen on the field plot of the weighting field on Figure 6.7 the field lines are very dense near the electrode, this is where the electrodes will reach their peak speed and induced the peak value for the current which is proportional to the drift velocity of the electrons. (see equation 3.42) By increasing the pitch size, the field maps approaches the vector field of a parallel plate geometry where the field lines are all parallel to each other hence less dense and electrons reach less speed values and the induced current si smaller.

The forth point can be explained when looking at Figure 6.7. An electron propagating towards the central electrode induces a negative signal on it. Electrons drifting along the most outer curved field lines, approach the central electrode but distant themselves from the adjacent electrodes creating a current of opposite sign.

Lastly we have already shown that the drift velocities of electrons inside $ArCO_2CF_4$ are more important than in $ArCO_2$ hence a shorter signal. This also accounts for the fact that the peak intensity is a bit smaller for $ArCO_2$ than for $ArCO_2CF_4$.

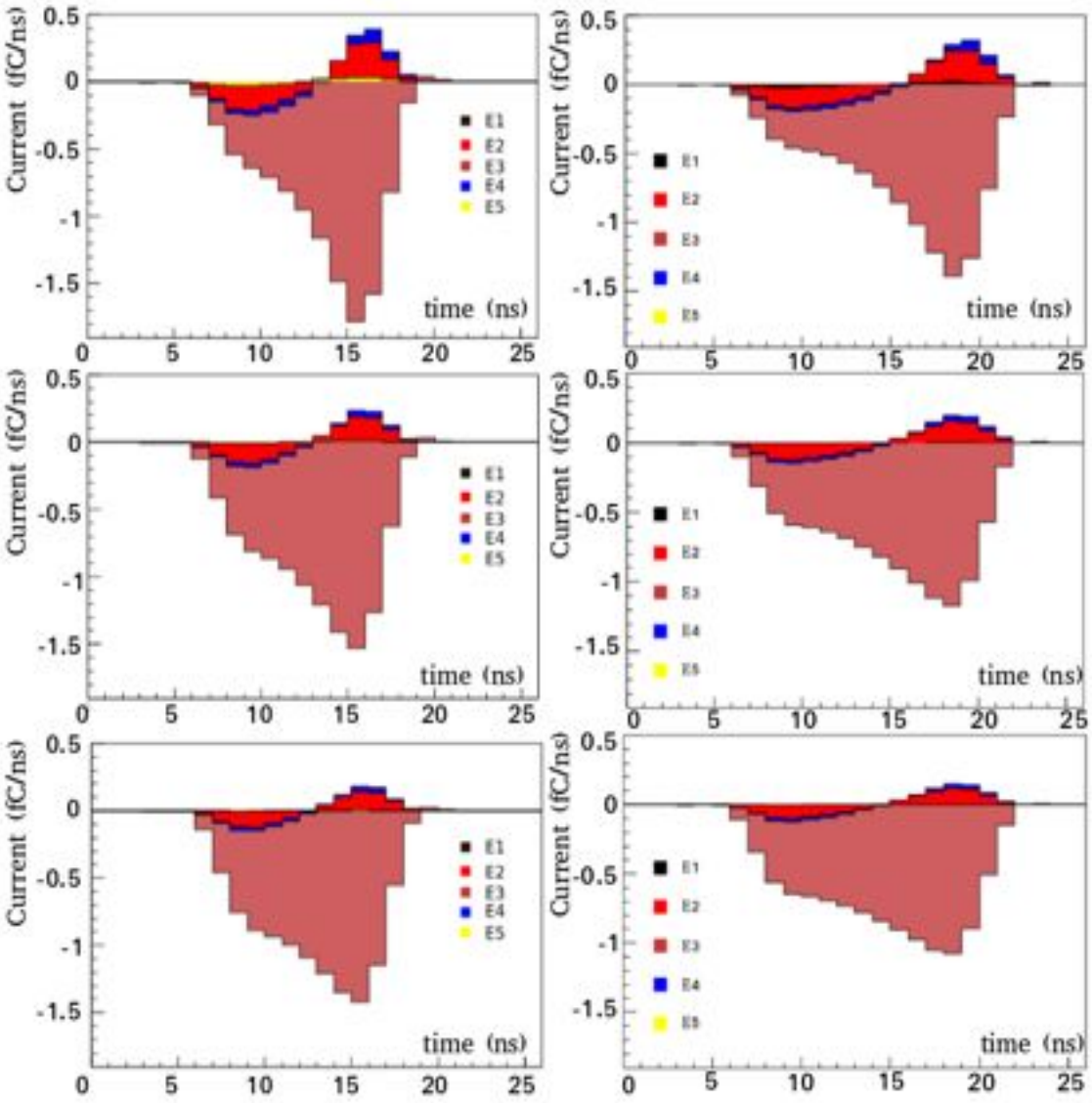

Figure 6.8: Induced signal on 5 electrodes inside the inductance gap for two gas mixtures $ArCO_2CF_4$ (left) and $ArCO_2$ (right) which accumulates the total contribution of all the electrons transfered through the GEM foil. The results are shown for different electrode widths 600 μm (top) 880 μm (middle) and 1050 μm (bottom)

6.3 Conclusions

In this Chapter we extracted two important parameters ; the gain and the transparency. The latter were obtained by relying exclusively on the Garfield framework. Now we have all the inputs for the parametrized simulation exposed in the next Chapter where the signals in a Triple GEM detector are studied.

Moreover the aim of this Chapter was also to give us a better understanding of the functioning of a Single GEM detector when discussing the characteristics of the electron avalanche. We have shown that the effective gain is higher in a mixture in $ArCO_2$ 70:30 than $ArCO_2CF_4$ and increases exponantially with the increasing voltage applied inside the GEM foil.

Furthermore we computed the position of the avalanched electrons below the GEM foil, where we have shown that inside the $ArCO_2$ mixture the distribution of these electron was larger than for the $ArCO_2CF_4$ mixture. This had a direct impact on the shape of the signal induced on the electrodes. We have shown that the signal is shorter inside the $ArCO_2CF_4$ than the $ArCO_2$ mixture anf how the signal decreases for an increasing pitch size. Those results will give us a better understanding when analyzing signal for a Triple GEM detector.

Chapter 7

Signal formation in a Triple GEM

The study of a Single GEM detector has been done by simulating its functioning with a 3-D model using Garfield. The computation of gain and transparency can be done fairly easy and fast , along with the signal induction on the readout electrodes. However this same procedure will be problematic when we apply it on the case of a Triple GEM detector where there are three amplification stages hence the number of electrons to track inside the gas medium increases very quickly. Moreover this will be very time consuming and not very efficient especially when analyzing the signal induced by one single primary electron produced in the drift gap. For instance the signal induction on a single electrode for a Triple GEM computed in a pure Garfield framework will take several hours whereas on multiple electrodes it can take up to one day computation time depending on the processing power. Nevertheless this time constraint can be avoided using an hybrid simulation described in this chapter when discussing signal formation in a Triple GEM. Moreover this is where the results discussed in Chapter 5 and Chapter 6 will we be of importance.

7.1 Hybrid Simulation

As we have already stated, the Garfield framework alone will be too time consuming for the study of signal formation on a single or multiple electrodes on a Triple GEM. A new approach is to perform a parametrized modelisation of all the parameters previously computed with Garfield, Magboltz and Heed. This approach will take the drift velocity, the various diffusion coefficients along with the transparency and the gain values as inputs to parametrize the three multiplication stages and the charge transport inside the gas medium. While Garfield took into account the three spatial coordinates, the parametrized simulation will work in two degrees of freedom, one transverse direction x and the longitudinal direction z. Consequently the computation time will be drastically reduced and it will be possible to study the signal formation on multiple electrodes for Triple GEM detector.

The results of the parametrized simulation can be seen on Figure 7.2 and Figure 7.1

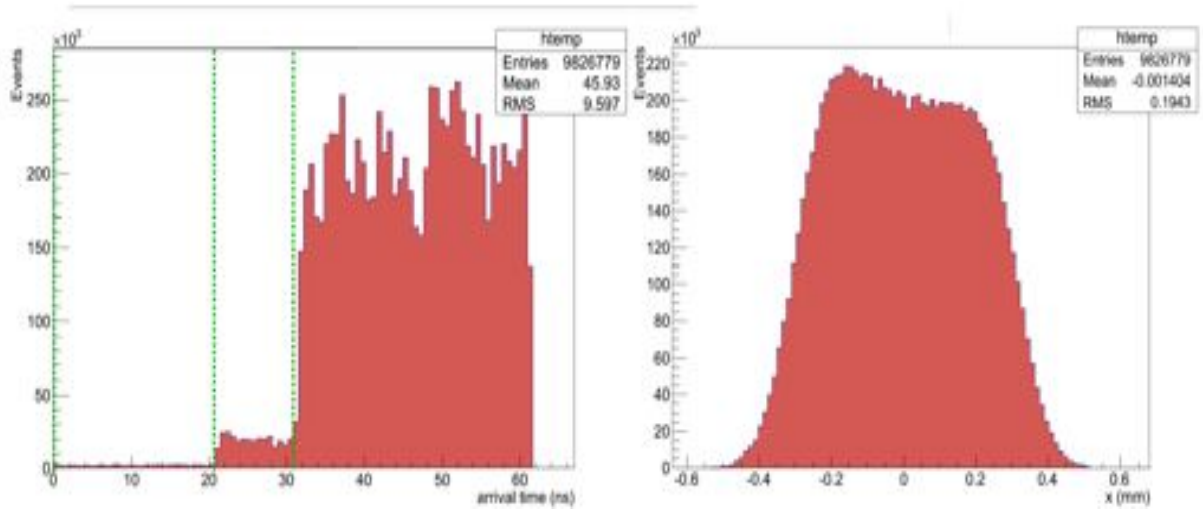

Figure 7.1: Results obtained with the parametrized simulation for $ArCO_2CF_4$ showing the electron arrival time (left) and and the x coordinate below the third GEM foil. The green dotted lines are the positions of the GEM foils.

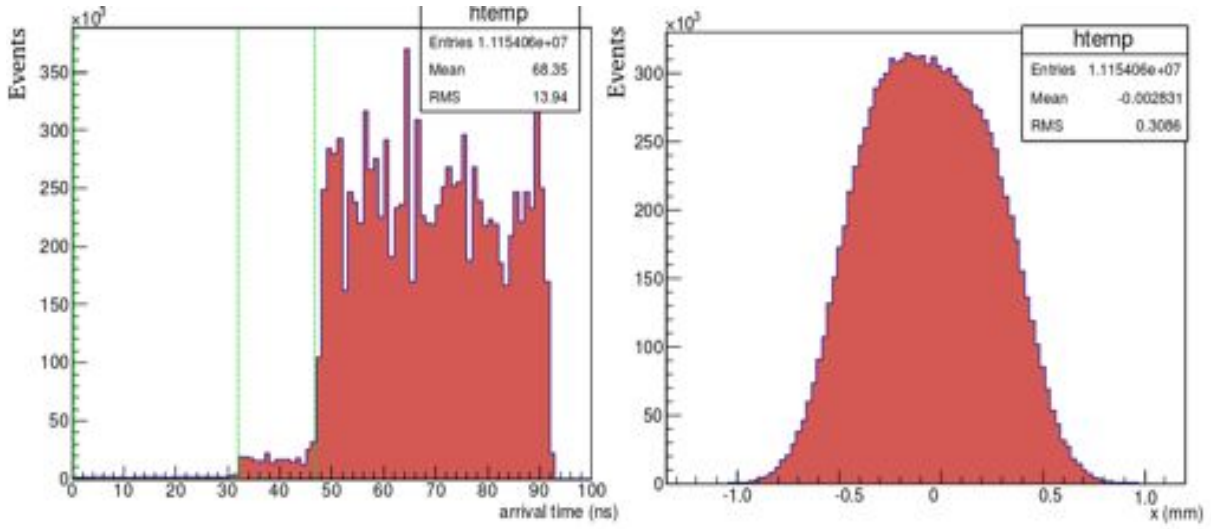

Figure 7.2: Results obtained with the parametrized simulation for $ArCO_2$ showing the electron arrival time (left) and and the x coordinate below the third GEM foil. The green dotted lines are the positions of the GEM foils.

which has been done using the typical drift:transfer1:transfer2:induction gap distances 3:1:2:1 mm in a $ArCO_2CF_4$ 45:15:40 and $ArCO_2$ 70:30 mixture. Gain and transparency results force the following GEM foil voltages and drift/gap/inductance field have been used. A total of 500 primary electrons or events have been simulated.

1. $E_{drift} = 3\ kV/cm$, $E_{transf1} = 3.5\ kV/cm$, $E_{drift} = 3.5\ kV/cm$, $E_{drift} = 5\ kV/cm$
2. $V_{GEM1} = V_{GEM1} = V_{GEM1} = 350\ V$

The dotted lines representing the positions of the three GEM foils converted in time units by taking $v_{drift} \sim 0.1mm/ns$ ($ArCO_2CF_4$) and $v_{drift} \sim 0.07mm/ns$ ($ArCO_2$) for an electric field around 3.5 kV/cm at atmospheric pressure. The large majority of the electrons arrive after 30-60 ns ($ArCO_2CF_4$) and 47-92 ns ($ArCO_2$) on the last GEM foil which correspond to the multiplied electrons originating from the drift gap. This $\sim$ 17 ns delay is due to the difference in drift velocity of the electrons. The x coordinate follows more or less a uniform distribution with a slight bias for negative x. The cause of this bias will not be discussed here and its impact won't influence significantly later conclusions.

Notice the difference in spread for the two gases in the position distribution already encountered for the case of a Single GEM detector where the electrons have spread more transversely in $ArCO_2$ (RMS = 300 μm) than in $ArCO_2CF_4$ (RMS = 190 μm). This can be verified using the alternative equation of 3.19. $\delta D = \sigma_x(ArCO_2) - \sigma_x(ArCO_2) = \sqrt{z} \cdot (D_x(ArCO_2) - D_x(ArCO_2CF_4) = 116\ \mu m$ for drift fields of 3.5 kV/cm where D_x is the transverse diffusion coefficient taken from the results in Section 5.2.3 and z the drift distance between the third GEM foil and the drift gap $z \sim 6\ mm$. δD corresponds approximately to difference in spread seen on Figure 7.2 and Figure 7.1.

7.1.1 Single electrode

Similar to the case of a single GEM the electron cloud drift will be modeled using Garfield but taking taking the parametrized simulation results as inputs. This time the geometry of the GEM i.e. the added transfer gaps will have an impact on the signal. Figure 7.3 shows the electron induced current on a single readout strip of width 600 μm inside $ArCO_2CF_4$. [1]

The duration of the total signal i.e. when the electrons have all arrived at the electrode is much longer than it was for the Single GEM configuration. This is due to the longer drift distance that the electrons, which has been mainly produced in the drift gap, have to travel to reach the induction gap. The signal can roughly be split in three time intervals when comparing to the arrival time shown in Figure 7.1

1. Between 0 ns and 20 ns the induced current is negligible and comes from the electrons multiplied in the transfer 2 gap.

1. The ion signal is not shown since we already proved its poor contribution. The $ArCO_2$ gas is not discussed here since it will give us not much information here but will be presented for the multiple electrodes signal study.

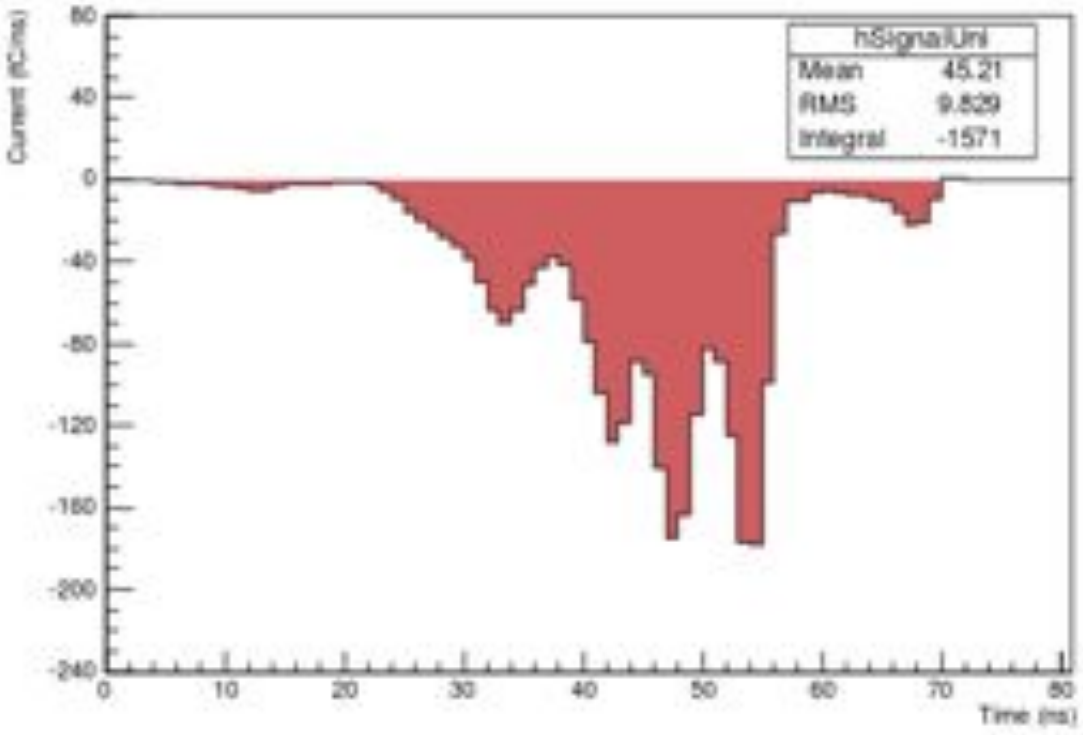

Figure 7.3: Electron signal for a triple GEM induced on a single readout strip of width 600 μm

2. Electrons generated before the transfer 1 gap induce a slightly stronger current between 20 ns and 35 ns.
3. After this time the electron cloud created in the drift gap arrives in the induction gap and induces the peak current that last about 20 ns.

For checking the consistency of the results we should obtain the total number of electrons having entered the induction gap when integrating the $I(t)$ curve over time.

$$Q = \int_0^{70} I(t)dt = -1571C \tag{7.1}$$

We verify that $-1571C = 9826779 \cdot e$ equals the number of entries in Figure 7.1 and where e is the elementary electric charge.

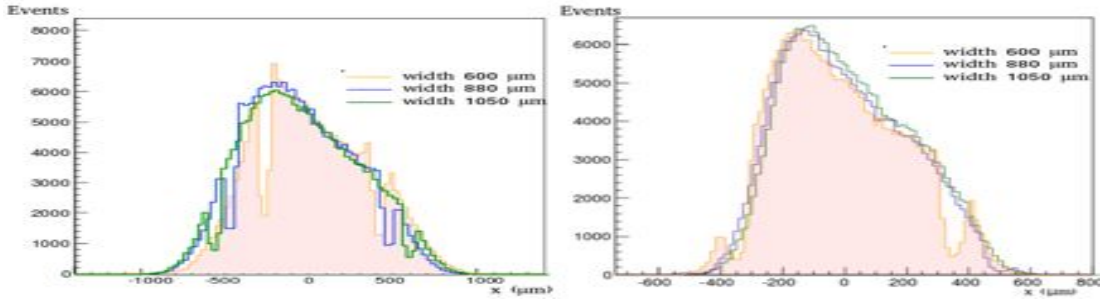

Figure 7.4: Electron position on the electrodes at z = -1 mm for $ArCO_2$ (left) and $ArCO_2CF_4$ (right). The 'holes' in the distribution correspond to the 100 μm interval between electrodes E2-E3 and E3-E4.

7.1.2 Multiple electrodes

More interesting is the signal induced on multiple readout electrodes with various widths separated by a distance of 100 μm. Results are shown on Figure 7.5. where the six top histograms show the induced current shared by five electrodes of widths 600 μm(bottom), 880 μm (middle) and 1050 μm (top). The three left are for $ArCO_2CF_4$ and the three left plots are for $ArCO_2$.

[2] Following observation can be made.

1. The signal is mainly recorded on the central electrode E3.
2. Signals on the outer electrodes E1 and E5 are essentially zero.
3. After the the current on E3 reaches its peak intensity, the amplitude drops quickly to zero.
4. Adjacent electrodes show negative amplitudes.
5. The electric current peak for each electrode decreases with the increasing electrode width.
6. The duration of the signal lasts longer in $ArCO_2$ than inside the $ArCO_2CF_4$ gas mixture.
7. The peak signal induced inside the $ArCO_2CF_4$ is more intense than inside the $ArCO_2$ gas mixture.

Firstly the electron cloud doesn't spread beyond the size of the central electrode. This is true for the $ArCO_2CF_4$ mixture . However the spread inside the $ArCO_2$ is more extended and can induce a signal on the next neighbor electrode E2 and E4. When

2. Without loss of generality only a fraction of the simulated output events of parametrized simulation has been chosen to reduce the computation time, since the amount of electrons inducing the signal would have only changed the global current amplitude. The full event computation would have taken several weeks to complete The events have been chosen uniformly from the arrival times t and position x below the third GEM foil.

looking at Figure 7.4 which shows the the end position (left for $ArCO_2$) of the charges at z = -1 mm, we see that some electrons drifted towards E2 and E3. Moreover there is a slight excess of current recorded by E2 compared to E4 due to the bias in the electron cloud distribution towards negative x (see Figure 7.4).

Secondly , the outer electrodes (see Figure 6.6) are too distant to record a signal. However they show a stronger signal for the $ArCO_2$ strip size 600 μm due to the larger spread for this gas.

Thirdly , as the charge propagates towards the strip and get more and more accelerated due to the higher field density near the electrode, the current increases rapidly until the point where the charges have all reached the electrode causing the signal to vanish.

Moreover all the neighbor electrodes E1 E2 E4 and E5 recorded a negative signal each time the main signal on E3 decreases. This is the same effect that has been encountered for the signal formation for the Single GEM detector. The signal E3 decreases when the electrons arrive near the central electrode resulting in a collection. If electrons originating from the outer boundary of the electron cloud spread, and follows the outer weighting field lines, those electrons will move away from the adjacent electrodes E1 E2 E4 and E5, resulting in a opposite current induction.

The fifth point has already been discussed for the signal induction in a Single GEM detector for multiple electrodes. When increasing the size of the electrodes we approach more and more a parallel plate geometry where the field are all parallel to each other and the electric field gradient is constant and gets less dense near the electrodes. The charges aren't speed up enough towards the strips hence inducing a poorer signal.

The sixth observation can be explained when recalling that electrons drift quicker inside the $ArCO_2CF_4$ than in the $ArCO_2$ mixture. (See Figure 5.9). This account also for the last observation since the induced signal intensity is proportional to the drift velocity of the electrons towards the electrodes.

Finally the results shown on Figure 7.5 are compared to some experimental results shown on Figure 7.6 and Figure 7.7. Notice the similarity between the shapes of the simulated signals in the $ArCO_2$ mixture and Figure 7.6. Additionally we recognize the crosstalk manifested by the negative amplitude on electrode 1 (red) when the main signal 3 (blue) decreases. Figure 7.7 shows different types of signal shapes resulting from different ionization profiles. Depending in which gap the primary particle creates more ionizations the signal shape will vary and shows multiple peaks. Each peak is separated by an interval depending in which gap the electrons have been generated [3] The first profile (left) corresponds to the case where most electrons where created in the drift and transfer 2 gap, second profile (middle) corresponds to the case where most electrons where created inside the transfer 1 gap and some in the drift region. Whereas the third profile shows the scenario comparable to our simulations where most electrons where created in the drift gap.

3. The drift velocity for a 4.5 kV/cm inside $ArCO_2$ is 0.075 mm/ns corresponding to a time interval of 40 ns between each gap.

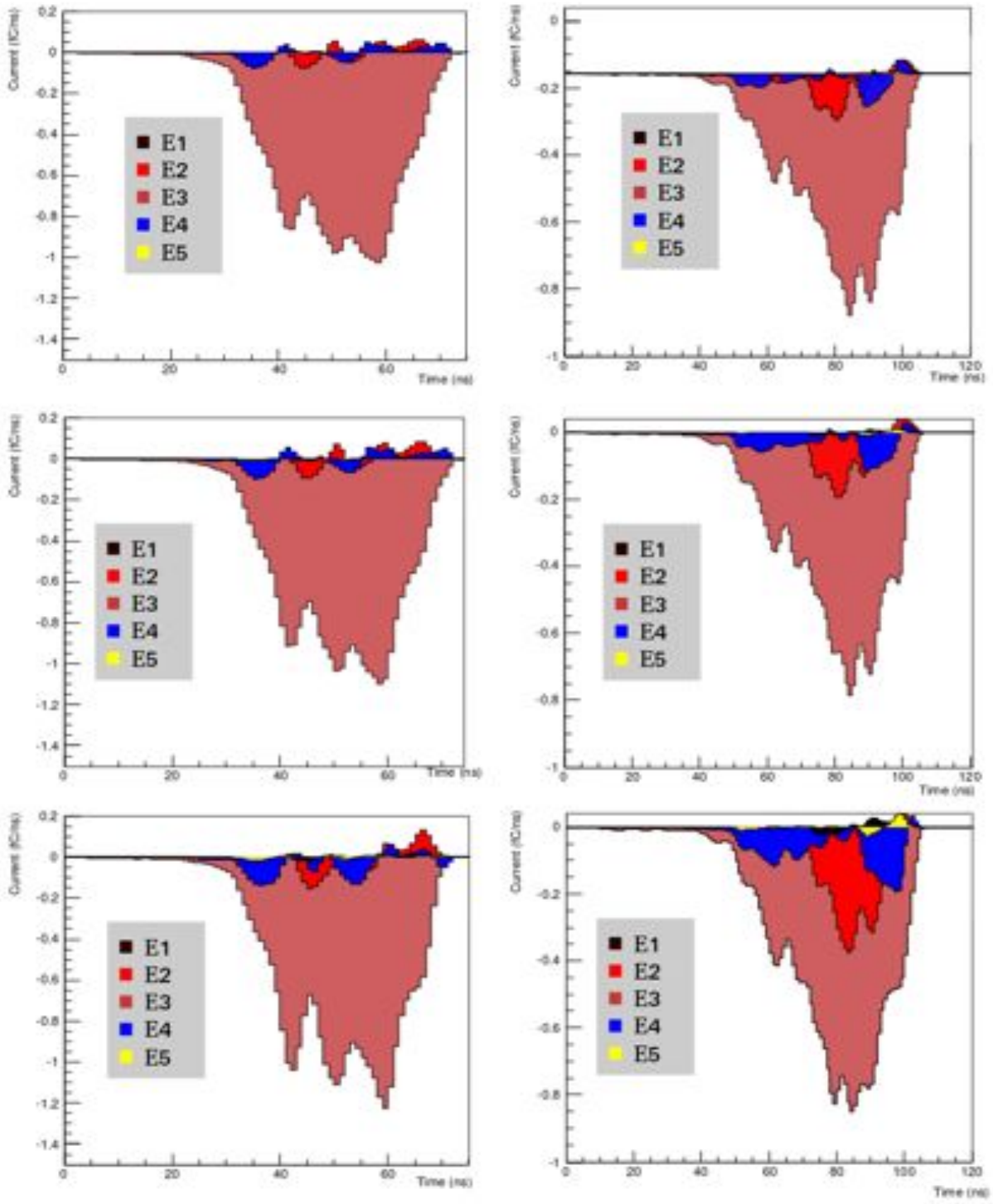

Figure 7.5: Signal induced on multiple electrodes with different strip widths, 1050 μm (top) , 880 μm and 600 μm (bottom). Left are shown the signal induction inside $ArCO_2CF_4$ mixture and right $ArCO_2$. The color of the histograms indicate the number of the electrode shown in the legend

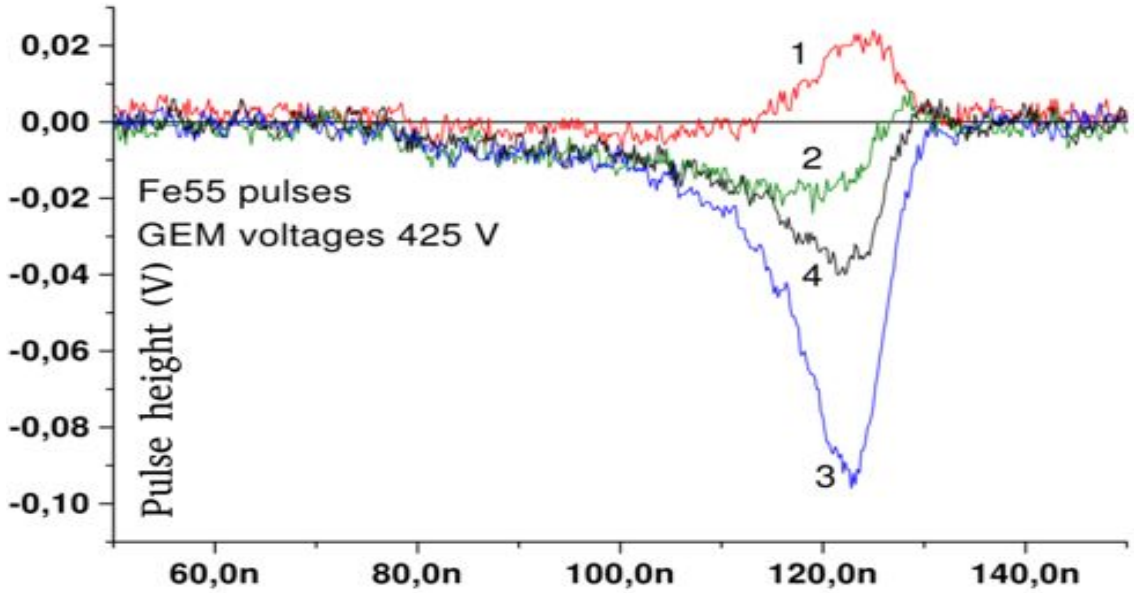

Figure 7.6: Signal induced on multiple electrodes inside a $ArCO_2$ 70:30 mixture with an electrode width of 500 μm. The numbers next to the signals indicate their position . 3 is the central strip, 2 and 4 the first neigbors and 1 the second neigbor. [54]

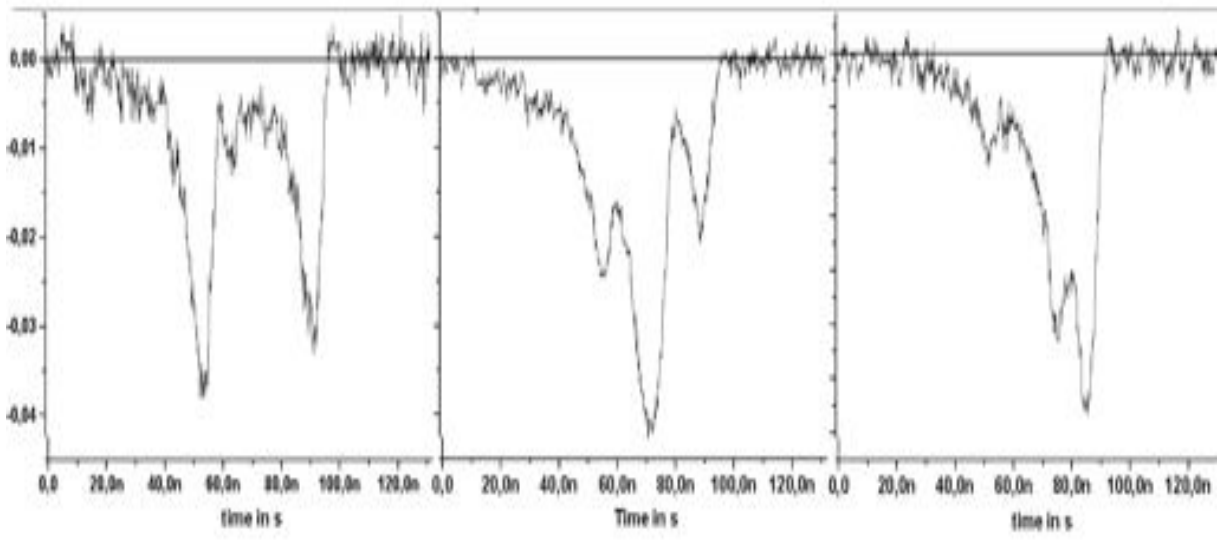

Figure 7.7: Signals induced inside a Triple GEM prototype for the LHCb experiment in a $ArCO_2$ 70:30 mixture. The gap distances are all 3 mm and have all the same gap fields of 4.5 kV/cm. [54]

7.2 Conclusions

In this Chapter we exposed a new method for modeling the signal induction inside the a Triple GEM detector. An emphasis was made on the hybrid simulation which needed the results derived in Chapter 5 using Magboltz, Heed and Garfield; the energy loss of the primary particle inside the detector, the drift and diffusion properties of the electrons inside the gas and the characteristics of the electron avalanche. These results were needed inputs for the 2-D parametrized simulation of the Triple GEM which enabled us to efficiently simulate the whole Triple GEM response where else a pure Garfield framework would have taken too long. By extracting the outputs of this simulation ; the (x, t) coordinates of the electrons below the third GEM foil we returned to the Garfield framework for modeling the signal formation on a single and multiple electrodes.

Furthermore we confirmed the validity of our end results with experimental data which gave us a preliminary proof of the power and efficiency of the hybrid simulation.

Chapter 8

Gain measurements in a Triple GEM

In this Chapter will generalize the gain study of a Single GEM to a Triple GEM. Again the whole simulation part will be done using Garfield for the gain and transparency computation for two different gas mixtures. Moreover we would like to confront those results with real gain measurements that will be taken using a Triple GEM prototype.

8.1 Voltage divider

In the CMS Triple GEM detector the voltage of every electrode (drift electrode and GEM copper layers) is applied through a voltage divider as shown in Figure 8.2. [1]

$$V_i = hV \cdot \frac{R_i}{R_{DIVIDER} + 0.3M\Omega} \tag{8.1}$$

By increasing the values for the high voltage hV the voltages across the GEM foils along with the drift, transfer and inductance field are increasing See Figure 8.1.

8.1.1 Simulation results

In this work we chose to compute the effective gain of a Triple GEM detector from the simulation of a single GEM detector using the formula 8.2. With this approach we have first to compute the electric field in each gap, the potential difference in each GEM foil and simulate the corresponding single-GEM effective gain $G_{eff}(i)$

$$G_{eff} = \cdot G_{eff}(1) \cdot G_{eff}(2) \cdot G_{eff}(3) \tag{8.2}$$

The computed effective gain values are plotted on Figure 8.3 as a function of the high voltage.

1. This solution has been chosen by CMS instead of applying the voltages independently to each electrode to minimize the number of cables and the number of power supplies.

HV (kV)	GEM1 (V)	DRIFT (kV/cm)	TR1 (kV/cm)	GEM2 (V)	TR2 (kV/cm)	GEM3 (V)	IND (kV/cm)
3.6	341	2.07	3.10	310	3.10	279	3.10
3.7	351	2.13	3.19	319	3.19	287	3.19
3.8	360	2.18	3.28	328	3.28	295	3.28
3.9	370	2.24	3.36	336	3.36	303	3.36
4	379	2.30	3.45	345	3.45	310	3.45
4.1	389	2.36	3.53	353	3.53	318	3.53
4.2	398	2.41	3.62	362	3.62	326	3.62
4.3	408	2.47	3.71	371	3.71	334	3.71
4.4	417	2.53	3.79	379	3.79	341	3.79
4.5	427	2.59	3.88	388	3.88	349	3.88
4.6	436	2.64	3.97	397	3.97	357	3.97
4.7	446	2.70	4.05	405	4.05	365	4.05
4.8	455	2.76	4.14	414	4.14	372	4.14
4.9	465	2.82	4.22	422	4.22	380	4.22
5	474	2.87	4.31	431	4.31	388	4.31
5.1	484	2.93	4.40	440	4.40	396	4.40

Figure 8.1: GEM foil voltage and gap field tables for the Triple GEM prototype

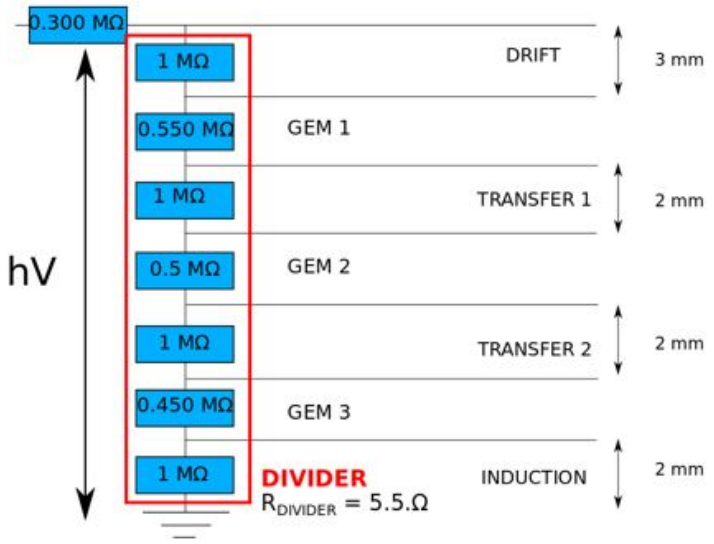

Figure 8.2: Tension divider inside the ULB triple GEM prototype 1

1. As we have already obtained for the Single-GEM, the gain increases exponentially when applying a higher voltage.
2. Moreover the results show consistently that the gain is higher for the $ArCO_2$ gas than for the $ArCO_2CF_4$ mixture.
3. The trend stays exponential until reaching a plateau above a high voltage of 4.9 kV.

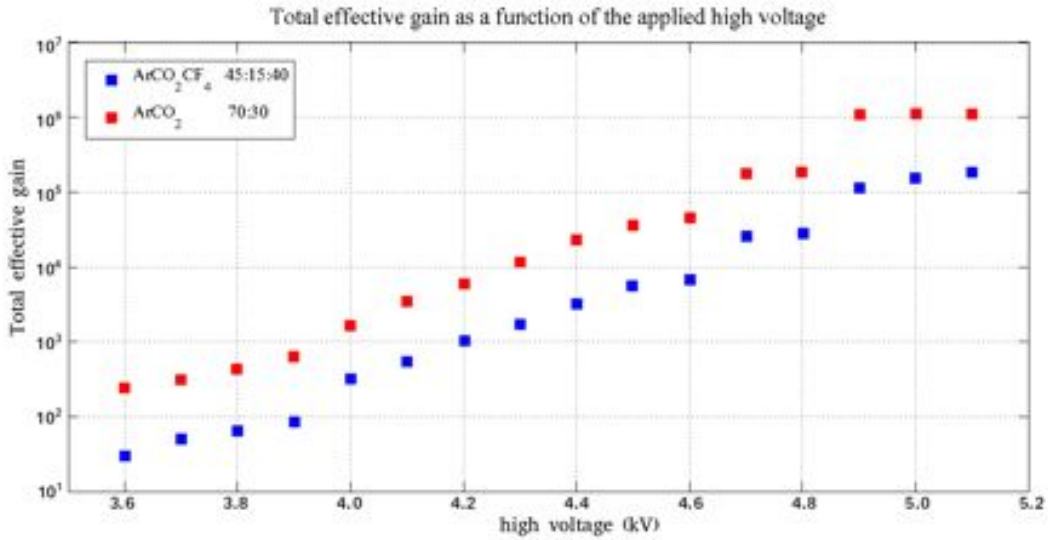

Figure 8.3: total effective gain of a triple GEM detector with gap distances 3:2:2:2 mm as a function of the high voltage. The gain is shown for two different gas mixtures $ArCO_2$ 70:30 and $ArCO_2CF_4$ 45:15:40

The first two observations have already been discussed in Section 6.1.2. The third observation can be understood qualitatively when referring to 6.1.2 where it has been stated that for higher induction fields the extraction of electrons out of the GEM foil is more efficient. Additionally a more intense drift field , the field lines are directed towards the upper metal plates of the GEM foil, where as for lower drift field values this effect diminishes and more electrons get injected into the GEM holes. Keeping this is mind , for high voltages above 4.9 kV the high extraction effect due to a higher induction field is compensated by a decreasing injection effect due to a higher drift field.

8.2 Experimental setup

This section exposes the experimental study of a Triple GEM detector which will help us to confront the previous simulated results with real measurements.

Figure 8.4 shows the the small Triple GEM prototype 10x10cm which will be used for the following gain measurement study. The drift:transfer1:transfer2:induction gap distances are 3:2:2:2 mm and a mixture of $ArCO_2$ 70:30 is used. In right upper corner and left lower corner are plugged the gas input/output flow tubes. For the following studies only 1-D readout is used. The connectors with each 128 channels for the readouts can bee seen on Figure 8.4 next to the upper gas tube. The raw signal is first transmitted through the connectors to a preamplifier and a shaper and finally readout on an oscilloscope.

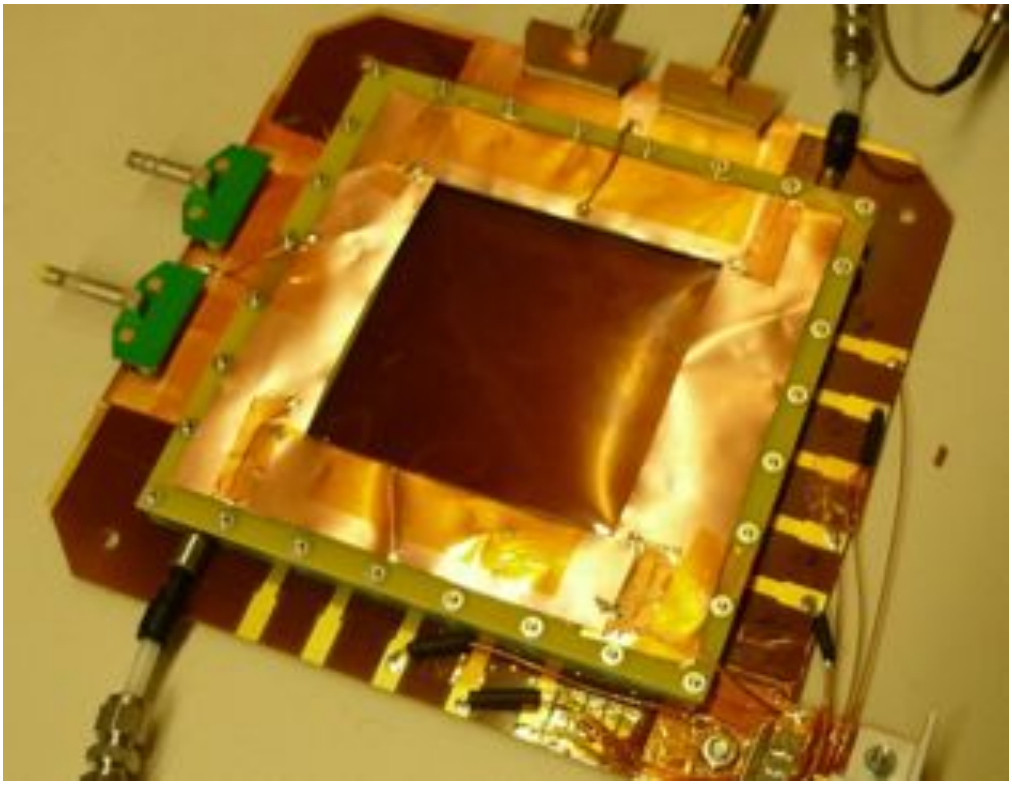

Figure 8.4: Photograph of the small Triple GEM prototype 10x10cm

8.2.1 Primary particle spectrum

The radioactive source at our disposal is a iron 55 source which emits photons in the keV scale a spectrum peak at $5.9keV$. The latter will enter the GEM and ionize an argon atom, extracting an electron from an inner atomic orbital with energy $E_e \sim 3keV$. The corresponding hole will be filled with an electron from an outer orbital which will result in an emission of a δ photon with $E_\gamma = 2.9keV$.

Figure 8.5 shows the Fe_{55} energy spectrum where the highest peak corresponds to the $5.9keV$ and the other to the $3keV$ peak called the Argon escape peak. The first represents the total energy of the $5.9keV$ photon deposited inside the detector. If the δ photon escapes the detector without interacting inside the gas, only the remaining $3keV$ are absorbed and converted into an electric signal producing the escape peak.

8.2.2 Calibration

The energy deposited inside the detector is converted proportionally into an electric signal seen on the readout electronics. The primary electrons are multiplied by a certain gain factor G which we want to measure. Those multiplied electrons induce a signal on the electrodes which is then sent to a series of preamplifier before being visualized on an

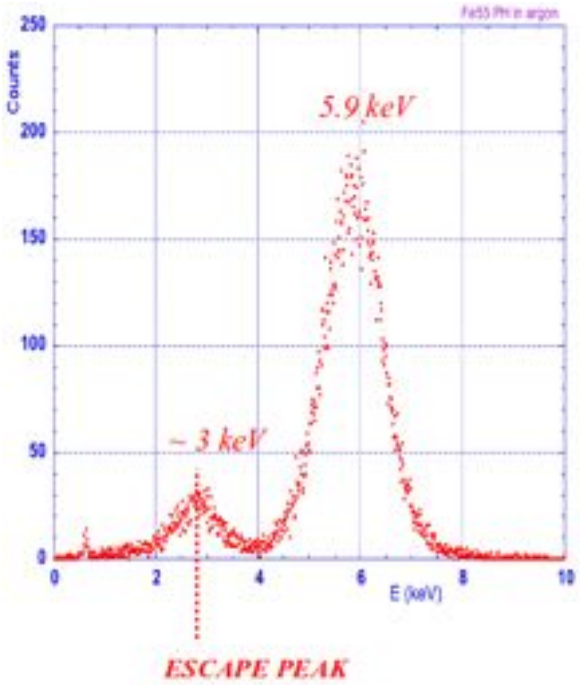

Figure 8.5: Iron 55 energy spectrum with its peak emission at 5.9 keV and the argon escape peak at $\sim$ 3 keV [55]

oscilloscope.

Supposing that the readout electronics convert the induced current linearly to the observed signal on the oscilloscope we can make the following calibration. By sending a square electric impulse through a capacity into the amplification electronics of charge $Q_{inj} = C \cdot V_{inj}$ where $C$is the capacitance and V_{inj} the voltage applied. A signal with amplitude V_{out} is read out at the output of the amplifier which is proportional to the injected charge $V_{inj} \sim C \cdot V_{inj}$. By varying the voltage of the injected signal we are able to retrieve a linear correlation between the injected and output signal. The peak of the the output signal is chosen to be the peak value V_{out}

Figure 8.6 shows the calibration curve where we verify that the relation between the input and output signal is linear. The input voltage is converted into the number of electrons The coefficient of the slope $\beta = 0.0004$ can be extracted to retrieve the induced charge on the readout electrodes.

8.2.3 Effective gain measurement

After calibration we are now able to compute the gain by simply identifying the peak voltage $V_{5.9keV}$ induced by the 5.9 keV photon, readout on an oscilloscope. This is repeated for different values of the high voltage. The gain can then be calculated by

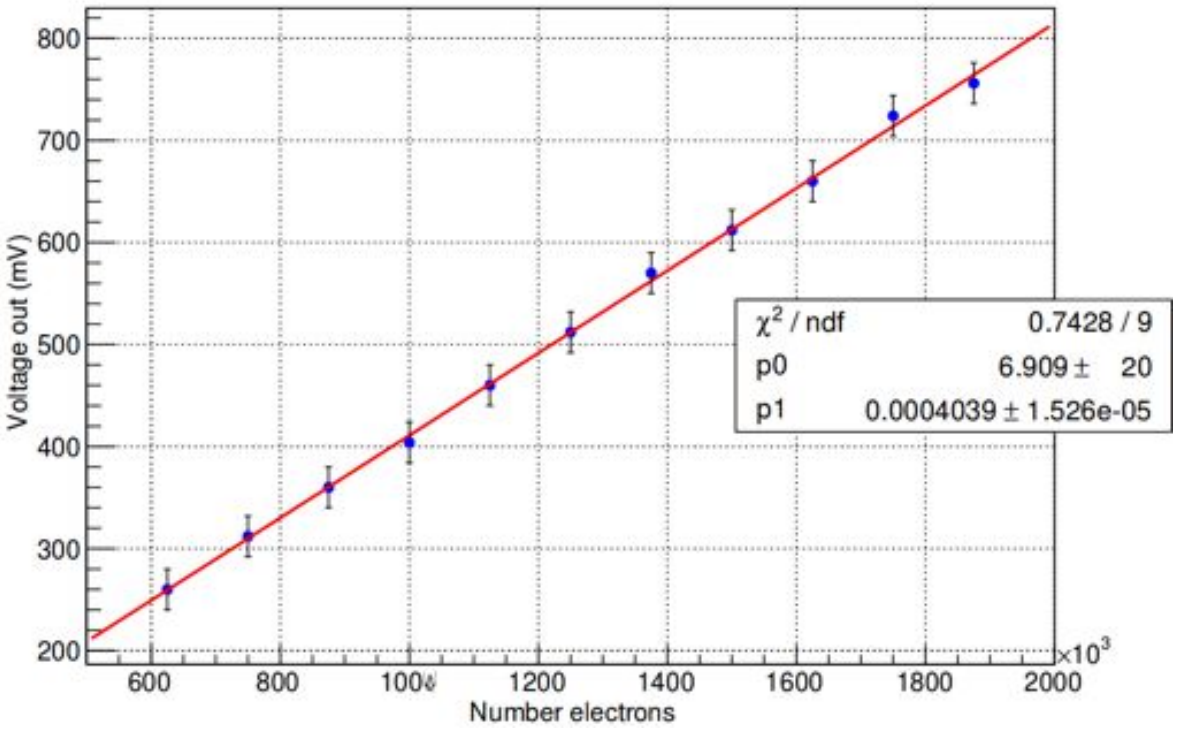

Figure 8.6: Calibration curve showing the voltage at the output of the preamplifier as a function the injected number of electrons

$$G = \frac{n_{5.9keV}}{n_{prim}} = \frac{V_{5.9keV}}{\beta \cdot n_{prim}} \tag{8.3}$$

where $n_{5.9keV}$ is the number of electrons resulting from the avalanched primary electrons n_{prim}. The latter can easily be derived by applying the following equation [56]

$$n_{prim} = E_\gamma \left(\frac{\%Ar}{W_{Ar}} + \frac{\%CO_2}{W_{CO_2}} \right) \tag{8.4}$$

where $E_\gamma = 5.9\ keV$, $\%Ar$ and $\%$ are the proportions of the gas mixtures 0.7 and 0.3, W are are their corresponding ionization energies 26 eV and 34 eV listed in Section 3.2.2. We get following results shown on Figure 8.7. Red and blue points correspond to the Garfield gain simulation results, red and violet correspond to the gain measurement taken on the Triple GEM prototype. The first are measured using the method exposed above while the second were taken at CERN using more precise calibration methods.

1. The simulated gain value are higher than the gain measurements taken on the Triple GEM prototype
2. Measurements taken (at CERN) on the same prototype are consistent with the Garfield simulation results but deviate below a high voltage of 4 kV

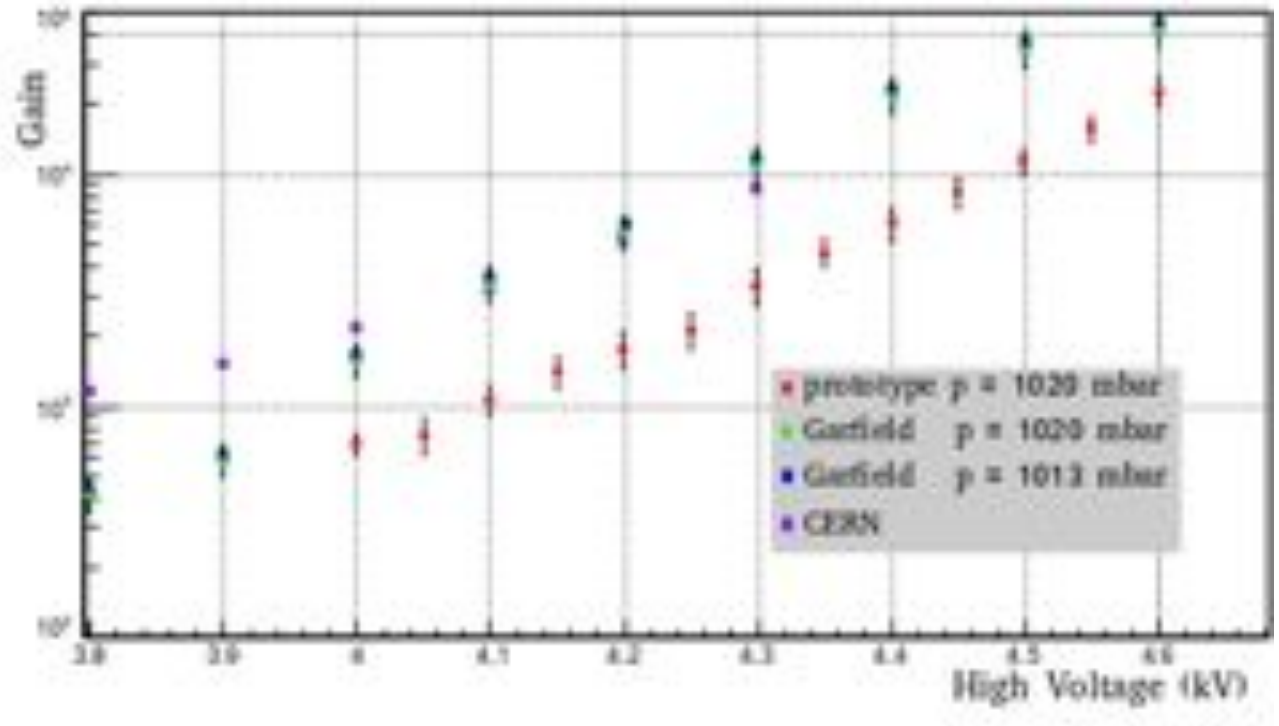

Figure 8.7: Gain as a function of the high voltage applied on the Triple GEM. Garfield simulation results for gas pressures of 1020 $mbar$ (green) and 1013 $mbar$ (blue) are shown. Error bars are too small to be visible. Experimental results are shown for the Triple GEM prototype (red) and measurement for the same prototype taken at CERN (violet).

3. An increased pressure seems to lower the gain by 10 % for the Garfield simulation.

8.3 Conclusions

This Chapter was dedicated to gain study of a Triple GEM detector where the gain value were fist simulated for each GEM foil individually then multiplied together taken into account the transparency for each foil. The results were then confronted with measurements taken on a Triple GEM prototype and deviated by a factor of 70%. Infact the experimental setup described in this Chapter was not precise enough since we used a analogical readout on an oscilloscope. Nevertheless some measurements were taken on the same prototype using a more precise calibration based on a digital readout. This was done through the use of a Analog-to-Digital Converter (ADC) where the signal leaving the amplifier electronics is converted into a digital signal. The outcome of these measurements match the simulation values for high voltages above 4 kV.

Conclusion

'Go away! Last words are for
fools who haven't said enough!"

Karl Marx

This work aimed at studying and characterizing a Triple GEM detector for the upgrade of the CMS muon spectrometer and in particular to the understanding of its signal formation on multiple anodes.

The LHC will run at luminosities beyond the planned $10^{34}\ cm^{-2}\ s^{-1}$, after the LS2 upgrade in 2019. For preparing the CMS experiment for the high particle fluxes and background rates that will diminish the efficiency of the L1 Trigger and the muon identification region of the muon spectrometer, the CMS GEM collaboration has proposed the Triple GEM technology to be instrumented in the forward region of the muon chambers. This new detector will be inserted in the $1.6 < |\eta| < 2.1$ region of the muon chambers in the vacant space initially foreseen to host RPCs. Nowadays, the GEM technology has been proved to sustain high rates of radiation as high as 10 $MHz\ cm^{-2}$ without loosing significant detection efficiency and yielding spatial resolution between 170 and 340 μm.

To better understand the functioning of the CMS Triple GEM detector we have developed a parametrization of the response of the detector based on results obtained with a 3-dimensional Monte Carlo simulation. In particular we have studied the signal formation on the micro-strips anodes of the detector.

Firstly we started by studying some preliminary phenomena which included the simulation of the interaction of primary particles inside two different gas mixtures $ArCO_2$ (70:30) and $ArCO_2CF_4$ (45:15:40) using Heed. We observed how the various primary particles, muons, pions and proton interact losing a fraction of their energy inside those gases, predicted by the Bethe curves. Moreover we computed the number of primary electrons produced during the ionization process involving the primary particles and the gas atoms.

Furthermore with the use of Magboltz we were able to simulate the transport and diffusion properties of the charge in the gas. As a result we retrieved the drift velocities, diffusion coefficients of the charges inside two gas mixtures $ArCO_2$ (70:30), $ArCO_2CF_4$ (45:15:40) in the presence of a electric and magnetic field. We concluded that the choice of these two gas mixtures along with the varying intensity of the electric field will affect the response of the detector. The drift velocities of electrons inside $ArCO_2$ are about 30 % lower for typical drift fields encountered in GEM detectors.

Later on we concentrated on the simulation of the avalanche inside the detector where we had to generate the appropriate electric field maps depending on the values of the GEM foil voltages and the gap fields. Using Garfield we showed that the latter will strongly impact the multiplication process of the electrons, described by the gain

and transparency of the GEM. Again the results were presented for the two gas mixtures where we concluded that their choice will strongly affect the performance of the detector. This was followed by the signal formation simulation of a Single GEM detector relying purely on Garfield, a qualitative study for the modeling of the signals inside a Triple GEM detector.

Having extracted all the necessary parameters in this 3-D Monte Carlo simulation; the energy loss, the number of primary clusters, the diffusion and drift properties, transparency and the gain of the GEM foils, we have to proceed with the hybrid simulation of a Triple GEM detector. This simulation combined the previous parameters obtained with Garfield and the parametrized simulation. This was a powerful and efficient way to retrieve the electron cloud spatial and temporal distribution at the the end of the third multiplication below the GEM foil. Similarly as for the Single GEM detector we continued with the Garfield framework for modeling the formation of signals on a signal and multiple electrodes. Moreover the results were confronted with experimental data which gave us a first glimpse of the validity of our simulation. Moreover we concluded that the signals lasted longer in a $ArCO_2$ than in a $ArCO_2CF_4$ mixtures and that for the first gas, the induced total charge was better distributed multiple electrodes.

The last Chapter concluded the study of the Triple GEM detector by a effective gain and transparency simulation. This was done using Garfield by first computing avalanches on each GEM foil separately and then combining the results to extract the effective gain of a Triple GEM detector. Additionally those results were confronted with measurements recorded with a Triple GEM detector in the setup recently built in our laboratory. Our gain measurement is not in agreement by a factor of 50 % with the simulation. However the simulation results are in very good agreement with measurements performed at CERN with the same prototype. The Brussel's setup being completely new, we are still investigating a possible problem in the calibration procedure.

The presented results are also aimed to give a baseline for further studies regarding the simulation of a Triple GEM detector. As we have shown in Chapter 5, the presence of the magnetic field inside CMS in the muon chambers, has a non negligible effect on the drift properties of the electrons inside the gas, especially transverse diffusion. The latter was decreased due to the magnetic field and has not yet been integrated in the parametrized simulation. Test beams will soon be made by the CMS collaboration on full-scale GEM prototypes with magnetic fields to reproduce the CMS endcap environments.

Appendix A

The following histograms have been generated with Heed and show the primary cluster distribution for different primary particle e.g. muons, charged pions and protons at different energies in two different gas mixtures $ArCO_2$ 70:30 and $ArCO_2CF_4$ 45:15:40. The length of the track has been simulated inside a gas volume along one coordinate of total length 7 mm for a total of 1000000 events. The table below contains all the extracted mean values for these distributions. If the distributions were normalized the mean value would coincide with the most probable number of primary clusters produced.

$\mu+/\mu-$			$\pi+/\pi-$		
E (GeV)	$ArCO_2$	$ArCO_2CF_4$	E (GeV)	$ArCO_2$	$ArCO_2CF_4$
1	20.97	27.94	1	20.37	27.15
5	25.03	32.88	2	21.99	29.2
10	26.03	34.03	5	24.39	32.17
15	26.33	34.39	8	25.38	33.28
20	26.47	34.57	10	25.72	33.66
100	26.78	34.89	50	26.66	34.78
500	26.82	34.93	100	26.76	34.88
1000	26.83	34.93	200	26.8	34.91

p+		
E (GeV)	$ArCO_2$	$ArCO_2CF_4$
1.5	25.78	34.4
2	21.25	28.39
3	19.66	26.22
4	19.61	26.16
5	19.86	26.47
8	20.73	27.63
10	21.25	28.32
50	25.26	33.14
100	26.13	34.17
200	26.52	34.62

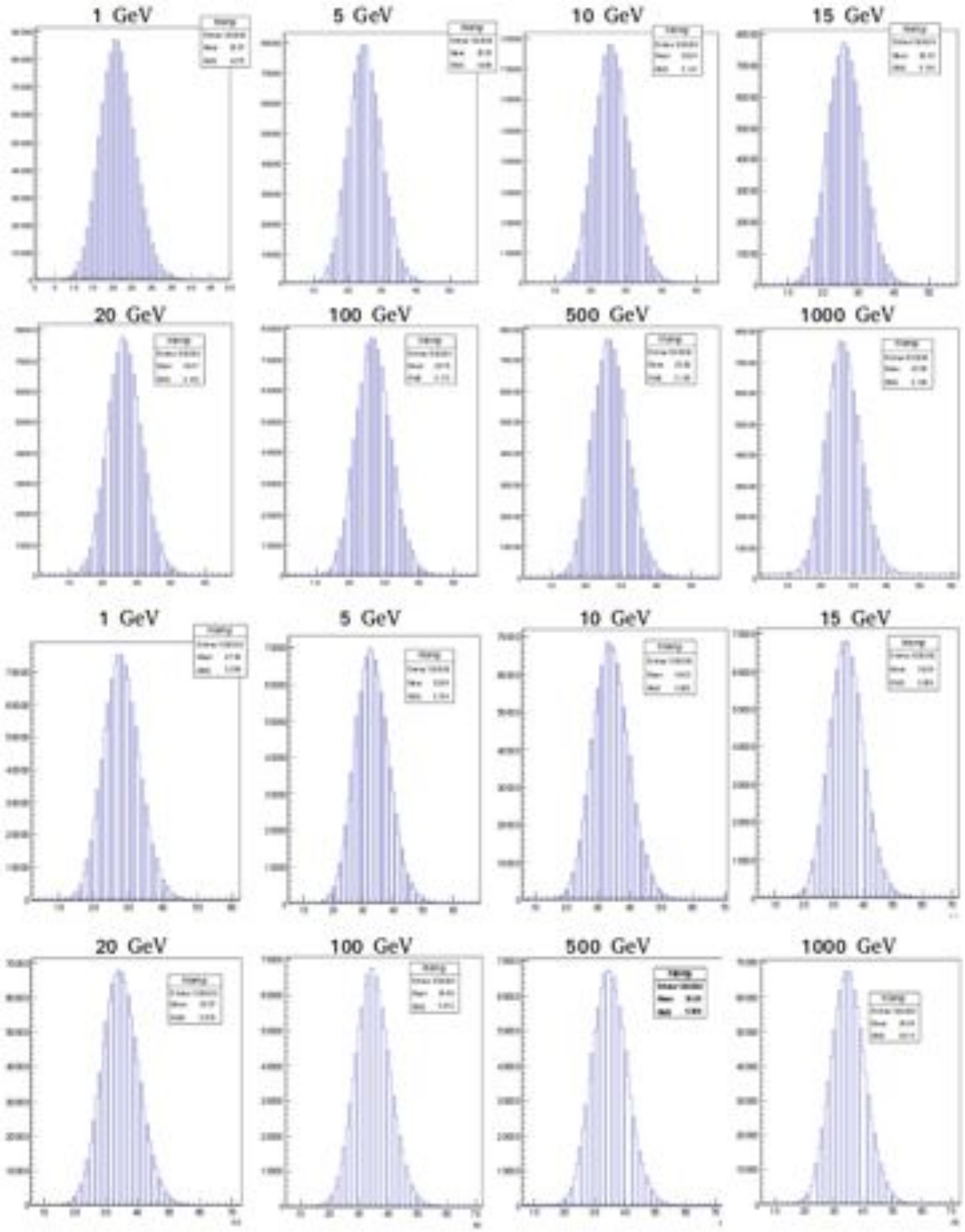

Figure 8.8: primary cluster distribution for muons along a 7 mm track for different energies, produced inside two different gas mixtures ; top eight $ArCO_2$ 70:30 , lower eight $ArCO_2CF_4$ 45:15:40

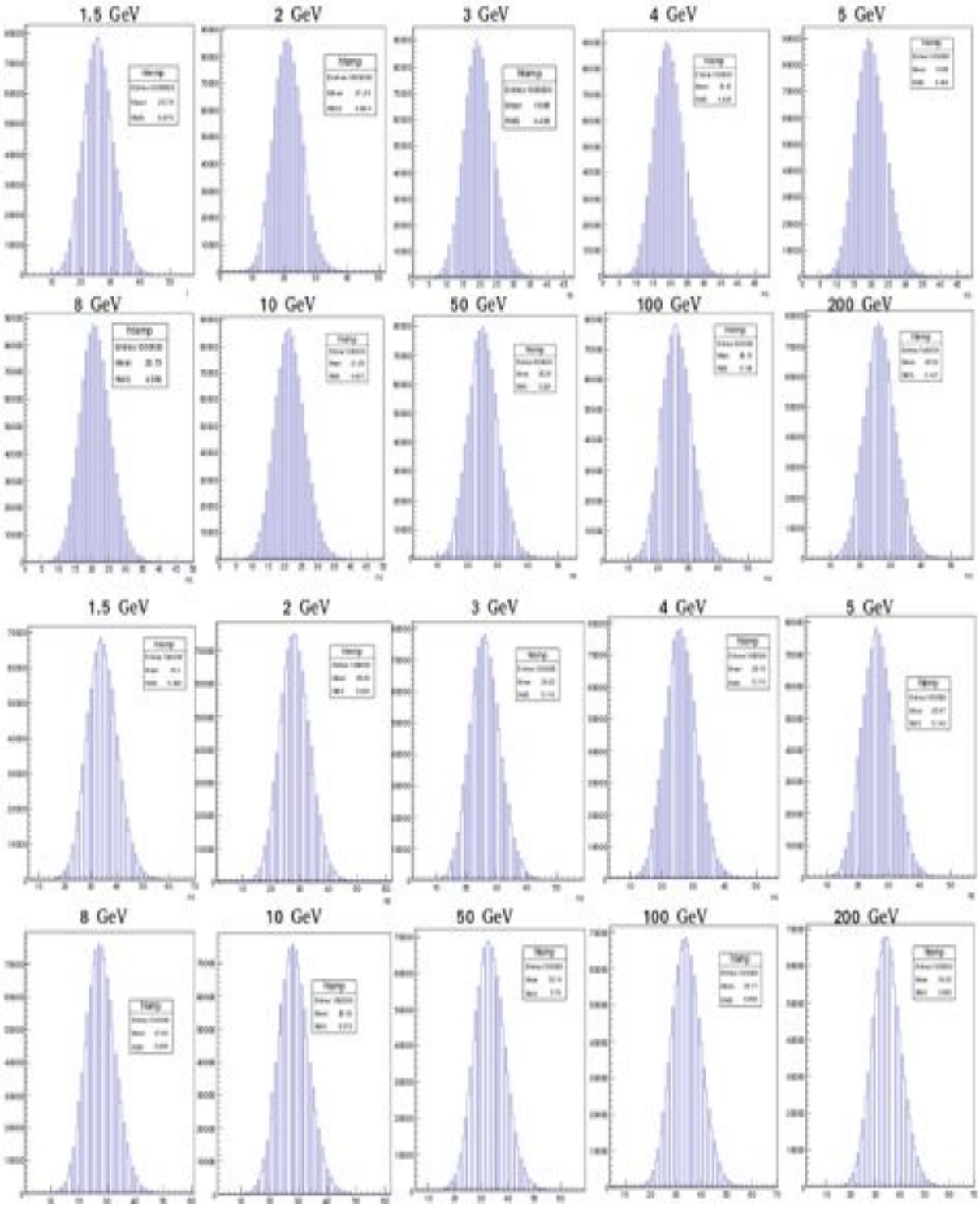

Figure 8.9: primary cluster distribution for protons along a 7 mm track for different energies, produced inside two different gas mixtures ; top eight $ArCO_2$ 70:30 , lower eight $ArCO_2CF_4$ 45:15:40

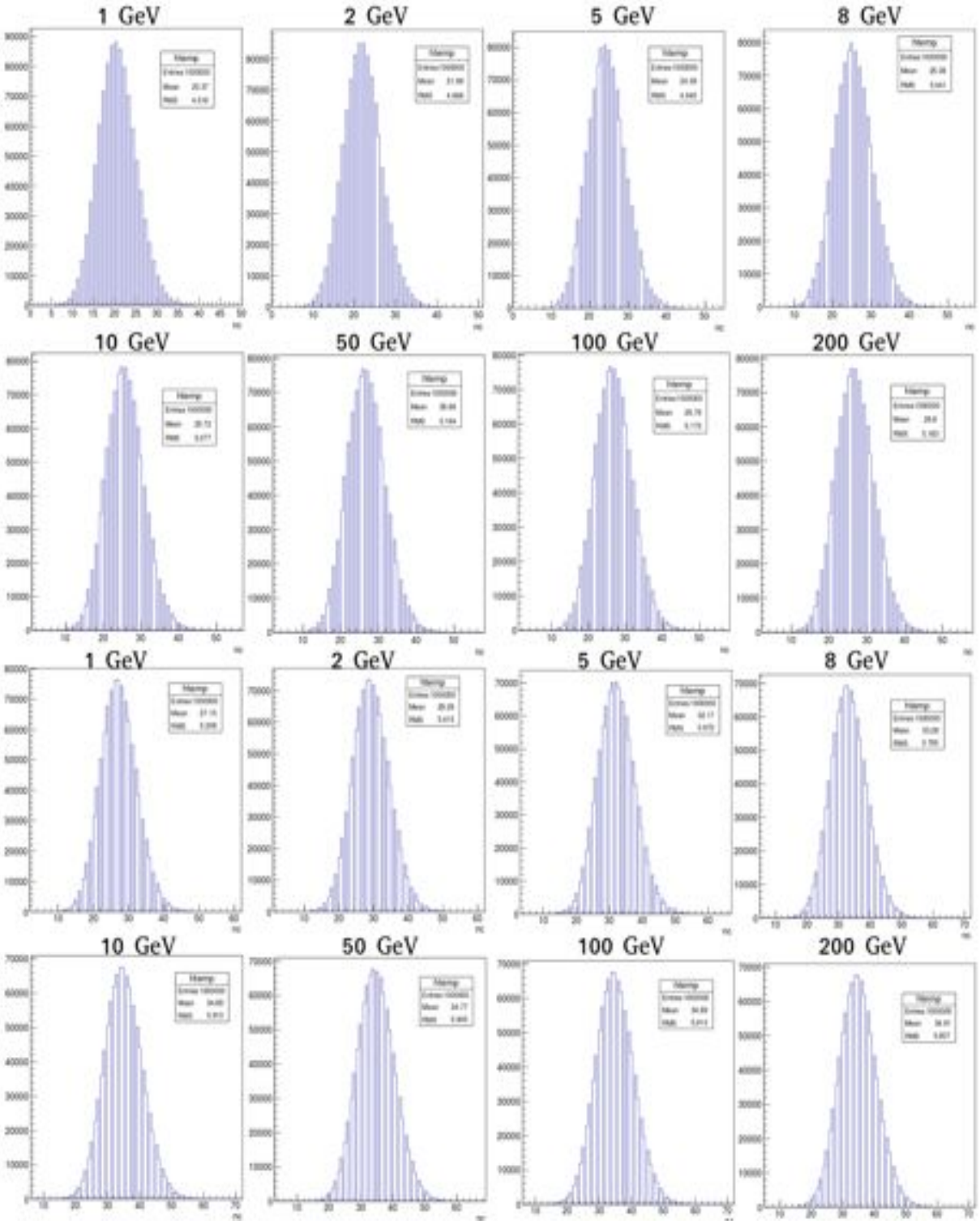

Figure 8.10: primary cluster distribution for charged pions along a 7 mm track for different energies, produced inside two different gas mixtures ; top eight $ArCO_2$ 70:30 , lower eight $ArCO_2CF_4$ 45:15:40

Appendix B

The following transparency and effective gain tables for two different gas mixtures are obtained using Garfield where the values for T and G_{eff} have been extracted by averaging the single electron response over 1000 simulated events.

$ArCO_2$ 70:30	E (kV/cm)	gap (mm)	E (kV/cm)	gap (mm)	E (kV/cm)	(mm)
Drift	3.0	3	3.5	1	3.5	2
Induction	3.5	1	3.5	2	5.0	1
V_{GEM} (V)	T	G_{eff}	T	G_{eff}	T	G_{eff}
300	0.526	7.629	0.463	7.412	0.483	7.056
325	0.611	12.755	0.551	11.831	0.564	11.904
350	0.706	21.871	0.599	19.127	0.674	21.976
375	0.756	38.163	0.671	33.042	0.702	34.595
400	0.819	64.783	0.730	60.805	0.745	62.276
425	0.845	108.903	0.766	100.400	0.775	107.726
450	0.883	204.990	0.820	196.520	0.830	193.190

$ArCO_2CF_4$ 45:15:40	E (kV/cm)	gap (mm)	E (kV/cm)	gap (mm)	E (kV/cm)	(mm)
Drift	3.0	3	3.5	1	3.5	2
Induction	3.5	1	3.5	2	5.0	1
V_{GEM} (V)	T	G_{eff}	T	G_{eff}	T	G_{eff}
300	0.440	1.865	0.427	1.857	0.457	2.020
325	0.565	2.991	0.512	2.785	0.589	3.343
350	0.665	5.152	0.665	5.152	0.672	5.199
375	0.730	7.718	0.741	7.685	0.716	8.382
400	0.780	12.170	0.754	12.601	0.781	13.304
425	0.791	21.017	0.815	20.756	0.797	22.789
450	0.845	33.985	0.836	33.849	0.805	39.948

The single electron response distribution follows a decreasing exponential distribution where the mean value represents the absolute gain. The error committed on this estimation assuming $N = 1000$ independent events for a decreasing exponential distribution equals $\frac{\sigma^2}{\sqrt{N}}$ where σ^2 is the variance and coincides with the mean for this kind of distribution. Hence the error associated with the above results are of the order of 3.16 %

Appendix C

The following transparency and effective gain tables for two different gas mixtures are obtained using Garfield where the values for T and G_{eff} have been extracted by averaging the single electron response over 1000 simulated events.

The voltages accross the respective GEM foils and with the drift/transfer1/transfer2/inductance gap fields resulting from the high voltage divider are shown below.

hV (kV)	ArCO2CF4	ArCO2
3.6	29	249
3.7	51	310
3.8	65	438
3.9	84	620
4	315	1662
4.1	544	3560
4.2	1025	5983
4.3	1714	11592

hV (kV)	ArCO2CF4	ArCO2
4.4	3224	22990
4.5	5424	36752
4.6	6815	44454
4.7	25348	173821
4.8	28710	174823
4.9	115421	1056747
5	149129	1096481
5.1	182695	1087135

Figure 8.11: Effective gain table for the Triple GEM prototype simulated with Garfield.

Appendix C

The errors for the gain measurements taken with the Triple GEM prototype depend on the calibration error and the read out of the output voltage $V_{5.9keV}$ on the oscilloscope. The deviation has been chosen to be Gaussian.

$$\Delta G = \sqrt{\left(\frac{\delta G}{\delta V} \cdot \Delta V\right)^2 + \left(\frac{\delta G}{\delta \beta} \cdot \Delta \beta\right)^2} \tag{8.5}$$

Bibliography

[1] Donald H. Perkins. *Introduction to High Energy Physics*. Cambridge University Press, 13 Apr 2000.

[2] Andrey Marinov. *Feasibility Study of a GEM Based Muon System for the CMS Detector at the Large Hadron Collider*. PhD Thesis.

[3] CERN. The higgs boson, http://home.web.cern.ch/topics/higgs-boson.

[4] Riccardo Argurio. *Introduction to Supersymmetry PHYS-F-417*. Université Libre de Bruxelles.

[5] Lyndon R Evans and Philip Bryant. *LHC Machine*. In: J. Instrum. 3 (2008).

[6] http://home.web.cern.ch/topics/higgs boson. url: http://te- epc-lpc.web.cern.ch/te- epc- lpc/machines/lhc/general.stm.

[7] CMS Collaboration. Technical proposal for the upgrade of the CMS detector through 2020. Technical Report CERN-LHCC-2011-006. LHCC-P-004, CERN, Geneva, Jun 2011.

[8] A Abrahantes Quintana R Achenbach The ALICE Collaboration, K Aamodt. *et al. "The ALICE experiment at the CERN LHC"*. In: Journal of Instrumentation 3.08 (2008), S08002.

[9] E Abat J Abdallah The ATLAS Collaboration, G Aad. *The ATLAS Experiment at the CERN Large Hadron Collider*. In: Journal of Instrumentation 3.08 (2008), S08002.

[10] The CMS Collaboration. *"The CMS experiment at the CERN LHC. The Compact Muon Solenoid experiment"*. In: J. Instrum. 3 (2008). Also published by CERN Geneva in 2010, S08004.

[11] Cms detector. `http://cms.web.cern.ch/news/cms-detector-design`, 2011.

[12] Particle data group. kinematics. `http://pdg.lbl.gov/2011/reviews/rpp2011-rev-kinematics.pdf`, 2011.

[13] Thomas LENZI. Master Thesis : Development and Study of Different Muon Track Reconstruction Algorithms for the Level-1 Trigger for the CMS Muon Upgrade with GEM Detectors. Technical report, Université Libre de Bruxelles.

[14] Observation of a new particle with a mass of 125 gev. http://cds.cern.ch/record/938513, 2006.

[15] Hb+ prepares for insertion into the cms solenoid. http://cms.web.cern.ch/news/observation-new-particle-mass-125-gev, 2012.

[16] Marta Felcini. The Trigger System of the CMS Experiment. Technical report, Tech. rep. arXiv:0806.2540. CMS CR-2008-030. 2008.

[17] E.Rutherford. An electrical method of counting the number of alpha-particles from radio-active substances. Technical report, Proceedings of the Royal Society of London. Series A, Containing Papers of a Mathematical and Physical Character, 81(546) 141–161, 1908. 13.

[18] H. Geiger and W. Müller. Elektronenzählrohr zur messung schwächster aktivitäten. Technical report, Naturwissenschaften, 16(31) :617–618, 1928. 13.

[19] T. Bressani J. Favier G. Charpak, R. Bouclier and Č. Zupančič. The use of multiwire proportional counters to select and localize charged particles. Technical report, Nuclear Instruments and Methods, 62(3) :262 – 268, 1968.

[20] Particle Data Group. Passage of particles through matter, 2011. Technical report.

[21] Enrico Fermi. The ionization loss of energy in gases and in condensed materials. Technical report, Phys. Rev., 57 :485–493, Mar 1940.

[22] Enrico Fermi. The ionization loss of energy in gases and in condensed materials. *Phys. Rev.*, 57:485–493, Mar 1940.

[23] J. Beringer and al. Review of particle physics. *Phys. Rev. D*, 86:010001, Jul 2012.

[24] F.M. Penning and C.C.J. Addink. The starting potential of the glow discharge in neon-argon mixtures between large parallel plates: I. results. *Physica*, 1(7–12):1007 – 1027, 1934.

[25] Geoffrey Mullier. Etude de détecteurs "Triple-GEMs" pour la mise à niveau du spectromètre à muons de l'expérience CMS pour les phases de haute luminosité du LHC. Technical report, MA thesis. Université Libre de Bruxelles, 2011.

[26] G.J. Verhaart, W.J. Van Der Hart, and H.H. Brongersma. Low energy electron impact on chlorofluoromethanes and cf4: Resonances, dissociative attachment and excitation. *Chemical Physics*, 34(2):161 – 167, 1978.

[27] M. Knapp, O. Echt, D. Kreisle, T.D. Märk, and E. Recknagel. Formation of long lived co2, n2o, and their dimer anions, by electron attachment to van der waals clusters. *Chemical Physics Letters*, 126(3–4):225 – 231, 1986.

[28] Tania Moulik Ankit D. Mohapatra. Role of cf4 in gas amplification in gems, novembre 2011.

[29] F. Sauli. Principle of operation of multiwire proportionnal and drift chambers. *Lectures given in the Academic Training Programme of CERN, Geneva*, May 1975-1976.

[30] Maximilien Alexandre Chefdeville. Development of micromegas-like gaseous detectors using a pixel readout chip as collecting anode. *PhD thesis, Universiteit van Amsterdam*, 2009.

[31] A. Einstein. Investigations on the theory of the brownian movement. *Dover Pubns*, 1956.

[32] P. Vanlear G. De Lentdecker C. Vander Velde. Phys-f-420, méthodes expérimentales de la physique des particules. *Université Libre de Bruxelles*, 2011.

[33] Werner Riegler Walter Blum and Luigi Rolandi. Particle detection with drift chambers (particle acceleration and detection). *Springer*, 2008.

[34] Werner Riegler. Signals formation in detectors. *Aida Tutorial, April 9th 2013, Frascati.*

[35] Simon Ramo. Currents induced by electron motion. *Proceedings of the IRE*, 27(9):584–585, Sept 1939.

[36] Fabrice Guilloux. Gdsp asic front end design, 19 avril 2012. `indico.cern.ch/getFile.py/access?contribId=1&sessionId=7&resId=0&materialId=slides&confId=182546`, 2012.

[37] G L Bayatian, S Chatrchyan, G Hmayakyan, and et al Sirunyan. CMS Physics: Technical Design Report Volume 2: Physics Performance. *J. Phys. G*, 34(CERN-LHCC-2006-021. CMS-TDR-8-2):995–1579. 669 p, 2007. revised version submitted on 2006-09-22 17:44:47.

[38] Serguei Chatrchyan and Khachatryan et. al. The performance of the CMS muon detector in proton-proton collisions at $\sqrt{s} = 7$ TeV at the LHC. *J. Instrum.*, 8(arXiv:1306.6905. CMS-MUO-11-001. CERN-PH-EP-2013-072):P11002, Jun 2013. Comments: Submitted to JINST.

[39] F. Sauli. Gem: A new concept for electron amplification in gas detectors. *Nuclear Instruments and Methods in Physics Research Section A: Accelerators, Spectrometers, Detectors and Associated Equipment*, 386(2–3):531 – 534, 1997.

[40] C. Altunbas, M. Capéans, K. Dehmelt, J. Ehlers, J. Friedrich, I. Konorov, A. Gandi, S. Kappler, B. Ketzer, R. De Oliveira, S. Paul, A. Placci, L. Ropelewski, F. Sauli, F. Simon, and M. van Stenis. Construction, test and commissioning of the triple-gem tracking detector for compass. *Nuclear Instruments and Methods in Physics Research Section A: Accelerators, Spectrometers, Detectors and Associated Equipment*, 490(1–2):177 – 203, 2002.

[41] S. Bachmann, A. Bressan, L. Ropelewski, F. Sauli, A. Sharma, and D. Mörmann. Charge amplification and transfer processes in the gas electron multiplier. *Nuclear*

Instruments and Methods in Physics Research Section A: Accelerators, Spectrometers, Detectors and Associated Equipment, 438(2–3):376 – 408, 1999.

[42] M. Capeáns M. Deutel S. Kappler B. Ketzer A. Polouektov L. Ropelewski F. Sauli E. Schulte et al S. Bachmann, A. Bressan. Discharge studies and prevention in the gas electron multiplier (gem). *Nuclear Instruments and Methods in Physics Research Section A : Accelerators, Spectrometers, Detectors and Associated Equipment*, 438(2–3):376 – 408, 1999.

[43] M. Tytgat et al. Status of the triple-gem project for the upgrade of the cms muon system. *Ghent University, Dept. of Physics and Astronomy, Proeftuinstraat 86, 9000 Gent, Belgium.*

[44] Ansys Software. Maxwell. `http://ansys.com/Products/Simulation+Technology/Electromagnetics/Electromechanical+Design/ANSYS+Maxwell.`, 2012.

[45] Parviz Moin. Fundamentals of engineering numerical analysis. Technical report, 2010.

[46] G. Cerminara. Introduction to finite element methods. `http://www.colorado.edu/engineering/cas/courses.d/IFEM.d/`, 2011.

[47] Rob Veenhof. Garfield++. `http://garfieldpp.web.cern.ch/garfieldpp/`, 2010-2012.

[48] Rob Veenhof. Garfield-9. `http://garfield.web.cern.ch/garfield/`, 1984-2010.

[49] H R Skullerud. The stochastic computer simulation of ion motion in a gas subjected to a constant electric field. journal of physics d : Applied physics, 1(11) :1567, 1968. `http://stacks.iop.org/0022-3727/1/i=11/a=423`, 1995-2012.

[50] MAGBOLTZ. Liste de sections efficaces, date dépendante des sections efficaces. `http://rjd.web.cern.ch/rjd/cgi-bin/cross`.

[51] Stephen Biagi. Magboltz. `http://consult.cern.ch/writeup/magboltz/`.

[52] Igor Smirnov. Garfield-9. `http://consult.cern.ch/writeup/heed/`, 1995-2012.

[53] Gas Detector Development Group. read-out of gem detectors. `http://gdd.web.cern.ch/GDD/gemreadout.htm`.

[54] P. Cwetanski M. Ziegler and U. Straumann. A triple gem detector for lhcb. lhcb trac. `http://cdsweb.cern.ch/record/684467`.

[55] CERN Gas Detectors Development Group. Gas electron multiplier - general. `http://gdd.web.cern.ch/GDD/gemgeneral.html`.

[56] A. Sharma. Properties of some gas mixtures used in tracking detectors. *Journal-ICFA 16*, 1998.